

SURFO Technical Reports

Graduate School of Oceanography

2019

SURFO Technical Report No. 19-02

SURFO

Follow this and additional works at: https://digitalcommons.uri.edu/surfo_tech_reports

Recommended Citation

SURFO, "SURFO Technical Report No. 19-02" (2019). *SURFO Technical Reports*. Paper 16.
https://digitalcommons.uri.edu/surfo_tech_reports/16

This Periodical is brought to you for free and open access by the Graduate School of Oceanography at DigitalCommons@URI. It has been accepted for inclusion in SURFO Technical Reports by an authorized administrator of DigitalCommons@URI. For more information, please contact digitalcommons@etal.uri.edu.

Papers from the
**SUMMER UNDERGRADUATE RESEARCH FELLOWSHIP PROGRAM IN
OCEANOGRAPHY**

at

**THE UNIVERSITY OF RHODE ISLAND
GRADUATE SCHOOL OF OCEANOGRAPHY**

Narragansett, Rhode Island

June – August 2019



This program was supported by The National Science Foundation
REU Program (OCE-1757572)



GSO Technical Report No. 19-02

TABLE OF CONTENTS

Table of Contents	iii
Participants in the 2019 Fellowship Program	v
Site Directors' Preface	vi
Wintertime Surface Heat and Momentum Fluxes in the Gulf Stream from Saildrone Observations <i>Marc B. Diard, Stuart P. Bishop, and Kathleen A. Donohue</i>	1
Putting Eyes in the Ocean Twilight Zone: Documenting the World's Largest Animal Migration <i>Agnella R. Dougal, Jackson Sugar, and Melissa M. Omand</i>	7
On the Characteristics of Hurricane Roll Vortices Over Land <i>Paul A. Ernst, Mansur A. Jisan, and Isaac Ginis</i>	16
Development of the Internal Structure and Mechanism of the Multipurpose Autonomous Underwater Vehicle (MAUVE) <i>Nicolai Gershfeld and Mingxi Zhou</i>	28
Comparing Phytoplankton Carbon to Volume Relationships Using Three-Dimensional (3D) and Two-Dimensional (2D) Imaging <i>Courtney N. Hammond, Heather McNair, and Susanne Menden-Deuer</i>	31
Mapping of Tectonic Features Submerged Beneath Lake Azuei, Haiti: Implications for Seismic Hazards <i>Kamal R. James, Marie-Hélène Cormier, and Heather Sloan</i>	42
Using Stable Isotopes to Trace Marine Ecogeochemical Cycling in Chemosynthetic Symbiotic <i>Solemya velum</i> <i>Sommer Meyer, Nina Santos, Roxanne Beinart, and Kelton McMahon</i>	57
Examining How Primary Productivity Shifts Over A Summer Season in Narragansett Bay <i>Lydia Nunez, Diana Fontaine, Samantha Setta, and Tatiana Ryneerson</i>	68
Testing Nanographene as a Passive Sampler for Emerging Contaminants of Environmental Concern in Narragansett Bay <i>Jamillez Olmo Classen, Jitka Becanova, Simon Votja, and Rainer Lohmann</i>	75
Understanding Sediment Biogeochemical Exchanges of Nutrients Impact on Ecosystem Health in Narragansett Bay <i>Forrest G. Pilone and Rebecca Robinson</i>	78

The Effect of Rising and Falling Tides and Current on Matunuck Oyster Farm <i>Sandra Rech and Chris Roman</i>	88
Understanding the Key Contributors to Smooth Dogfish Trends in Abundance in New Jersey and Delaware Waters <i>Brianna Villalon and Camilla McCandless</i>	91
Using Multi-GNSS Interferometric Reflectometry to Monitor Sea Level in Newport, Rhode Island <i>Benjamin A. Watzak and Meng Wei</i>	94

2019 PROGRAM PARTICIPANTS
SUMMER UNDERGRADUATE RESEARCH FELLOWSHIP IN OCEANOGRAPHY

FELLOWS

Marc Diard
Agnella Dougal
Paul Ernst
Nick Gershfeld
C. Nicole Hammond
Kamal James
Sommer Meyer
Lydia Nunez
Jamillez Olmo Classen
Forrest Gage Pilone
Sandra Rech
Brianna Villalon
Benjamin Watzak

ADVISORS

Jitka Becanova
Roxanne Beinart
Stuart Bishop (North Carolina State University)
Marie-Hélène Cormier
Kathleen Donohue
Isaac Ginis
Rainer Lohmann
Camilla McCandless (NOAA)
Kelton McMahon
Heather McNair
Susanne Menden-Deuer
Melissa Omand
Rebecca Robinson
Christopher Roman
Tatiana Rynearson
Matt Wei
Mingxi Zhou

MENTORS AND COLLABORATORS

David Casagrande
Diana Fontaine
Kun Gao
Dennis Graham
Michelle Hauer
Mansur A. Jisan
Pat Kelly
Chris Kerr
Kristine Larson (University of Colorado)
Chris Mayer
Sarah Nickford
Catherine Nowakowski
Jaime Palter
Nina Santos
Angela Stahl
Jackson Sugar
Samantha Setta
Heather Sloan (Lehman College)
Jackson Sugar
Simon Votja

PROGRAM ASSISTANTS

Asta Habtemichael, URI Student Liaison
Caryl Jardon, Program Administrator

PREFACE

This report presents the papers written by the 13 participants in the ten weeks of the 2019 Summer Undergraduate Research Fellowships in Oceanography (SURFO) program at the Graduate School of Oceanography (GSO), University of Rhode Island (URI). The papers are introduced in alphabetical order of the participants. Nine papers follow manuscript-style presentation, whereas four are written to satisfy the proposal requirements for application to the National Science Foundation Graduate Research Fellowship Program. This 2019 summer represented the 35th consecutive year in which the program has been coordinated and extended through the several disciplines in oceanography and ocean engineering at URI's Narragansett Bay Campus. The activities continue excellence beyond the official duration of the program with six planned presentations at national conferences: one presentation for the AGU 2019 Fall Meeting in San Francisco (CA), one for the Joint Mathematics Meetings (JMM 2020) in Denver (CO), and four projects as posters for the 2020 Ocean Sciences Meeting in San Diego (CA).

The 2019 SURFO participants are grateful to the National Science Foundation REU program for their support through grant OCE-1757572. The SURFO program sincerely thanks advisors and mentors who contributed to the program's success including those who gave SURFO seminar presentations and/or participated in various educational activities. In addition, our thanks go to Caryl Jardon for her timely assistance covering administrative and financial tasks. Finally, we acknowledge Asta Habtemichael who served as the program student liaison.

Lucie Maranda
David C. Smith
SURFO Site Directors

October 2019

Wintertime Surface Heat and Momentum Fluxes in the Gulf Stream from Saildrone Observations

Marc B. Diard^{1,2}, Stuart P. Bishop², and Kathleen A. Donohue¹

¹Graduate School of Oceanography, University of Rhode Island, Narragansett, RI, USA.

²Department of Marine, Earth, & Atmospheric Sciences, North Carolina State University, Raleigh, NC, USA.

Corresponding author: Marc Diard (mbdiard@ncsu.edu)

Running head: Winter Gulf Stream Heat Flux from Saildrone

Key Points:

- Majority of annual air-sea heat flux from Gulf Stream occurs in winter storms
- ERA5 reanalysis model compares well to Saildrone-observed data

Key Index Words: Saildrone, ERA5, Heat Flux, Gulf Stream, Air-sea Interactions, Western Boundary Currents

Abstract

Every winter, the ocean loses a tremendous amount of heat from the passage of weather systems that transport cold and dry continental air from the US across the warm and moist Gulf Stream. To measure this air-sea interaction, a new autonomous observing platform - the Saildrone - was deployed in the Gulf Stream from late January through early March 2019. The Saildrone offers a unique opportunity to observe the heat and momentum fluxes at the ocean's surface during winter when it is challenging to observe. Accomplishing five crossings of the Gulf Stream, the Saildrone measured surface ocean and atmospheric parameters such as surface air and sea temperature, barometric pressure, wind, and relative humidity. In addition to these variables, the Saildrone was equipped with an acoustic Doppler current profiler enabling surface current measurements. Heat and momentum fluxes were computed using these state variables in the Coupled Ocean-Atmosphere Response Experiment (COARE) version 3 algorithm. These fluxes were used to study how the ocean loses heat during the passage of major wintertime weather systems. The goals of this study were to first compare the surface fluxes with climatology and predicted fluxes from the reanalysis data set ERA5. The comparison is favorable, with correlation coefficients between the datasets ranging from 0.90 to 0.99. Large heat fluxes (~1200 W/m²) occur during the passage of the winter weather systems.

1. Introduction

1.1 Ocean Heat Flux

The ocean plays an important role in the global energy balance. Heat is absorbed by the ocean in the lower latitudes, very close to the equator. From there it is transported poleward as part of the sub-tropical gyre circulation, in the ocean's western boundary currents. As these currents move poleward in their respective ocean basins, they eventually release the heat to the atmosphere. This interaction has been known for some time. Most of this heat flux occurs during storms in the wintertime months (Shaman et. al, 2010), yet measuring these fluxes with traditional ship-based or moored techniques is difficult during winter owing to the intense storm

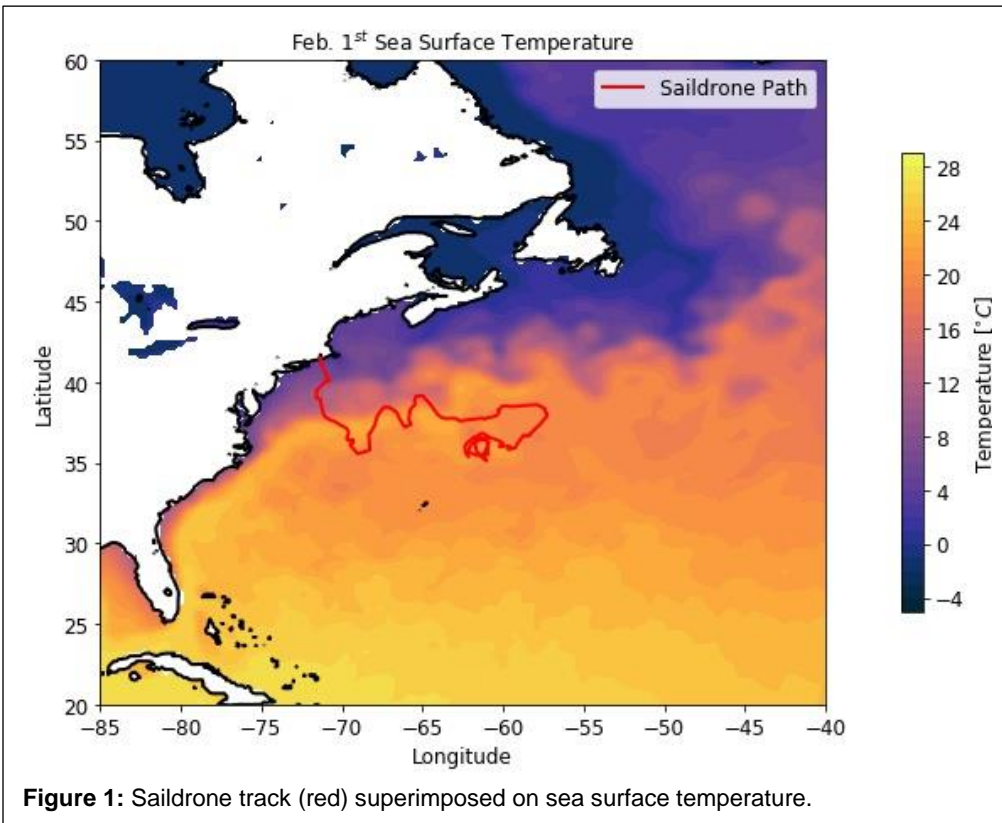
systems. An innovative autonomous platform termed Saildrone managed by Saildrone Inc. seeks to successfully measure surface and ocean properties in order to quantify air-sea fluxes. Moreover, Saildrone Inc. seeks a robust platform capable of working in harsh conditions that are inaccessible with current technologies.

The goal of this study is to examine a three-month winter Saildrone mission within the Gulf Stream. Motivation derives from the comparably low number of surface measurements on this area of the ocean during winter. A natural question is: ‘How well do atmosphere-ocean reanalysis products simulate air-sea properties near the Gulf Stream during winter?’ Here, a comparison is conducted between a wintertime Saildrone mission and a new reanalysis product, the ERA5 (C3S, 2019).

2. Materials and Methods

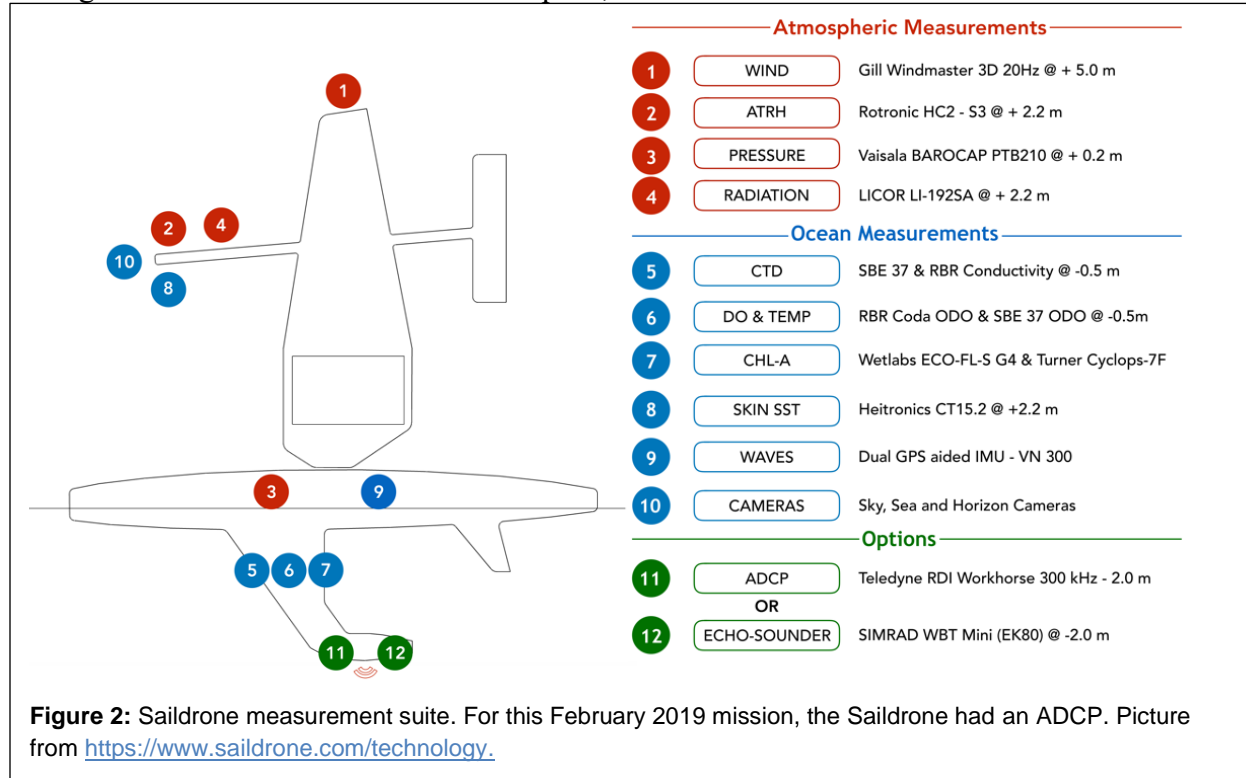
2.1 Saildrone Measurements

The Saildrone collected data during the month of February 2019. Figure 1 shows its track. It set sail from Rhode Island on January 30th and headed south to the Gulf Stream. There it made five Gulf Stream crossings, before turning south to make a scheduled rendezvous with the R/V *Endeavor* in the Sargasso Sea. Unfortunately, an intense extratropical storm system rapidly strengthened as the Saildrone headed to meet the R/V *Endeavor*. The 10-m waves generated by the storm damaged the Saildrone sail and partially disabled the instrumentation. The Saildrone collected data from Jan. 30 to March 2, 2019.



On this mission, the Saildrone had a suite of measuring tools and devices, consisting of the basic loadout (Zhang et. al, 2019), as seen in Figure 2. Here we focus on the following variables:

air temperature, sea surface temperature (SST), wind speed and direction, surface currents, sea level pressure, and relative humidity. Data were recorded every minute. Here we use hourly-averaged data. Based on the Saildrone's speed, that is a resolution of about 4.5 km.



2.2 Air-Sea Flux Calculations

The air-sea fluxes calculated from Saildrone data use the COARE v3 algorithm (Fairall et. al, 2003). Our focus is heat and momentum fluxes. The COARE algorithm uses surface currents to correct wind speed in order to calculate the turbulent fluxes.

3. Reanalysis Product

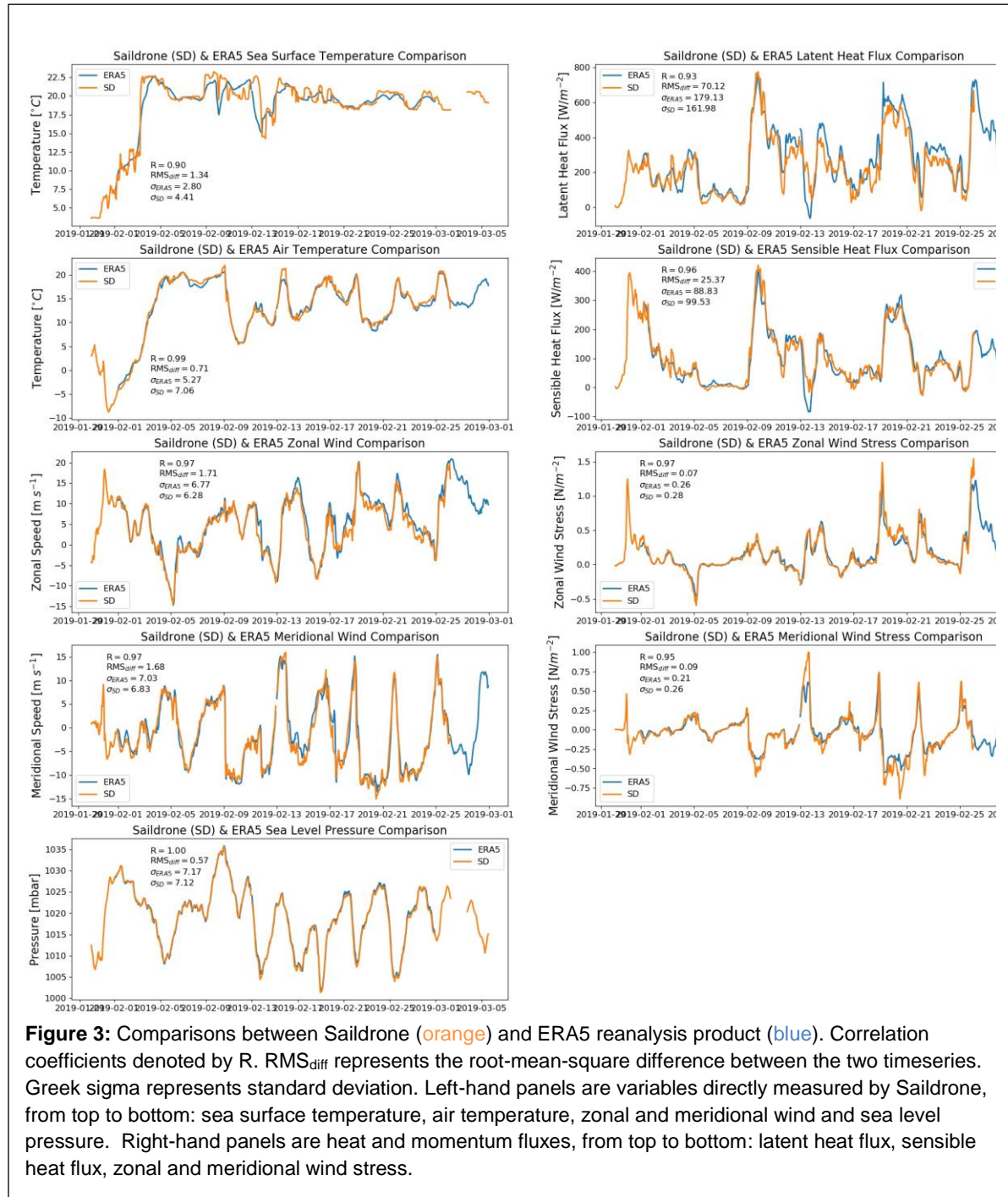
The reanalysis product is the ERA5 Reanalysis Product (C3S, 2019). This dataset is compared with Saildrone data for the month of February 2019 in order to determine the validity of the ERA5 product during wintertime in the Gulf Stream. The ERA5 variables that were used are SST, air temperature at 10 m, sea level pressure, zonal and meridional wind, latent and sensible heat flux, as well as zonal and meridional wind stress. The ERA5 product has a grid resolution of 0.25° , and a temporal resolution of one hour. To compare with the Saildrone data, ERA5 was linearly interpolated along the hourly-averaged Saildrone track.

4. Results and Discussion

4.1 Saildrone-ERA5 Comparisons

The comparisons of the Saildrone data with the ERA5 product show that the series are highly correlated (Figure 3). Correlation coefficients for all of the comparisons are greater than 0.9. Notable results are the high correlation coefficient for sea level pressure, as well as a comparatively low correlation coefficient of 0.9 for SST. However, when looking at a comparison of root-mean-square (rms) differences, the SST, latent heat flux, and sensible heat

flux all have fairly high rms difference/standard deviation ratios. For SST, this is most likely caused by the relatively low resolution of ERA5 – 0.25° – compared to the ~ 4.5 km Saildrone resolution. Note the Saildrone and ERA-5 SST time series near the edges of the Gulf Stream. The Gulf Stream crossings are identified by the rapid changes in SST. Additionally, the variance of the ERA SST is reduced compared to Saildrone by 40%. Again, this reflects the relatively coarse resolution of ERA5.



Air-sea fluxes compare well (right panels of Figure 3). The latent and sensible heat fluxes show the impact of storm systems. Both series exhibit a series of pulses of elevated air-sea fluxes associated with the passage of extratropical storm systems. Nevertheless, upon close examination, fairly large deviations are present (right panels of Figure 3). The amplitude of the strong events is larger in Saildrone compared to ERA5 and this is especially so for events after Feb 13. These differences seem focused on specific events, implying that the ERA5 product has difficulty capturing the magnitudes of the fluxes during the passage of winter storms.

4.2 Storm Case Study

A more in-depth look into one of these events (Feb. 9th – 11th) allows an examination of the fluxes and state variables during this high flux period. A clear low-pressure system can be seen moving west to east offshore of Canada (Figure 4). The winds circling this system push cold, dry continental air off the mainland, leading to the large air-sea temperature differences. This temperature difference feeds directly into the high fluxes that occur over the Gulf Stream. The peak heat flux during this event was 1196 W/m². The annual average flux within the Gulf Stream in this region is about 200 W/m² (Shaman et. al, 2010). Thus, the majority of the annual heat flux not only occurs during winter months but occurs in an event-like manner associated with a handful of extratropical storm systems each year.

5. Conclusions

The Saildrone observational platform gathered data during February 2019, crossing the Gulf Stream five times. These data were compared with the ERA5 reanalysis product, with very good agreement, showing that the ERA5 product is reliable for use in wintertime Gulf Stream region. The majority of net heat flux occurring in the Gulf Stream occurs in a few singular wintertime events; mainly storms. This particular Saildrone mission lacked shortwave and longwave radiation measurements. As a result, the net air-sea flux could not be calculated. Future missions would benefit from the inclusion of these sensors.

Acknowledgments

Marc Diard was supported by a Summer Undergraduate Research Fellowship in Oceanography (SURFO) (National Science Foundation REU Grant # OCE- 1757572). He would also like to thank Dr. Jaime Palter, for sharing access to the Saildrone data, as well as Sarah Nickford, for her assistance with data processing.

References

- Copernicus Climate Change Service (C3S) (2017): ERA5: Fifth generation of ECMWF atmospheric reanalyses of the global climate. Copernicus Climate Change Service Climate Data Store (CDS), July 8, 2019. <https://cds.climate.copernicus.eu/cdsapp#!/home>
- Fairall, C.W., E.F. Bradley, J.E. Hare, A.A. Grachev, and J.B. Edson, 2003: Bulk Parameterization of Air–Sea Fluxes: Updates and Verification for the COARE Algorithm. *J. Climate*, **16**, 571–591, [https://doi.org/10.1175/1520-0442\(2003\)016<0571:BPOASF>2.0.CO;2](https://doi.org/10.1175/1520-0442(2003)016<0571:BPOASF>2.0.CO;2)
- Shaman, J., R.M. Samelson, and E. Skillingstad. 2010. Air–Sea Fluxes over the Gulf Stream Region: Atmospheric Controls and Trend. *J. Climate*, **23**, 2651–2670. <https://doi.org/10.1175/2010JCLI3269.1>
- Zhang, D., M. F. Cronin, C. Meinig, J. T. Farrar, R. Jenkins, D. Peacock, Jennifer Keene, A. Sutton, and Q. Yang. June 2019. Comparing Air-Sea Flux Measurements from a New Unmanned Surface Vehicle and Proven Platforms During the SPURS-2 Field Campaign. *Oceanography*, **32**, 122–133.

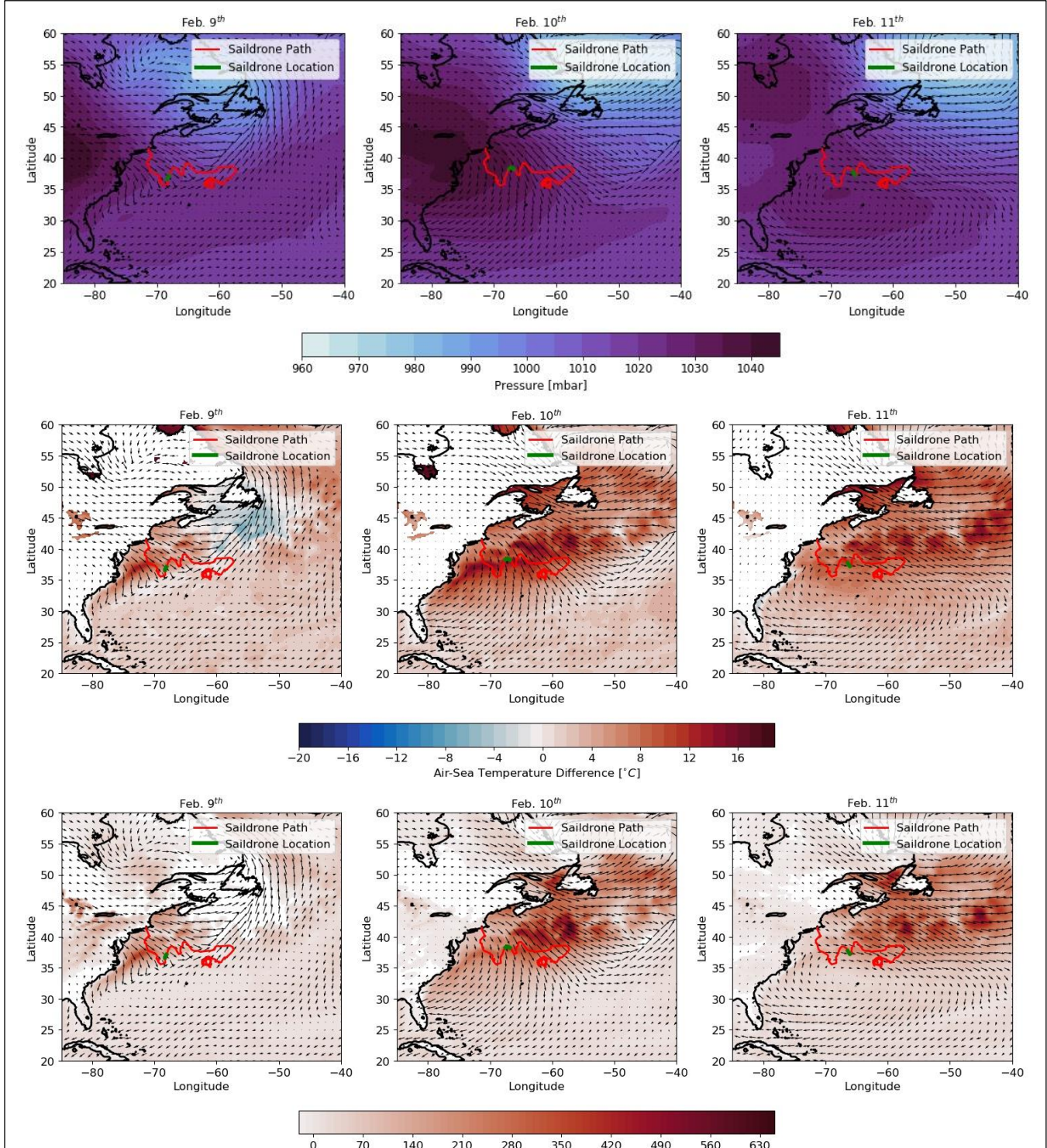


Figure 4: Saildrone mission path (red) and location (green) on Feb 9 (left panels) Feb 10 (center panels) and Feb 11 (right panels) superimposed on ERA5 sea level pressure (top panels) air-sea temperature difference (middle panels) and sensible heat flux (bottom panels). Black vectors denote ERA5 10 m winds.

"Putting eyes in the Ocean Twilight Zone: Documenting the world's largest animal migration"

Agnella R. Dougal ¹, Jackson Sugar ¹, and Melissa M. Omand ^{1,*}

¹*University of Rhode Island, Graduate School of Oceanography, Narragansett, RI,
USA*

Correspondence*:
Melissa M Omand
momand@uri.edu

2 ABSTRACT

3 Many zooplankton swim hundreds of meters every day; finding refuge from predators in deep,
4 dark regions during the day and travel up the water column to the euphotic zone at night to feed.
5 This diel behavior constitutes Earth's largest migration and plays an important role in ecology and
6 carbon export in the ocean. This summer, I learned how to build a low-cost underwater camera
7 to image zooplankton and particles nominally 1mm to 2cm in size. An individual camera unit
8 was completed as well as a separate camera unit for observing real-time images and videos in
9 a test chamber. The data obtained in this experiment will hopefully illuminate the physical and
10 ecological interactions of living and non-living entities in the mesopelagic. Putting 'many eyes in
11 the twilight zone' through low-cost imaging tools and automated processing will bring us closer to
12 the life of these sparse and enigmatic creatures living there.

13 **Keywords:** DIY Oceanography, Camera Chain System, Arduino Nano, Raspberry Pi Electronics, Build Housings, Mesopelagic,
14 Zooplankton, Marine Snow

(The rest of this section intentionally left blank)

On the Characteristics of Hurricane Roll Vortices Over Land

Paul A. Ernst, Mansur A. Jisan, and Isaac Ginis

Graduate School of Oceanography, University of Rhode Island, Narragansett, Rhode Island

Corresponding author: Paul Ernst, ernstp@uri.edu

Running head: Hurricane Roll Vortices Over Land

Key Points:

- Hurricane roll vortices strengthen significantly upon hurricane landfall
- Roll vortices strengthening may contribute to hurricane landfall wind damage

Key Index Words:

Hurricane Boundary Layer, Numerical Model, Roll Vortices, Landfall

Abstract

The hurricane boundary layer (HBL) is the region of heat and momentum fluxes that enables a hurricane to extract energy from the ocean. Horizontal roll vortices (rolls) are a secondary circulatory structure observed within the HBL. Observations first established the existence and extent of rolls generated by the inflection point instability of the HBL flow. Theoretical and numerical studies described the behaviors of rolls under both stationary and moving hurricanes over the open ocean. Previous studies at the GSO hurricane group created a two-dimensional high-resolution single-grid roll-resolving model (SRM) embedded within the horizontal grid points of an HBL model. In this study, we continue the development of the SRM in order to simulate the effect of land surface roughness on rolls. We find that the effect of land surface roughness positively influences factors in the HBL model that contribute to the formation of larger roll wavelengths. Furthermore, SRM-simulated rolls formed in a storm over land contain an order of magnitude more kinetic energy than those formed over the water. We conclude that rolls strengthen significantly upon landfall. This presents a new factor for the prediction of wind damage upon storm landfall that is not taken into account by current impact forecasting models.

1. Introduction

Roll vortices (hereafter rolls) are observed as coherent vortices aligned in the mean wind direction that continually form in the hurricane boundary layer (HBL) (Wurman and Winslow 1998; Morrison et al. 2005; Lorsolo et al. 2008; Zhang et al. 2008; Ellis and Businger 2010). Analytical and model-based studies conclude that rolls are generated via the inflection-point instability in basic-state wind profiles (Foster 2005; Gao and Ginis 2014, hereafter GG14; Gao and Ginis 2016; Nakanishi and Niino 2012; Wang and Jiang 2017). Such studies demonstrated that such rolls influence hurricane intensity and structure through varied entropy and momentum fluxes (Zhang et al. 2008; Gao and Ginis 2016; Gao et al. 2017). GG14 additionally proposes

positive correlations between roll growth rate and radial wind shear magnitude as well as roll wavelength and boundary layer height. Lastly, Gao and Ginis (2018) (hereafter GG18) explores the effects of hurricane wind asymmetry caused by a moving storm, including evidence that a greater boundary layer height correlates with lower roll growth rate.

Every study performed so far on the subject of roll vortices has been concentrated on a storm over the open ocean, with the effect of an elevated surface roughness heretofore unknown. In this study, we examine linear phase rolls under a stationary and moving hurricane over land using a numerical model. As in GG18, linear phase rolls are rolls that are growing exponentially but are at least one order of magnitude smaller than mean winds, making nonlinear terms in governing equations negligible. The purpose of this study is to examine the differences in roll size and intensity between water and land surface roughness in order to better determine the possible impacts of rolls on landfall wind damage.

2. Methods

Our approach mirrors that of GG14 and GG18, utilizing a linear two-dimensional single-grid roll-resolving model (SRM) and a diagnostic HBL model. Linear roll equations are identical to GG14 [their equations (7)-(10)] and are therefore not displayed here. As in GG14 and GG18, the HBL wind fields are assumed to be in a steady state, with secondary flow in the form of radial and vertical winds due to surface friction. The equations for mean wind components in Cartesian coordinates are exhibited in GG18 [their equations (1)-(3)]. We similarly set the asymptotic mixing length to 40 m in accordance with the reasoning in GG18.

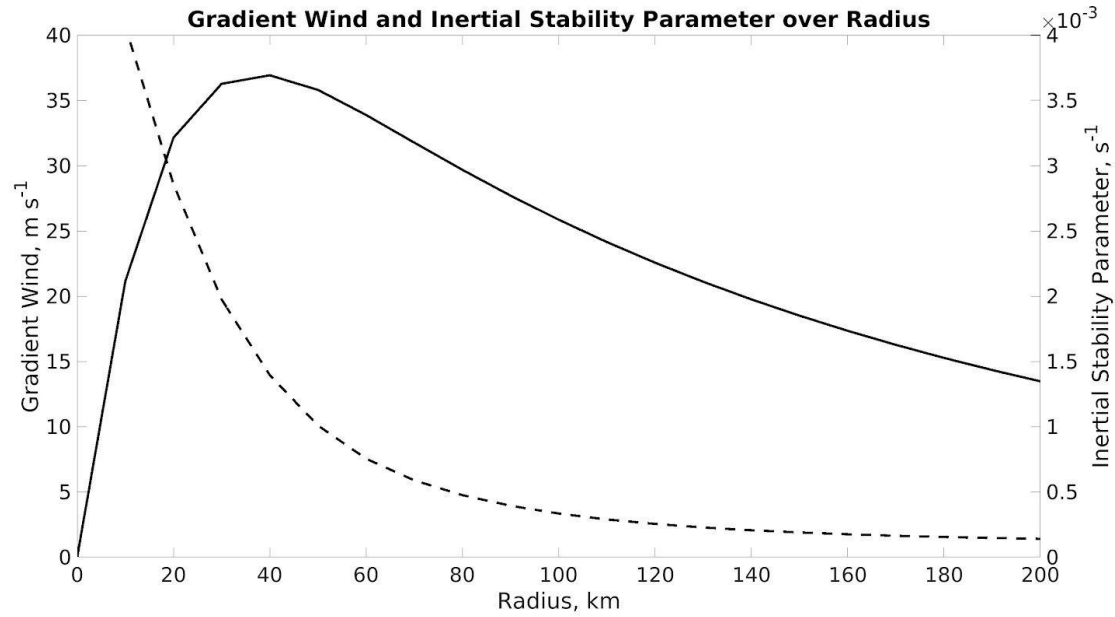


Figure 1: Gradient wind (solid line) and inertial stability parameter (dashed line) as functions of radius. This is a similar distribution to that found in GG14 Figure 2.

In our experiments with a moving storm, we use the same translational coordinate system as implemented in Kepert and Wang (2001) and GG18. The storm moves to the west at a constant

speed of 5 m s^{-1} ($U_g = -5 \text{ m s}^{-1}$) with the mesh and hurricane moving at the same speed, such that the hurricane and mesh do not move relative to each other. The wind at the top of the 3-km boundary height is in the gradient wind balance and its radial distribution is prescribed using the Holland (1980) parametric model (Figure 1). The pressure gradient force is described by a solution to GG14 equation 4 and assumed vertically uniform.

Four experiments are performed in this study. The four experiments represent the four possible configurations of a stationary versus moving storm and a storm over land versus a storm over water. To this end, experiment W_S is a stationary storm over water ($znot = .002$; $U_g = 0 \text{ m s}^{-1}$), experiment W_M is a moving storm over water ($znot = .002$; $U_g = -5 \text{ m s}^{-1}$), experiment L_S is a stationary storm over land ($znot = .05$; $U_g = 0 \text{ m s}^{-1}$), and experiment L_M is a moving storm over land ($znot = .05$; $U_g = -5 \text{ m s}^{-1}$). As in GG14 and GG18, the HBL model domain is a 1000 km square with 10-km horizontal and 30-m vertical grid spacing, and hurricane maximum wind value of 39 m s^{-1} at a radius of 40 km is prescribed at a 3-km height.

The HBL model is run with similar methodology as GG18, reaching a steady state at approximately 20 hours before embedding the linear SRM. We embed the SRM for 4 hours at the locations of the radius of maximum wind (hereafter RMW), equaling 40 (hereafter RMW 1), 80 (RMW 2), and 120 (RMW 3) kilometers, respectively. As in GG18, we assumed a neutrally stratified HBL.

3. Results

3.1. Confirmation of Previous Studies

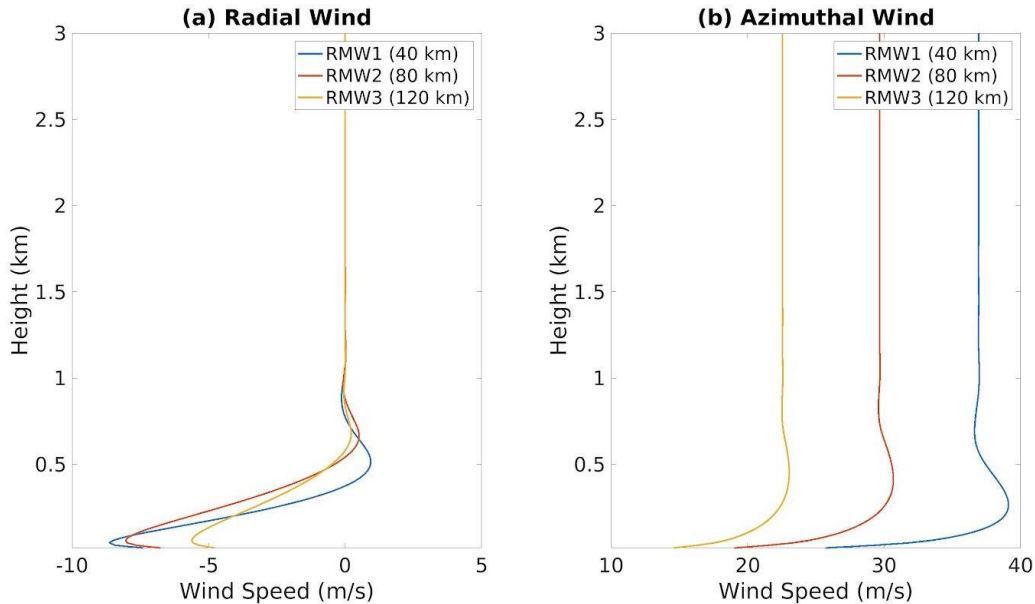


Figure 2: Vertical profiles of (a) radial wind and (b) azimuthal wind at RMW 1, RMW 2, and RMW 3 within experiment W_S. Compare with GG14 Figure 4.

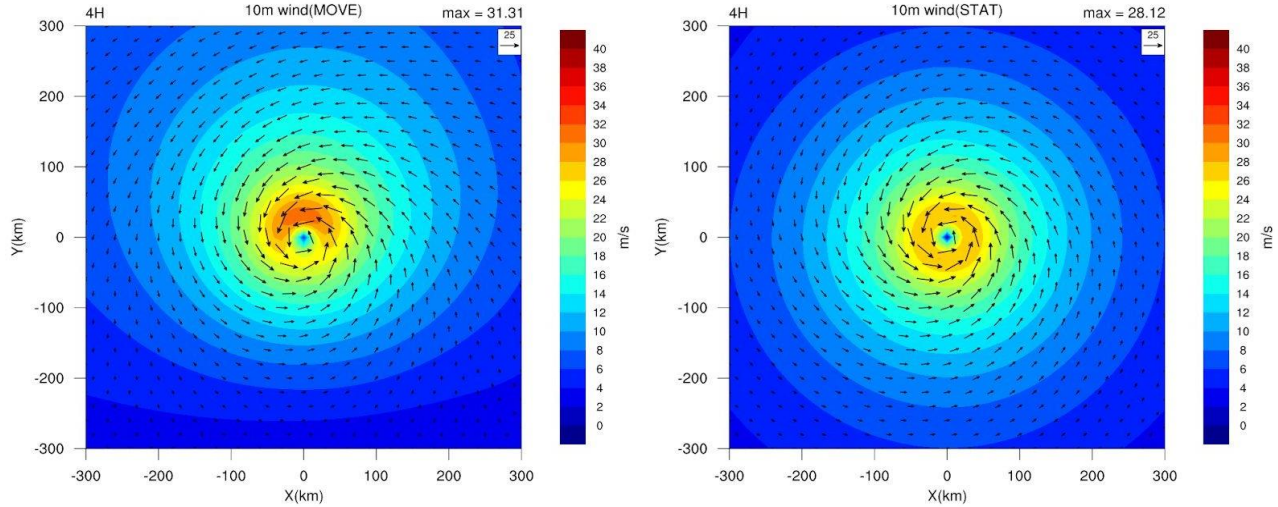


Figure 3: Top-down visualizations of 10-meter-height winds from experiments W_M and W_S at 20 hours into the HBL model simulation. This is a comparable distribution to that found in GG18 Figure 1.

Figure 2 is a recreation of GG14 Figure 4 using data from experiment W_S. The shapes of the profiles and their extrema are consistent with findings from GG14, demonstrating that the basic HBL model is consistent with those used in previous studies. Figure 3 is a similar confirmation using 10-meter-height wind data from experiments W_S and W_M to illustrate the impact of translational movement of the storm. These data are generally consistent with experiments MOVE and STAT in GG18 and align with their results.

3.2. Differences in the Characteristics of the HBL due to Land

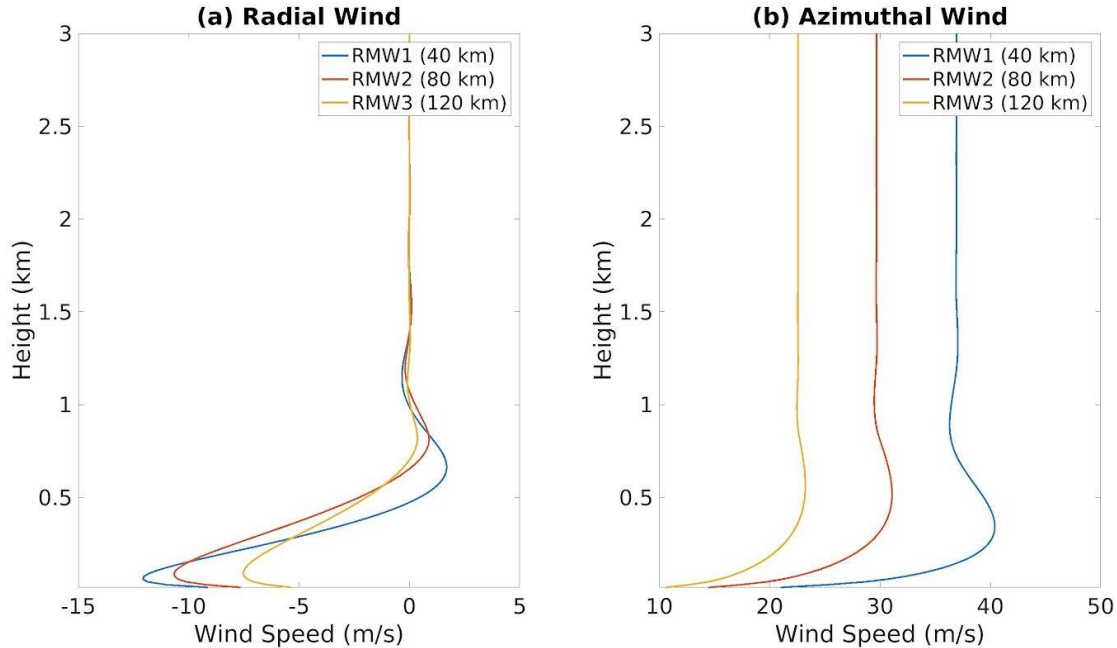


Figure 4: Vertical profiles of (a) radial wind and (b) azimuthal wind at RMW 1, RMW 2, and RMW 3 using the profiles from experiment L_S.

The mean wind profiles of experiment L_S is shown in Figure 4, while the difference between the mean wind profiles of experiments W_S and L_S is displayed in Figure 5. The effect of land surface roughness is evident in two ways. The first is the increased extrema exhibited by the land case-- both the negative peaks from approximately 0 m to 250 m in height as well as the positive peaks from between 500 m and 750 m in height represent the effects of greater friction on the balance of forces influencing the low-altitude mean winds. Secondly, a variation in wind profiles exists up to a height of nearly 2 km, as compared to the 1-km variation heights in Figure 1.

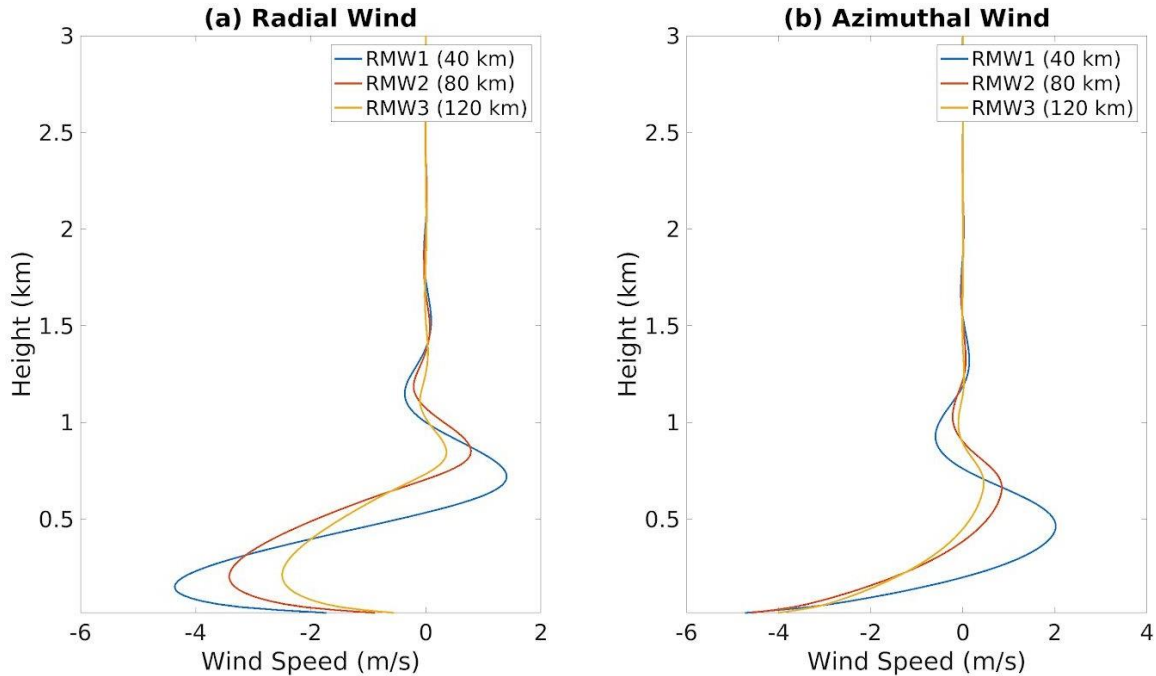


Figure 5: Vertical profiles of (a) radial wind and (b) azimuthal wind at RMW 1, RMW 2, and RMW 3 using the difference between the profiles from experiments W_S and L_S.

Turbulent viscosity, K , is another basic-state HBL variable that varies in a landfalling storm (Figure 6). Three profiles are given using data from W_S, L_S, and the difference between the two experiments. The positive difference between the landfalling and water cases suggests an increase in mixing occurs at landfall throughout the boundary layer.

Figures 7 and 8 display the cross sectional profiles of the radial, azimuthal, and vertical components of the mean wind for experiments W_M and L_M, and the differences between experiments W_M and L_M are presented in Figure 9. As in Figure 5, the increase in land surface roughness produces an increase in radial wind extrema, with an intensification occurring in the lowest layer of the radial wind. The azimuthal wind also changes as expected from Figure 5, with a decrease of wind velocity in the lowest layer followed by an increase in the layer above.

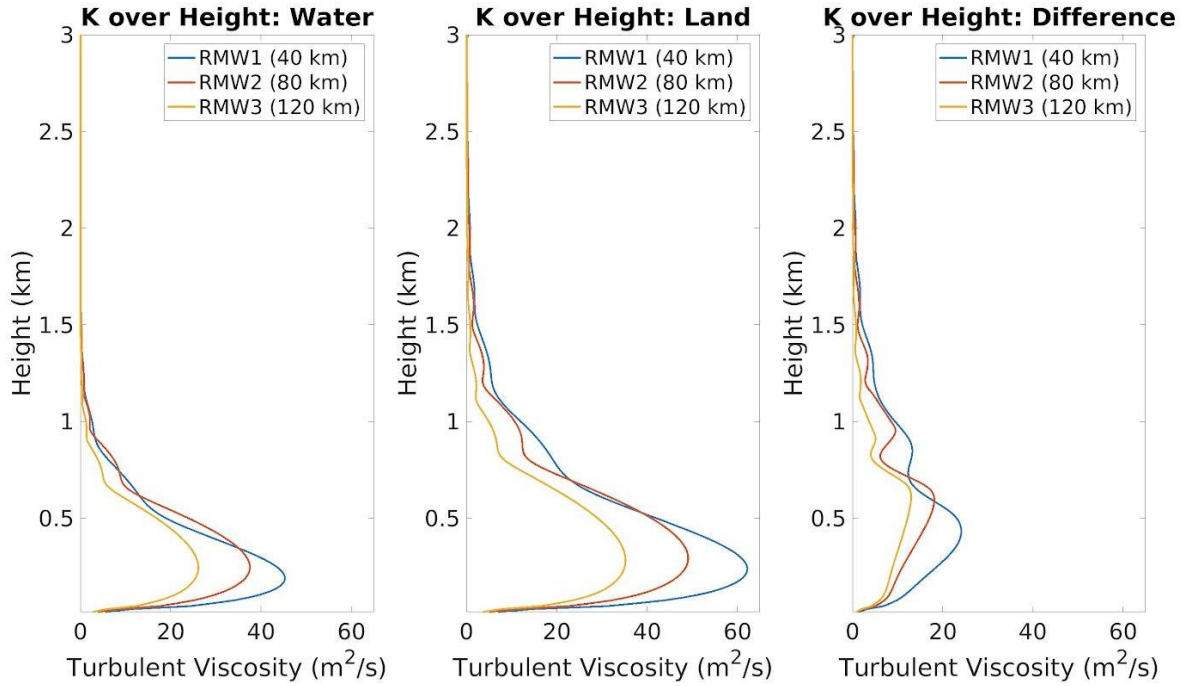


Figure 6: Turbulent viscosity profiles at RMW 1, RMW 2, and RMW 3 for experiments W_S, L_S, and their differences.

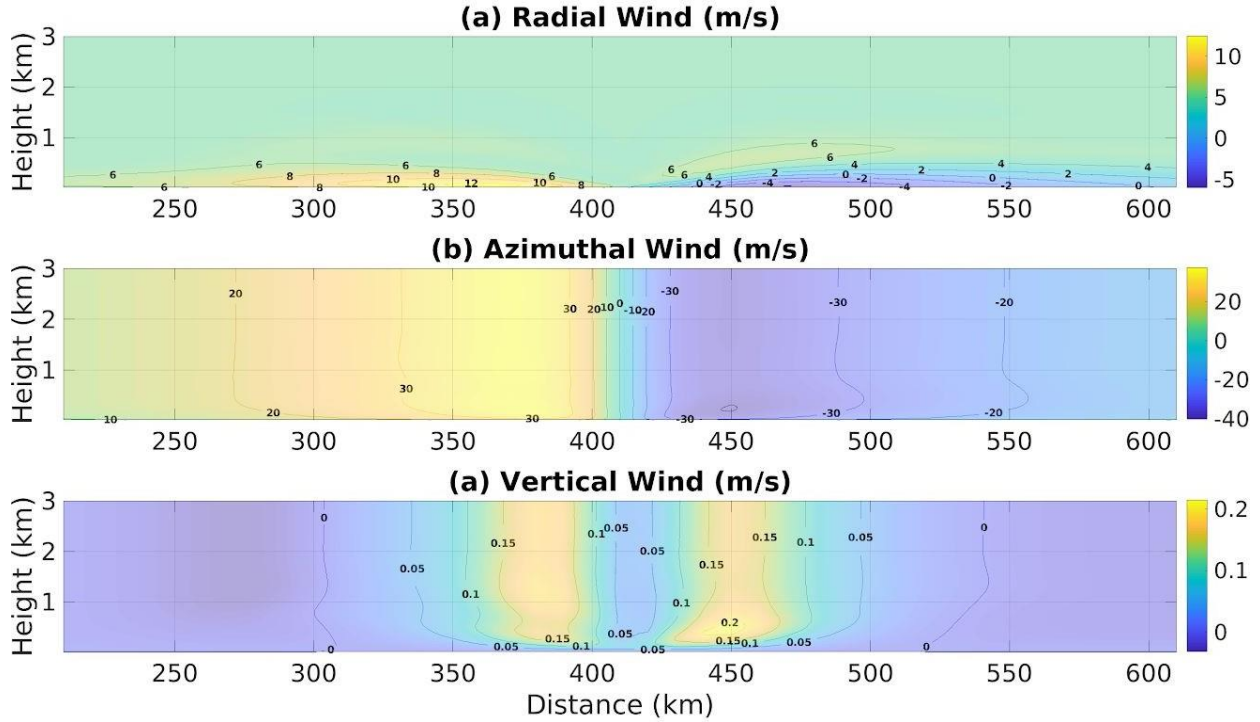


Figure 7: Cross sectional wind profiles of (a) radial wind, (b) azimuthal wind, and (c), vertical wind generated by experiment W_M. The center of the storm is at a distance of 410 km. The cross section travels from the south of the center of the storm to the north of the center of the storm.

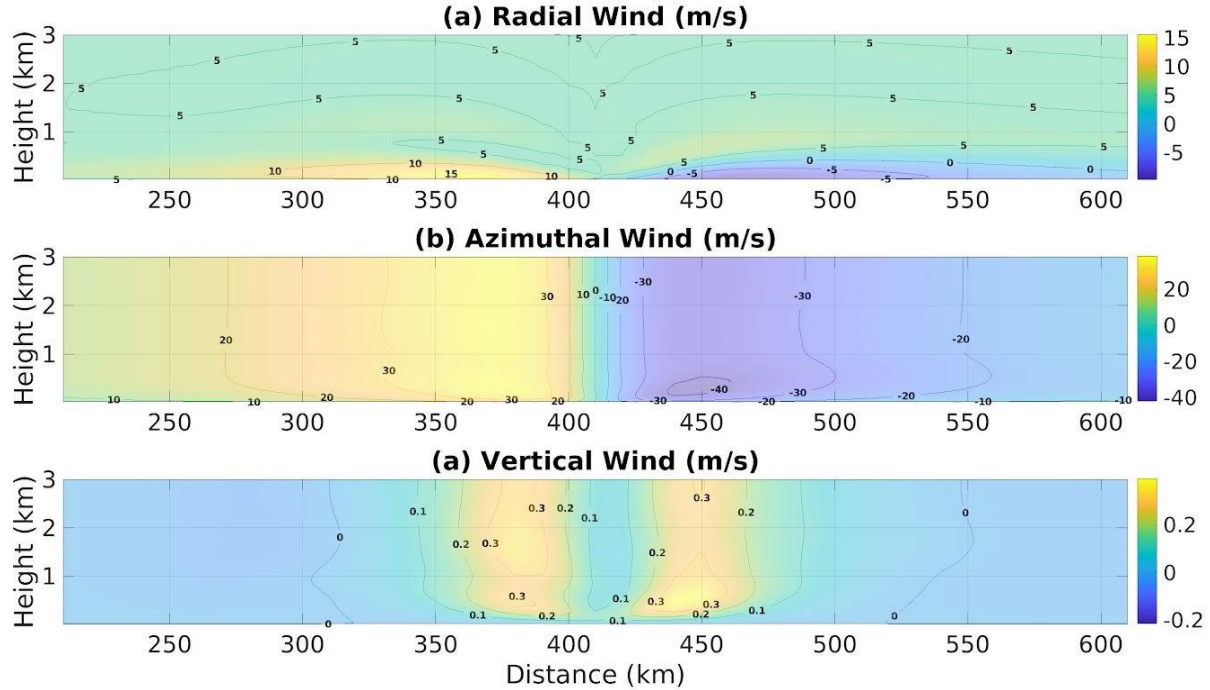


Figure 8: Cross-sectional wind profiles of (a) radial wind, (b) azimuthal wind, and (c), vertical wind generated by experiment L_M. The center of the storm is at a distance of 410 km. The cross section travels from the south of the center of the storm to the north of the center of the storm.

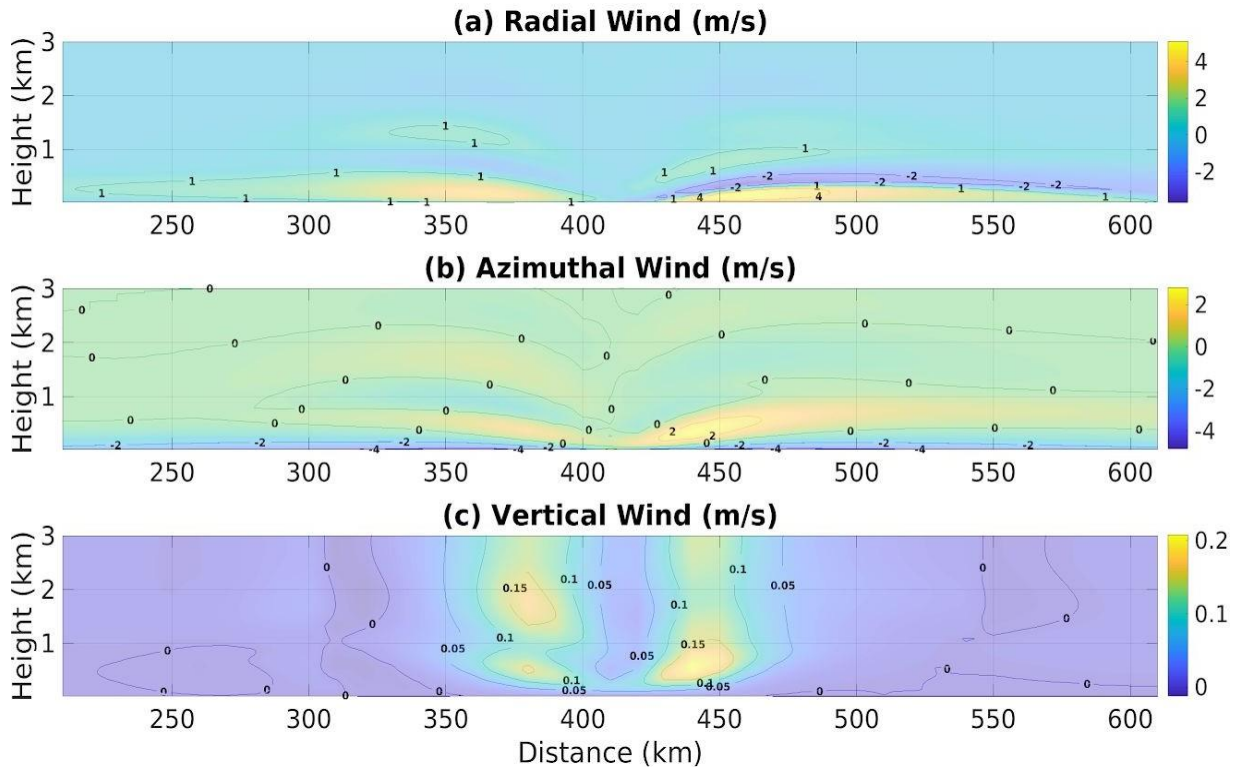


Figure 9: Cross-sectional wind profiles of (a) radial wind, (b) azimuthal wind, and (c), vertical wind generated by the difference between experiments W_M and L_M. The center of the storm

is at a distance of 410 km. The cross section travels from the south of the center of the storm to the north of the center of the storm.

There additionally appears to be signs of an internal wave travelling upwards as indicated by the positive and negative zones between zero contours. Finally, the vertical wind cross section reveals that the vertical velocity within the eyewall of the storm at the RMW1 is increased due to the land-induced enhanced convergence in the lower part of the boundary layer.

3.3. Characteristics of Rolls over Land

Delta is a derived quantity used to represent the height of the boundary layer. It was introduced by Kepert (2001) and used in GG14. It is defined as $\delta = \sqrt{2K/I}$ where K is the turbulent viscosity and I is the inertial stability parameter, given by

$$I = \sqrt{\left(f + \frac{2\bar{V}g}{r}\right)\left(f + \frac{\bar{V}g}{r} + \frac{\partial \bar{V}g}{\partial r}\right)}$$

where V_g is the gradient wind and f is the Coriolis parameter. GG14 Figure 9 provides evidence that greater Delta correlates with greater roll wavelength, while GG18 concludes that greater Delta correlates with lesser roll growth rates. Figure 10 uses data from all four experiments to display Delta profiles. In it, moving cases exhibit a consistently higher Delta than their corresponding stationary cases, consistent with GG18. Similarly, cases over land are consistently higher than cases over water.

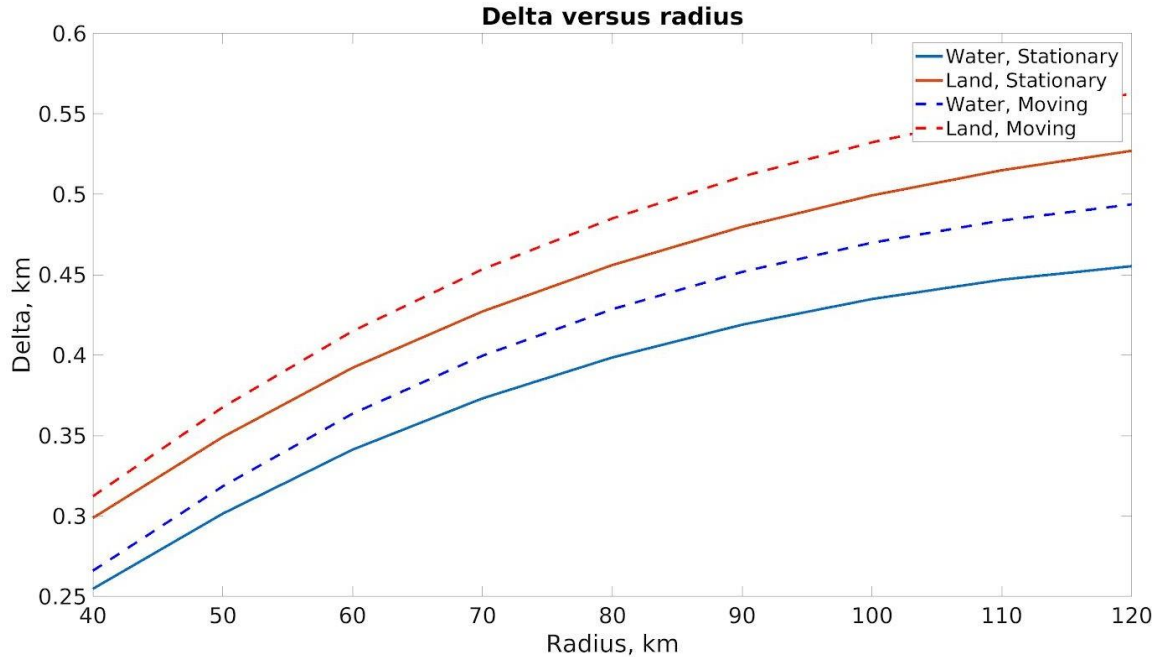


Figure 10: Delta as a function of radius derived from all four experiments. Moving cases use a profile to the right of the storm direction of motion.

Another derived quantity useful for characterizing rolls is Bulk Shear. Bulk Shear is defined by GG14 as \bar{u}_{max}/δ where \bar{u}_{max} is the maximum cross-roll mean wind and is

demonstrated in GG14 Figure 10 to be generally correlated with roll growth rates. Our Figure 11 consists of all four experiments' Bulk Shear profiles, with stationary cases possessing a consistently higher Bulk Shear than their moving counterparts and water cases also rating higher than their respective land cases.

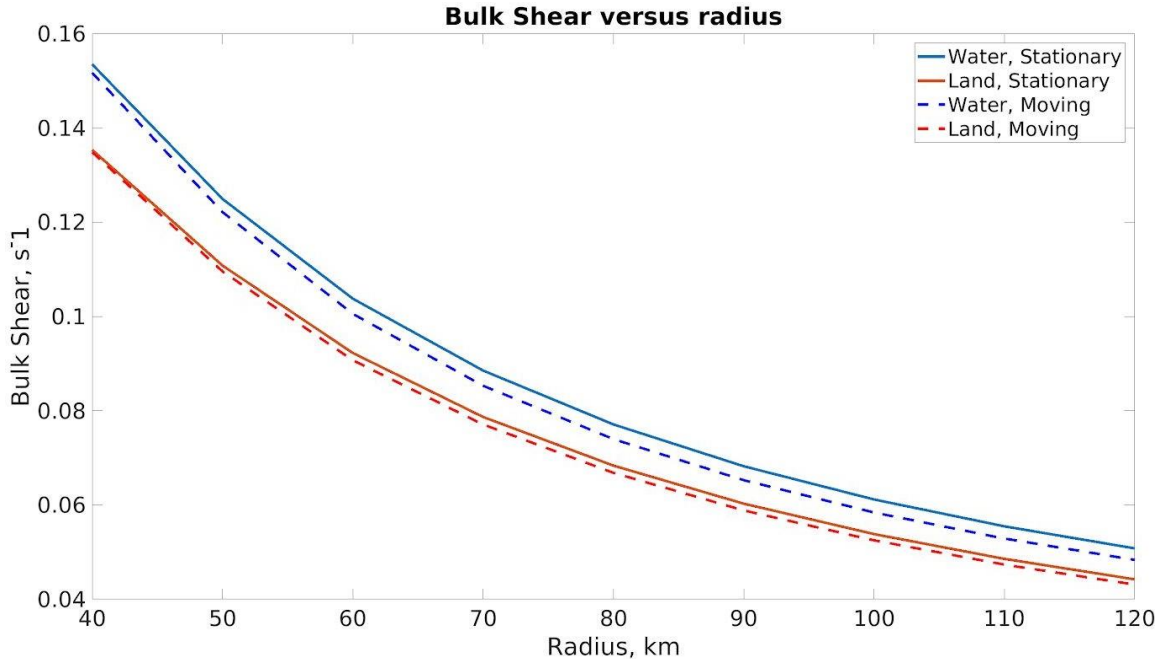


Figure 11: Bulk Shear as a function of radius derived from all four experiments. Moving cases use a profile to the right of the storm direction of motion.

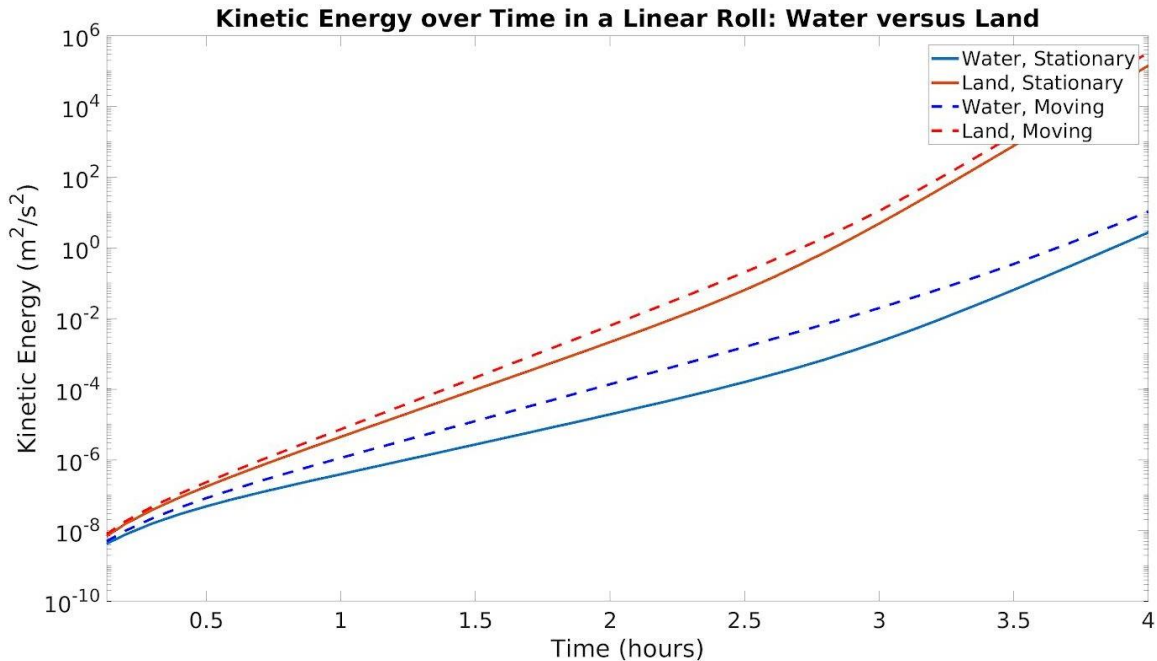


Figure 12: Kinetic energy as a function of radius derived from all four experiments. Moving cases use a profile to the right of the storm direction of motion.

Just as Delta and Bulk Shear describe the extent and growth of rolls, kinetic energy is a measure of a roll's total intensity. The kinetic energy of the rolls at RMW1 are shown in Figure 12. This mirrors the pattern in Figure 10, as moving and land cases greatly exceed stationary and water cases in terms of both Delta and kinetic energy, with land being the most prevalent factor.

Rolls can be visualized through a plot of their vertical wind velocity and streamlines, (Figures 13 and 14). Figure 13 is a snapshot from W_S, while Figure 14 is a snapshot from L_S. Both Figures 13 and 14 are at RMW1 in a stationary storm taken at 3 hours. The average magnitude of the vertical wind in Figure 14 is significantly higher than that of the vertical wind in Figure 13. The vertical and horizontal extent of the rolls are also larger as predicted by the measurements of Delta and kinetic energy in Figures 10 and 12.

4. Discussion

Of the factors that we examine in this study, the three of greatest concern are roll wavelength, roll growth rate, and roll intensity, represented by Delta, Bulk Shear, and kinetic energy. If we expected rolls to strengthen upon landfall, we would expect to see an increase in Delta and kinetic energy in the moving and land cases, whereas the opposite would be true if we expected rolls to weaken. Given the data presented in Figures 10 and 12, it appears that Delta and kinetic energy both increase as we simulate a storm with increased surface roughness. This in turn leads to a greater roll wavelength and intensity compared to the over water case, consistent with the differences between Figures 13 and 14.

However, the decrease in Bulk Shear from Figure 11 between the water and land cases would suggest that while the ultimate intensity of rolls increases, their growth rate slows. Despite this apparent decrease in growth, this does not appear to significantly influence the intensity of rolls after a short time given the results in Figure 12. It may be that the change in roll growth rate is not large enough to affect the growth of the linear phase rolls as simulated in this study.

5. Conclusions

Due to the increases in factors correlating with increasing roll wavelength and intensity, we conclude that rolls generally strengthen upon storm landfall. Given that rolls are not currently considered in storm intensity and damage forecasts, these findings present a new factor for future studies to consider when examining wind damage in a landfalling hurricane.

Acknowledgments

This study was supported by a Summer Undergraduate Research Fellowship in Oceanography (SURFO) (National Science Foundation REU grant # OCE- 1757572). Computational resources accessed remotely thanks to the Renaissance Computing Institute (RENCI) at UNC. Special thanks to Chris Kerr and Kun Gao for help in running models and analyzing model outputs.

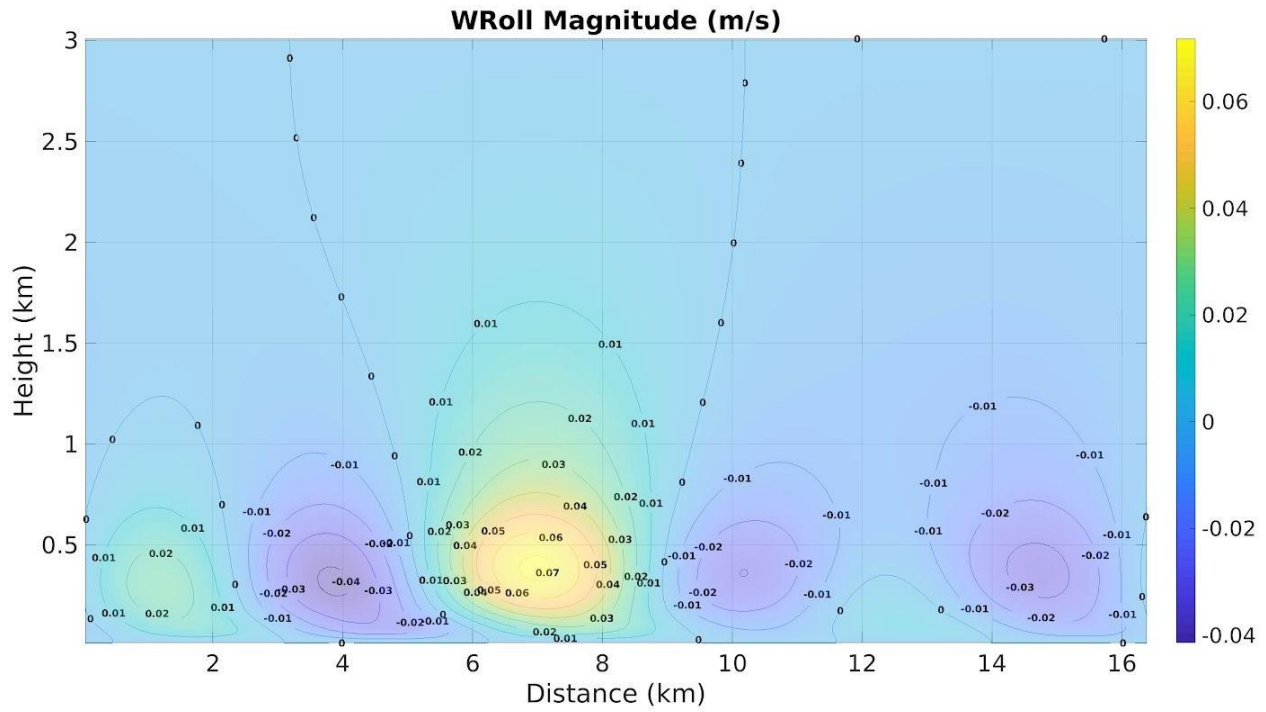


Figure 13: The vertical wind component in experiment W_S at 3 hours, RMW1.

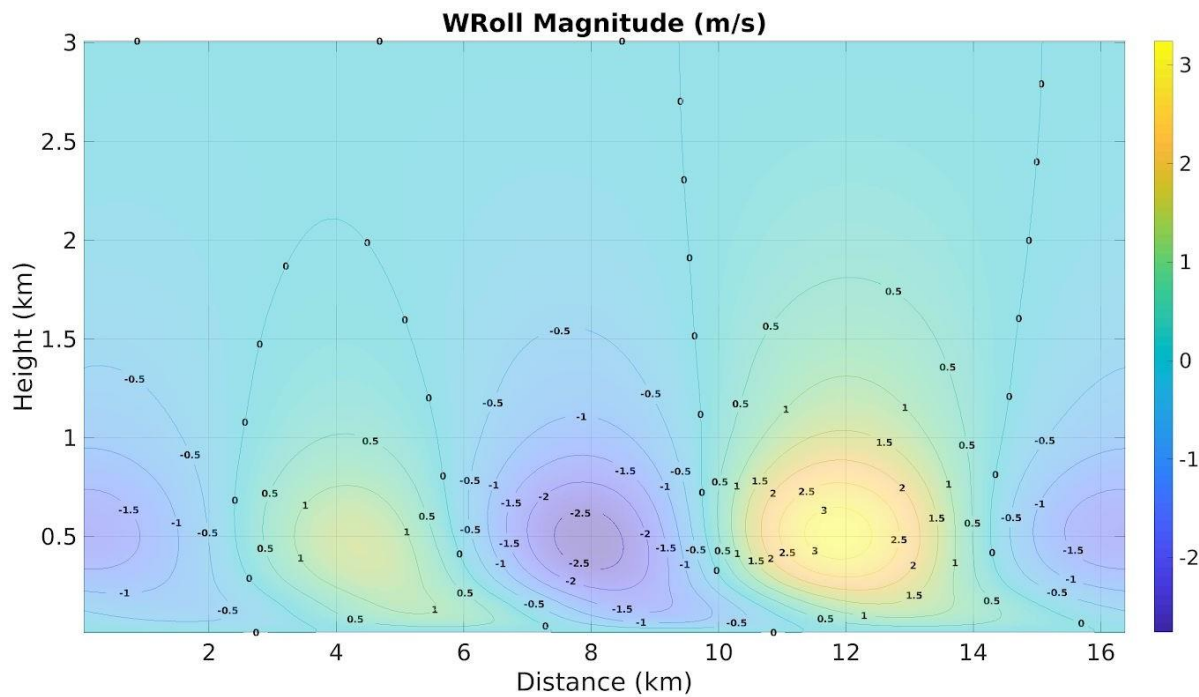


Figure 14: The vertical wind component in experiment L_S at 3 hours, RMW1.

References

- Ellis, R., and S. Businger, 2010: Helical circulation in the typhoon boundary layer. *J. Geophys. Res.*, 115, D06205, <https://doi.org/10.1029/2009JD011819>
- Foster, R. C., 2005: Why rolls are prevalent in the hurricane boundary layer. *J. Atmos. Sci.*, 62, 2647–2661, <https://doi.org/10.1175/JAS3475.1>.
- Gao, K., and I. Ginis, 2014: On the generation of roll vortices due to the inflection point instability of the hurricane boundary layer flow. *J. Atmos. Sci.*, 71, 4292–4307, <https://doi.org/10.1175/JAS-D-13-0362.1>.
- , and -----, 2016: On the equilibrium-state roll vortices and their effects in the hurricane boundary layer. *J. Atmos. Sci.*, 73, 1205–1222, <https://doi.org/10.1175/JAS-D-15-0089.1>.
- , -----, J. D. Doyle, and Y. Jin, 2017: Effect of boundary layer roll vortices on the development of an axisymmetric tropical cyclone. *J. Atmos. Sci.*, 74, 2737–2759, <https://doi.org/10.1175/JAS-D-16-0222.1>.
- , and -----, 2018: On the Characteristics of Linear-Phase Roll Vortices under a Moving Hurricane Boundary Layer. *J. Atmos. Sci.*, 75, 2589–2598, <https://doi.org/10.1175/JAS-D-17-0363.1>.
- Kepert, J. D., 2001: The dynamics of boundary layer jets within the tropical cyclone core. Part I: Linear theory. *J. Atmos. Sci.*, 58, 2469–2484, doi:10.1175/1520-0469(2001)058,2469:TDOBLJ.2.0.CO;2.
- Holland, G. J., 1980: An analytic model of the wind and pressure profiles in hurricanes. *Mon. Wea. Rev.*, 108, 1212–1218, doi:10.1175/1520-0493(1980)108,1212:AAMOTW.2.0.CO;2.
- Lorsolo, S., J. L. Schroeder, P. Dodge, and F. Marks, 2008: An observational study of hurricane boundary layer small-scale coherent structures. *Mon. Wea. Rev.*, 136, 2871–2893, <https://doi.org/10.1175/2008MWR2273.1>.
- Morrison, I., S. Businger, F. Marks, P. Dodge, and J. Businger, 2005: An observational case for the prevalence of roll vortices in the hurricane boundary layer. *J. Atmos. Sci.*, 62, 2662–2673, doi:10.1175/JAS3508.1.
- Nakanishi, M., and H. Niino, 2012: Large-eddy simulation of roll vortices in a hurricane boundary layer. *J. Atmos. Sci.*, 69, 3558–3575, <https://doi.org/10.1175/JAS-D-11-0237.1>.
- Wang, S., and Q. Jiang, 2017: Impact of vertical wind shear on roll structure in idealized hurricane boundary layers. *Atmos. Chem. Phys.*, 17, 3507–3524, <https://doi.org/10.5194/acp-17-3507-2017>.
- Wurman, J., and J. Winslow, 1998: Intense sub-kilometer boundary layer rolls in Hurricane Fran. *Science*, 280, 555–557, <https://doi.org/10.1126/science.280.5363.555>.
- Zhang, J.A., K. B. Katsaros, P. G. Black, S. Lehner, J. R. French, and W. M. Drennan, 2008: Effects of roll vortices on turbulent fluxes in the hurricane boundary layer. *Bound.-Layer Meteor.*, 128, 173–189, doi:10.1007/s10546-008-9281-2.

DEVELOPMENT OF THE INTERNAL STRUCTURE AND MECHANISM OF THE MULTIPURPOSE AUTONOMOUS UNDERWATER VEHICLE (MAUVE)

Nick Gershfeld^{1,2} and Mingxi Zhou¹

¹Graduate School of Oceanography, University of Rhode Island, Narragansett, RI, USA. ²Department of Mechanical Engineering, Cornell University, Ithaca, NY.

Abstract

In recent years, Autonomous Underwater Vehicles (AUVs) have been widely used in a variety of civilian, military, and oceanographic operations. All existing AUVs share the same operational schematics -- horizontal-flight with constrained pitch angle. Here, we present the design of a multipurpose AUV (MAUVE) with an emphasis on the internal structure and actuation mechanisms. The MAUVE will operate in horizontal-flying, vertical-descending, and hovering modes, controlled in part by adjusting its center of gravity relative to its center of buoyancy. The MAUVE is one-man portable, with a length of 1.5 meters and a weight around 20 kg. Payload space is also available for integrating additional sensors, e.g., imaging sonar, CTDs, and oxygen optodes. The MAUVE will be primarily used for coastal water profiling.

(The rest of this section is intentionally left blank)

Comparing phytoplankton carbon to volume relationships using three-dimensional (3D) and two-dimensional (2D) imaging

Courtney N. Hammond^{1,2}, Heather McNair¹, and Susanne Menden-Deuer¹

¹University of Rhode Island, Graduate School of Oceanography, Narragansett, RI, USA.

²Salisbury University, Salisbury, MD, USA.

Corresponding author: Courtney Hammond (courtney.nicole.hammond@gmail.com)

Running head: 3D volume and carbon relationships

Key Points:

- 3D and 2D modeling of phytoplankton cell volume
- volume to carbon relationships for phytoplankton

Key Index Words:

phytoplankton, carbon, biogeochemical cycling, cell volume

Abstract

Phytoplankton are a taxonomically and morphologically diverse group that plays a critical role in the cycling of carbon within marine ecosystems. The carbon-biomass of oceanic phytoplankton is often inferred from cell size distributions because cell carbon content scales with cell size. The current understanding in cell volume (V) to carbon content of phytoplankton comes from cells grown in replete conditions where volume has been calculated from a 2D image. To understand how carbon (C) to volume (V) relationships for 2D and 3D image analysis change in response to abiotic factors, cell size, carbon and nitrogen content and chlorophyll concentration were measured for six species in high and low light treatments. Carbon content ranged from 15 to 17,284 pg C cell⁻¹ and nitrogen ranged from 2 to 6,455 pg N cell⁻¹. Light treatment had no significant impact on C density (pg C cell⁻¹ or C μm⁻³ (p>0.05)). However, cellular carbon and nitrogen content decreased over time in both high and low light treatments, indicating a potential effect from nutrient stress. To relate our C: Vol measurements to established 2D relationships we compared calculated 2D volumes to 3D volumes that were measured using confocal-microscopy. 2D volumes that were geometrically determined were generally slightly higher than measured 3D volumes although the slope of the relationship between C and V was similar. The relationships for 2D calculated volumes were, pg C cell⁻¹ = 0.6 *volume^{0.725} and pg N cell⁻¹ = 0.033* volume^{0.88} while the relationships for 3D measured volumes were, pg C cell⁻¹ = 1.3*volume^{0.647}, and pg N cell⁻¹= 0.081 x volume^{0.798}. The lower volume measurement from the high-resolution 3D image indicates that estimations of cell carbon when using a 2D image are on average 20% higher. The consistence of C:V between light treatments suggests that the same relationship can be used to convert phytoplankton size to carbon throughout the euphotic zone. These results help constrain C:V relationships enabling deeper understanding of carbon cycling in the euphotic zone.

1. Introduction

Phytoplankton play an important role ecologically within freshwater and marine ecosystems by producing oxygen and fixing atmospheric carbon (Field et al. 1998). Phytoplankton convert atmospheric carbon into usable forms by other marine organisms and export to the deeper ocean. Their role as a carbon sink is essential to the transfer and contribution to the carbon cycle and other biogeochemical cycles (Nelson et al. 2016). To understand phytoplankton and their contribution to the carbon cycle, cell size or volume serve as a proxy for carbon. Previous studies have established these relationships mathematically and allow for conversion from readily measurable cell size to less tractable biomass. A study that has been cited extensively and plays an essential role in calculating carbon and nitrogen relative to cell size is Menden-Deuer and Lessard (2000). These relationships between cell size and carbon and nitrogen were established in nutrient, temperature and light replete conditions across a taxonomically diverse range of phytoplankton (Menden-Deuer and Lessard 2000).

Traditionally, cell volume has been determined two-dimensionally (2D) or geometrically through the use of light microscopy (Roselli et al. 2015). Cell length and width were measured and assumptions about depth were made. Advancements in technology allow for the use of modern computers to image phytoplankton three-dimensionally. Three-dimensional (3D) imaging provides a precise measurement of cell volume for phytoplankton that have complex shapes and features through confocal laser scanning microscopy coupled with image analysis systems (Roselli et al. 2015).

Techniques to visualize plankton has traditionally involved brightfield/darkfield, fluorescence and electron microscopy but confocal microscopy provides the opportunity to blend advancements in technology with digital imaging processing in order to provide a better understanding into the morphological and physiological characteristics of plankton (Lichtman 1994). A confocal microscope scans the planes of a specimen and produces a stack of thin images that provides a precise measurement of location (x and y coordinates) as well as depth (z coordinates). Image processing programs compile individual slices of images into three-dimensional reconstructions of the object (Lichtman 1994). Confocal microscopy has traditionally been used for biomedical research, but digital confocal microscopy provides more opportunity to understand smaller single-celled plankton (Verity et al. 1996).

To understand cell volume and other morphological characteristics, we must understand the environment in which phytoplankton are found. In dynamic ecosystems, like the ocean, abiotic factors like temperature, light and salinity are constantly changing and impacting productivity. With a changing world, we are interested in how phytoplankton are responding to these changes within oceanic environments. Zones of the ocean are classified by how much light penetrates at different depths. High concentrations of phytoplankton, like our algal blooms, concentrate closer to the surface within the euphotic zone in order to perform photosynthesis. Understanding how cellular carbon content of phytoplankton changes in response to light gives us an indication of biomass and contribution to the carbon cycle.

We measured how changes in cell volume affect carbon and nitrogen concentrations to indicate changes in biomass and how light alters these relationships within dynamic ecosystems. Having access to 3D imaging tools, we determined cell volume three-dimensionally as well as

two-dimensionally to compare precision of the two approaches and investigated how similar or different relationships are to previously established relationships for phytoplankton communities.

2. Materials and Methods

2.1. Preparing Cells for Harvesting and Placing in Treatments

Six different phytoplankton species were grown in f/2 media (Guillard 1975) without silicate added at a 12:12 dark:light cycle at 15°C; *Skeletenoma marinoi* (SM), *Heterocapsa triquetra* (HT), *Heterosigma akashiwo*(HA), *Ceratium lineatum*(CL), *Prorocentrum micans* (PM) and *Akashiwo sanguinea* (AS). 50:50 transfers of medium and culture were performed to ensure exponential growth of cells and high density needed to conduct chlorophyll and CHN analysis. 4.0 L of culture and medium were split into six 1.0-L bottles (~600 mL per bottle) for each species. Triplicate bottles were then placed in two different light intensities; with a high light treatment of 12 hour light: 12 hours dark at 100 μmol photons $\text{m}^{-2} \text{s}^{-1}$ and a low light treatment at ~15 μmol photons $\text{m}^{-2} \text{s}^{-1}$. Low light levels were obtained by covering bottles in mesh. Each bottle was sampled at each time interval for cell counts, cell volume imaging, filtered for CHN and chlorophyll analysis. Bottles were sampled at three time points; initial time (T0), twenty-four hours later (T24) and seven days later (TF). *Akashiwo sanguinea* is not included in the data analysis because cultures were not sufficiently dense at any harvesting time to get accurate CHN values or cell volume measurements.

2.2 Cell Counting

10 mL of culture was removed from each bottle and pipetted into glass scintillation vials for each species at T0, T24 and TF. 1-2 drops of Lugol's Iodine solution was added to preserve the cell samples. Cell counts were performed in a 1-mL Sedgewick-Rafter counting chamber. Dense cultures were counted until 500 cells were reached. Chain forming phytoplankton were counted by determining average number per chain and then counting 500 chains.

2.3 Chlorophyll a Extraction

Chl a concentration was determined from triplicates in each bottle at each time interval. 5 to 50 mL subsample was extracted within 3 mL of 96% ethanol, kept in dark conditions and determined twenty-four hours later using the Turner Designs 8000-010 Aquafluor Handheld Fluorometer/Turbidimeter. If chlorophyll concentrations were too dense and above the RFU detection limit of the fluorometer, 1:20 dilutions were performed. *Prorocentrum micans* and *Akashiwo sanguinea* were extracted in 6 mL of ethanol and read on a Turner 10-AU Fluorometer.

2.4 Carbon-Nitrogen (CHN) Content Analysis

25-mm GF/F filters were combusted at 500 °C for 4 hours. 50 mL was filtered from each bottle at every time point and f/2+Si and f/2-Si blanks were filtered onto 25-mm GF/F filters using a vacuum pump filtration system. Filters were placed in sterile petri dishes and frozen (-20°C) until analysis. To prepare for CHN analysis, filters were dried in a drying oven at 60 °C overnight. Filters were prepared and packaged within a sterile environment on top of aluminum black and materials were cleaned in between samples with ethanol. Filters were cut in half and the mass was recorded for each half. Each sample was packaged into a spherical shape and deposited into 9x 10 mm tin capsules to be read on an elemental analyzer. The other half served as an archive in case of needed replication. Samples were processed at the University of Rhode

Island for bulk carbon and nitrogen analysis using an Exeter Analytical CE-440 elemental analyzer.

2.5 Determining Cell Size Two-Dimensionally and Three-Dimensionally

Subsamples from each bottle were transferred to 5- μ L cryovials and preserved with 1% glutaraldehyde. To accurately measure cellular volumes using confocal microscopy, the cell walls needed to be fluorescent. The silica frustule of *S. marinoi* was stained with PDMPO (Lysosensor DND 160 Yellow/Blue) that was added to the growing culture. The thecate dinoflagellates, *C. lineatum*, *H. triquetra*, and *P. micans*, were stained with the cellulose binding dye, calcofluor white. The cell outline of the remaining unarmored species was determined based on chlorophyll fluorescence because the cells had chloroplasts that lined the cell wall.

Sparse phytoplankton cells were concentrated by centrifuging a subsample and removing supernatant. Up to 300 μ L of the sample along with stain (~20 μ L) were pipetted into a PerkinElmer CellCarrier 96 ultra well plate. The plate was placed into the Opera Phenix™ High Content Screening System. Using the instrument specific Harmony™ software automates the process from signal acquisition to analysis and evaluation. Cells were imaged using the confocal capabilities and z-stacking with 40x or 20x water immersion objectives. Image analysis was done with the Opera Phenix software, Harmony, which calculates the volume of 3D rendered objects. To compare these high-resolution volume metrics to previous methods, a confocal image was converted to a 2D maximum projection and the Harmony software was used to measure the major and minor axes of each cell in an image. Volumes from the 2D images were determined geometrically using the given equations of a prolate spheroid, sphere or cylinder (Hillebrand et al 1999).

2.6 Statistical analysis

All statistical analysis were performed using R. It was necessary to perform linear regressions with log-transformed data to normalize the distribution of residuals. A least squares linear regression was used to determine the relationships between cell volume and the amount of carbon and nitrogen in each cell. A model II linear regression was performed to quantify the relationship between the 2D and 3D volume measurements. ANOVAs were performed with a nested species factor to test for significant changes in cell size, carbon and nitrogen content with changes in light level and time.

3. Results

3.1 Two-dimensional versus three-dimensional measurements

The two different methods of measuring cell volume: two-dimensional (2D) and three-dimensional (3D) overall were nearly identical (Figure 1). The slope between 3D cell volume and 2D was close to unity, 1.12, ($R^2 = 0.95$) with a 95% CI of 1.105 to 1.19. While the measurement method did not matter when comparing across a wide range of sizes, on a species-specific basis, the measurement method did matter (ANOVA, $p << 0.001$). Generally, 2D volume and 3D volume measurements where the species with the greatest difference between measured 2D and 3D volumes were the smaller phytoplankton *S. marinoi* and *H. akashiwo* (Figure 2). 2D volume was 30% higher for *Heterosigma akashiwo* and 43% higher for *Skeletonema marinoi* indicating potential over estimation of carbon when determining cell volume two-dimensionally relative to three-dimensional measurements. In phytoplankton communities where three-dimensional volume measurements were greater than two-dimensional

measurements, percent difference was low with *H. triquetra* exhibiting 2D volume measurements 12% lower and *P. micans* 5% lower. This difference is accounted for the higher variability in cell volume, as indicated by a higher coefficient of variation.

The coefficient of variation (C.V) for 2D cell volume ranged from 4 to 23% while the C.V for the 3D volume ranged from 5 to 27%. While CV was similar between measurement methods, generally the 3D rendering showed a tighter distribution. Generally, smaller cells such as *S. marinoi* and *H. akashiwo* exhibited lower coefficient of variation for 3D (~5% C.V) than the 2D volume measurements (~12-14 % C.V). The decrease in variability is attributed to the high density at which the cells were able to reach and provide a better representation of cell volume.

3.2 Cell Volume and Carbon and Nitrogen Relationships

There was a positive relationship between cell volume and cellular carbon (pg C cell^{-1}) and nitrogen (pg N cell^{-1}). As cell volume increased, the amount of carbon and nitrogen per cell increased (Figure 2). 3D and 2D measurements of cell volume exhibited similar volume to carbon and nitrogen relationships. Carbon content ranged from 15 to 17,284 pg C cell^{-1} and nitrogen ranged from 2 to 6,455 pg N cell^{-1} . Logarithmic regression equations indicate that the elemental composition dependence on size was very similar between 3D and 2D measurements for carbon and nitrogen. Carbon and volume relationships can be expressed mathematically for 3D measurements: $\text{pg C cell}^{-1} = 1 \text{ pg C cell}^{-1} = 1.3 * \text{volume}^{0.647}$, and $\text{pg N cell}^{-1} = 0.081 \times \text{volume}^{0.798}$ or for 2D measurements: $\text{pg C cell}^{-1} = 0.6 * \text{volume}^{0.725}$ and $\text{pg N cell}^{-1} = 0.033 * \text{volume}^{0.88}$. The slope for C: vol relationships for both 2D and 3D measurements is less than 1 indicating that smaller cells are proportionally more dense than larger cells. $\text{C } \mu\text{m}^{-3}$ ranges from 0.00086 to 0.0292 with smaller cells, *Skeletenoma marinoi* exhibiting higher concentrations than larger cells, such as *Ceratium lineatum*.

3.3 Effect of Light Treatments Over Time

The light treatments did not affect cell volume ($p = 0.65$) nor cell carbon content ($p = 0.81$). On the other hand, nitrogen appeared to be significantly impacted by treatment ($p = 0.003$), with the low-light cells having significantly more N (Figure 3). Time did not impact cell volume ($p = 0.35$) but there was a significant decrease of pg C cell^{-1} within all phytoplankton species over time (Figure 4a, $p << 0.001$), as well as a decrease in $\text{pg N}^{-1} \text{ cell}$ (Figure 4b, $p = 0.007$). Chlorophyll changed significantly with treatment ($p = 0.02$) and over time ($p < 0.001$). Chlorophyll a increased over time but was higher in low light conditions comparative to high light conditions. Carbon and nitrogen ratios ($\text{pg C cell}^{-1}/\text{pg N cell}^{-1}$) remained constant at around 6 while *S. marinoi* remained at a constant level of above 8 (Figure 5). C:N ratios dramatically increased over time ($p = 0.008$) indicating that the rate of change for carbon was greater than that of nitrogen.

4. Discussion

The data presented here suggest that higher-resolution imaging does not significantly change cell volume measurements as seen in the nearly 1:1 slope of volume estimated using the 3d rendered confocal images versus the volume estimated from the 2D images. Thus, in most cases, instrumentation that either calculates volume from a 2D image or calculates volume based on

estimated spherical diameter will be sufficient for measuring cell size. Similar to previous studies, we find a strong relationship between cell size and carbon and nitrogen content.

We see a positive trend between cell volume and carbon and nitrogen, similar to that of Menden-Deuer and Lessard (2000). Our obtained regression predicts that smaller cells exhibit higher concentrations of carbon and larger cells exhibit lower concentrations of carbon than previously established logarithmic relationships. On the other hand, we would expect lower concentrations of nitrogen across all size classes. The logarithmic relationship from the Menden-Deuer and Lessard paper ($m = 0.939$) indicates a greater rate of change in volume and carbon relationships comparative to our obtained value ($m = 0.679$). Carbon to nitrogen ratios were generally higher than those previously established (Menden-Deuer and Lessard 2000).

There are a few possible explanations for the differences between this study and Menden-Deuer and Lessard (2000). One possible explanation could be in the number of species that were used to create the carbon:volume relationship. Here, we use six diverse phytoplankton species, while the regression from Menden-Deuer and Lessard (2000) compiled data from experiments and literature to create a regression with >45 different phytoplankton species. Thus, it could be just by chance that we selected species that have slightly less carbon and nitrogen content than the global average. Another difference could arise from time of analysis. In this study, our regression was performed with exponentially growing cells that were growing in replete f/2 medium and harvested 24 h after transfer. As we saw in our time-series analysis, carbon content changes with time were likely due to changes in nutrient availability. Thus, differences in carbon and nitrogen content could arise from differences in media nutrient concentrations at time of harvest.

Although chlorophyll *a* can serve as a proxy for biomass in phytoplankton studies, chlorophyll *a* alone cannot be used to estimate phytoplankton carbon (Verity et al. 1996). Using 2D and 3D imaging to measure cell size provides a way to convert a wide range of sizes for phytoplankton into quantifiable forms of carbon. Being able to mathematically relate size and carbon allows to better model how the input of phytoplankton into the carbon cycle impacts global biogeochemical cycles.

5. Conclusions

Advancements in technology allow us to determine cell volume three-dimensionally and compare it to historical methods of determining cell volume two-dimensionally. Understanding how factors such as light and time impact cell volume provides an idea on how abiotic factors affect other cell components such as carbon, nitrogen and chlorophyll. By understanding these relationships, researchers can better model phytoplankton responses within dynamic environments.

Acknowledgments

Courtney N. Hammond was supported by a Summer Undergraduate Research Fellowship in Oceanography (SURFO) (National Science Foundation REU grant # OCE- 1757572). Thank you to Pat Kelly for help with carbon analysis and Vinka Craver for help imaging and processing confocal microscopy data. Experiment supplies and analysis were supported by a NASA Exports grant awarded to Susanne Menden-Deuer. The Opera Phenix imaging and analysis were supported by a grant awarded to Vinka Craver.

References

- Field C.B. Behrenfeld, M.J, Randerson J.T, Falkowski P. 1998. Primary production of the biosphere: Integrating terrestrial and oceanic components. *Science*. 281(5374):237-240.
- Guillard, R.R. 1975. Culture of phytoplankton for feeding marine invertebrates. In W. L. Smith and M. H. Chanley. [eds.], *Culture of marine invertebrate animals*. Plenum.
- Hillebrand, H.C, Duerselen,D. Kirschelt, U. Pollingher, and T. Zohary. 1999. "Biovolume calculation for pelagic and benthic microalgae". *J. Phycol.* 35: 403–424.
- Menden-Deuer, Susanne, and Evelyn J. Lessard. 2000. "Carbon to Volume Relationships for Dinoflagellates, Diatoms, and Other Protist Plankton." *Limnology and Oceanography*, 45: 3: 569–579
- Nelson, N. B., Siegel, D. A., Carlson, C. A., & Swan, C. M. (2010). Tracing global biogeochemical cycles and meridional overturning circulation using chromophoric dissolved organic matter. *Geophysical Research Letters*, 37(3)
- Lichtman, J.W.1994. "Confocal Microscopy." *Scientific American*, 27: 40–45.
- Roselli, L., et al. 2015. "New Data-Driven Method from 3D Confocal Microscopy for Calculating Phytoplankton Cell Biovolume." *Journal of Microscopy*, 258: 3: 200–211
- Verity, P. G., et al. 1996. "Visualization and Quantification of Plankton and Detritus Using Digital Confocal Microscopy." *Aquatic Microbial Ecology*, 10:55–67.

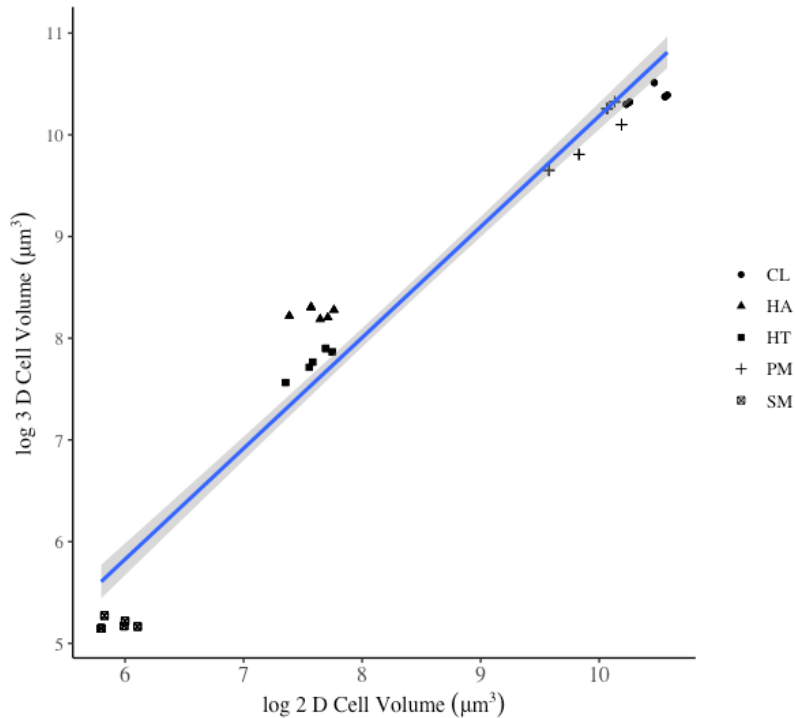
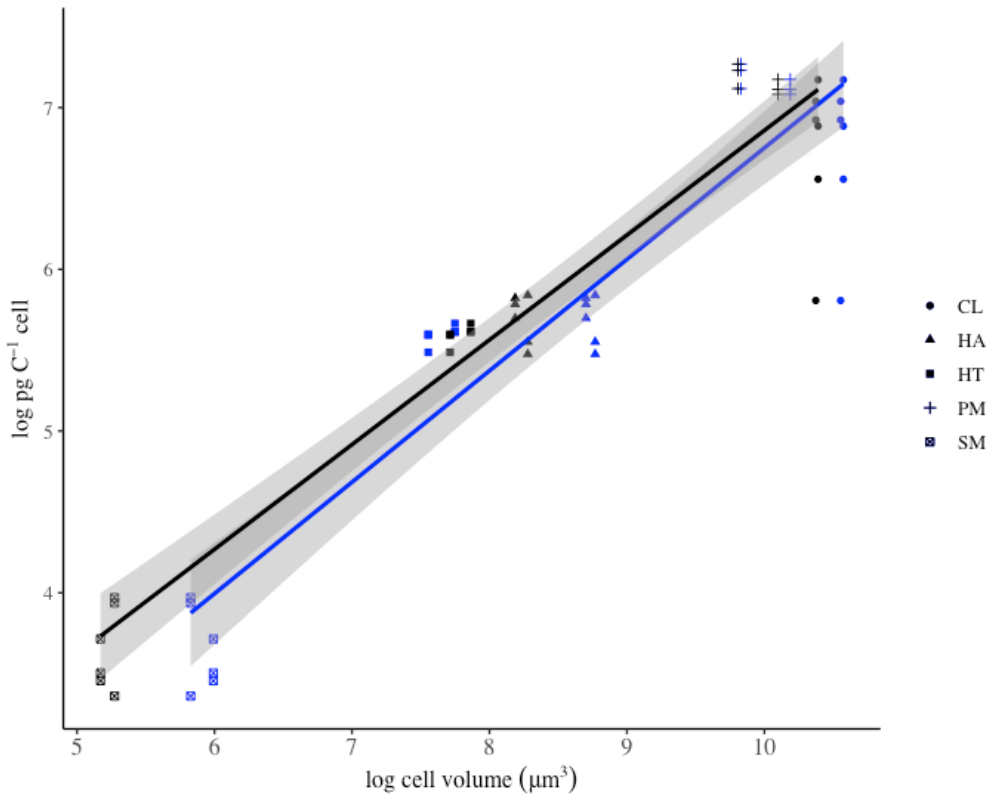


Figure 1. Log of the linear regression relationships between two-dimensionally (2D) and three-dimensionally (3D) determined cell volume (μm^3) for CL (*Ceratium lineatum*), HA (*Heterosigma akashiwo*), HT (*Heterocapsa triquetra*), PM (*Prorocentrum micans*) and SM (*Skeletonema marinoi*).

a)



b)

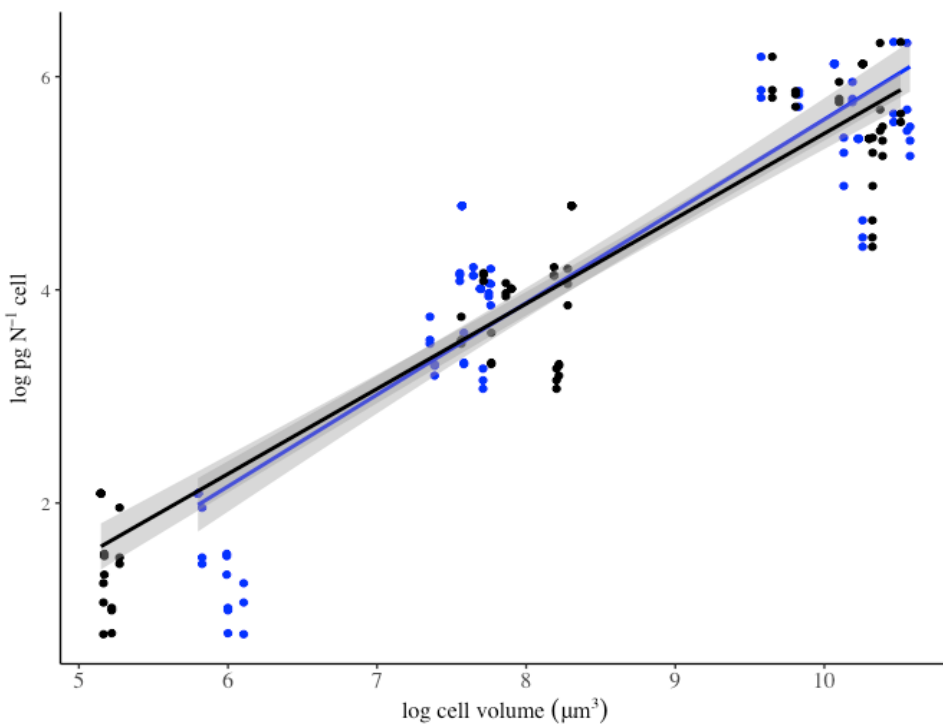


Figure 2. Log of carbon (a) and nitrogen concentrations (b) (pg C cell^{-1} and pg N cell^{-1}) versus cell volumes obtained through three-dimensional (3D - black dots) and two-dimensional (2D- blue dots) analysis.

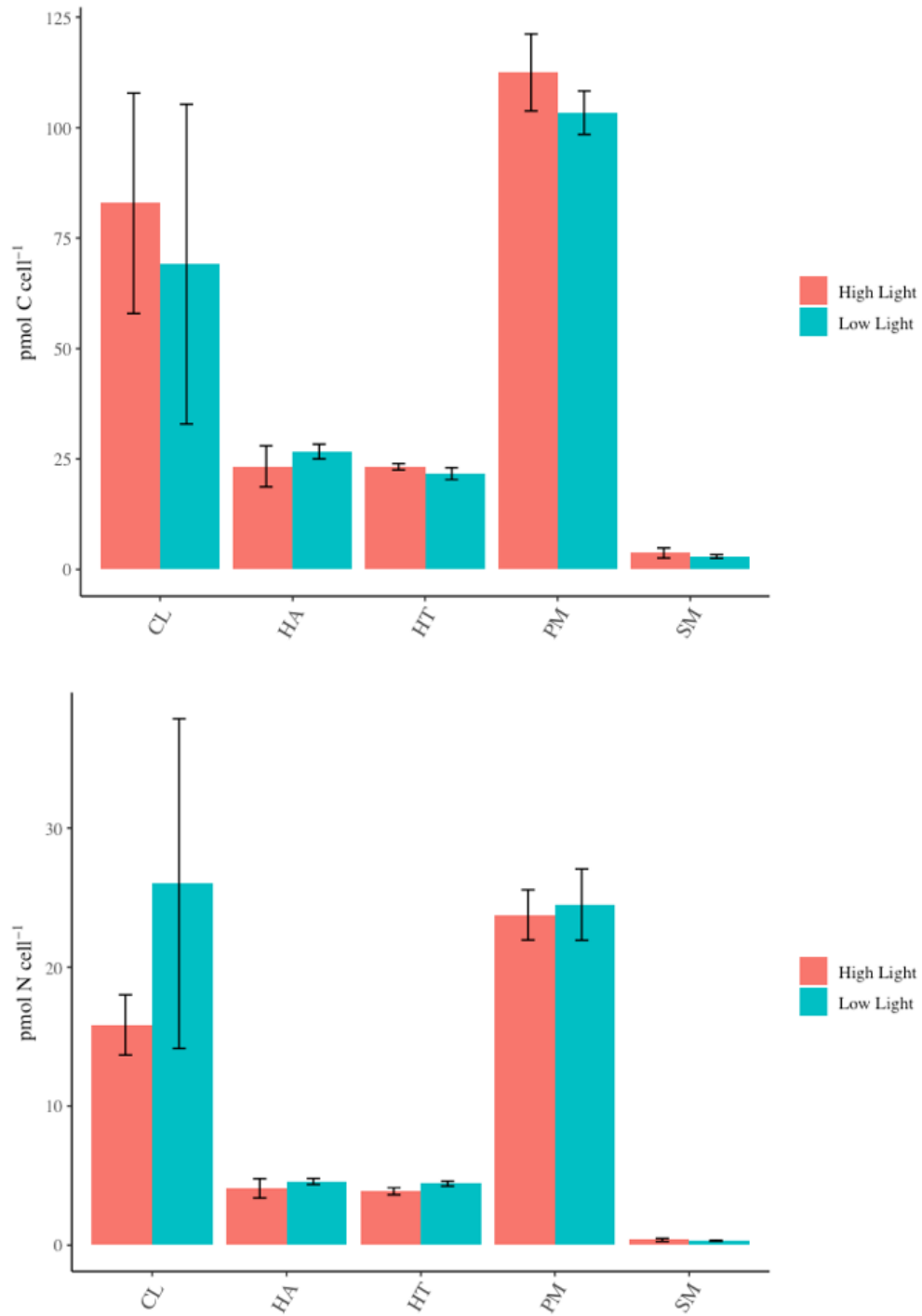


Figure 3. Carbon (pmol C cell⁻¹) was not affected by light treatment whereas nitrogen (pmol N cell⁻¹) significantly was affected by light treatment across six species of phytoplankton.

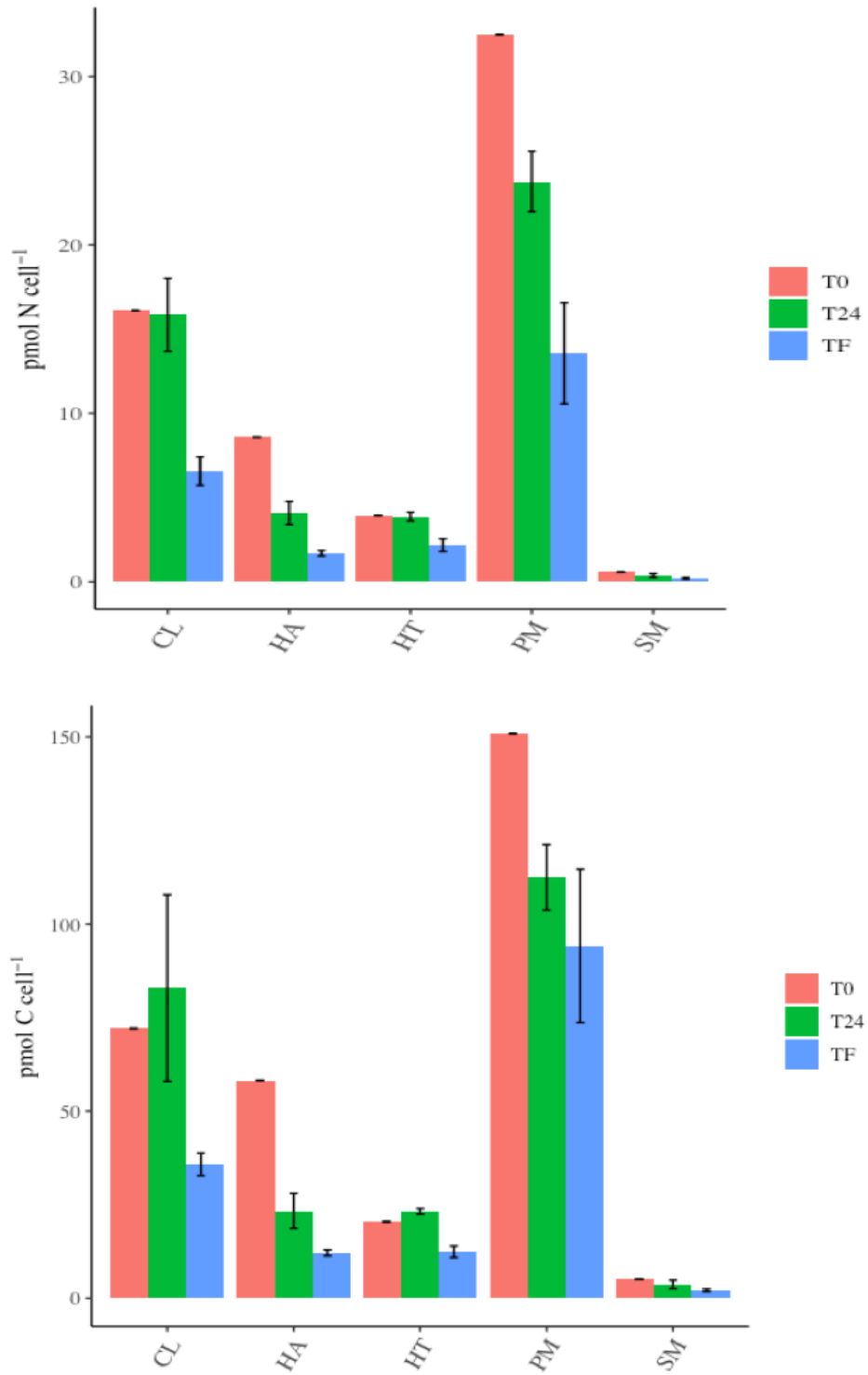


Figure 4. Changes in a) pmol N cell^{-1} and b) pmol C cell^{-1} over three time intervals; T0 , T24 (24 hours) and TF (168 hours) for five species of phytoplankton.

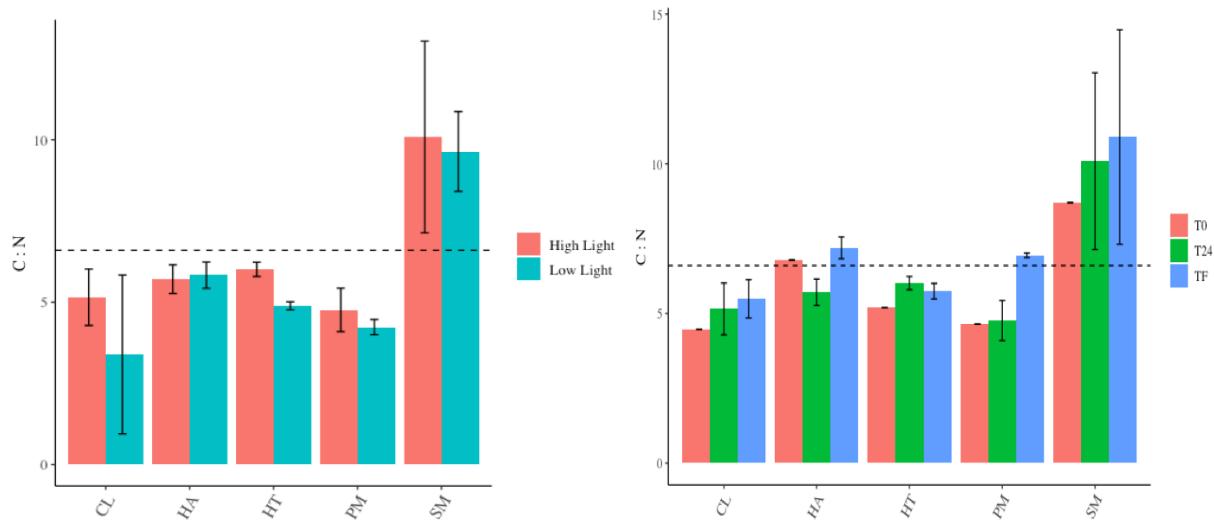


Figure 5. Carbon and nitrogen ($\text{pg C cell}^{-1}/\text{pg N cell}^{-1}$) ratios for phytoplankton relative to a) light treatment and b) ratios increase over the three time intervals; T0, T24 (24 hours) and TF (168 hours).

Table 1. Average width (μm), length (μm), calculated two-dimensional (2D) volume (μm^3), three-dimensional (3D) volume obtained from the Opera Phenix™ and coefficient of variation (C.V).

Species	Width	Length	2D Volume	C.V	3D Volume	C.V
<i>Skeletonema marinoi</i>	4.3	6.4	384.1	12.8	180.7	5.2
<i>Heterocapsa triquetra</i>	13.7	21.2	1989.8	14.6	2365.4	12.9
<i>Heterosigma akashiwo</i>	9.9	15.6	6270.8	4.2	3789.5	5.1
<i>Prorocentrum micans</i>	27.2	51.4	21642.7	23.3	23396.4	27.5
<i>Ceratium lineatum</i>	25.6	95.1	33730.6	16.0	32292.2	8.5
<i>Akashiwo sanguinea*</i>	32.1	56.8	38684.9	18.5	115970.8	63.1

Mapping of Tectonic Features Submerged Beneath Lake Azuei, Haiti: Implications for Seismic Hazards

Kamal R. James^{2†}, Marie-Hélène Cormier ¹, and Heather Sloan²

¹University of Rhode Island Graduate School of Oceanography, Narragansett RI

²Lehman College, City University of New York, Bronx, NY

† Brooklyn College, City University of New York, Brooklyn, NY

kamal.james25@bcmail.cuny.edu

Key Points:

- Sonar data are used to inventory morphotectonic features related to motion along the N. American - Caribbean plate boundary
- This inventory of morphotectonic features will prove useful in producing a geological map of Lake Azuei
- Preliminary analysis reveals the geometry of active faults, en echelon folds, and an area with liquefaction features

Key Index Words: Haiti, Lake Azuei, transpression, plate motion, plate boundary, CHIRP sonar, echosounder, tectonic deformation, morphology, transform fault

Abstract

The boundary between the North American and Caribbean plates traverses the Island of Hispaniola, which comprises Haiti and the Dominican Republic. The relative motion across that plate boundary is “transpressional”, a mix of shear motion and convergent motion. The structure and geometry of this broad plate boundary are still poorly constrained. Lake Azuei may overlie or be bounded by the Enriquillo-Plantain Garden Fault Zone (EPGFZ). In 2010, the abutting Leogane fault located about 60 km to the west of the lake ruptured in a devastating M7.0 earthquake (death toll: ~ 200,000). The earthquake displaced 1.3 million people and created \$7.8 billion in damages, confirming the high seismic risk within the region. Lake Azuei represents an ideal location for investigating complex tectonic deformation across this broad plate boundary, prompting a detailed geophysical survey across the lake in January 2017. Roughly 200 km of the high-resolution seismic profiles collected in 2017 have been inspected using the interpretive software “OpendTect”. This dataset was complemented with the analyses of another ~ 200 km of seismic profiles from two other sonar dataset acquired in 2013. The objective is to interpret and precisely locate morphological features including faults, folds, and slope breaks and produce an interpretative map of these features. This information will contribute to our understanding of crustal deformation across the diffused Caribbean-North American plate boundary. In addition, determining the geometry of the fault system will provide critical information for government agencies in mitigating seismic risks and locating critical infrastructures such as schools and hospitals.

1. Introduction

The North American- Caribbean boundary cuts through the island of Hispaniola. Relative motion across this diffuse plate boundary is transpressional, a combination of strike-slip and

convergent forces, which is partitioned between two sets of tectonic features rather than occurring on a single fault or within a narrow zone of deformation (e.g., Mann et al., 1995; Calais et al., 2010). The strike-slip component of relative motion is accommodated along two EW transform faults separated by ~150 km: The Septentrional fault in the north, and the Enriquillo-Plantain Garden fault (EPGF) in the south (Figure 1). Each fault accommodates roughly 1 cm/yr of left-lateral or sinistral slip (Symithe & Calais, 2016). The convergent component of relative motion is mostly accommodated across a broad “fold-and-thrust belt” that trends NW-SE, located between the two transform faults. Plate boundaries are the locus of most earthquakes, and are therefore seismically hazardous. This was exemplified by the devastating January 12, 2010 Mw7.0 earthquake resulting in an estimated ~200,000 deaths, 1.3 million people displaced and \$7.8 billion in damages (World Bank, 2010). While this broader context of plate motion is well understood, the precise geometry of the structures that accommodate this transpressive motion is not. This is critical information for any meaningful assessment of the seismic hazard facing the people of Hispaniola. To answer this question, a geophysical survey was carried out in Lake Azuei in 2017. Lake Azuei, known locally as “Etang Saumâtre”, is the largest lake in Haiti and is located between the two transform fault systems. The EPGF system is located near its southern shore, but where exactly remains controversial to this day. Lakes offer a unique opportunity to image geological structures: compared to terrestrial environments, sedimentation in lakes is more continuous, is not disrupted by human activity, and is not subject to intense erosion. Therefore, sediment stratigraphy and morphology are assumed to continuously record tectonic deformation in exquisite details. In addition, seismic reflection method, which is used to image the sediment stratigraphy beneath linear survey tracks, is easier, faster and more economically employed over water than on land. Here, we have inspected ~ 265 km of high-resolution seismic reflection data (CHIRP) as well as 140 km of echosounder data acquired in Lake Azuei to produce an inventory of tectonic features beneath the lake. This information is then used to establish a geologic map of the lake bottom.

2. Materials and Methods

2.1 CHIRP data analysis and interpretation

A geophysical survey conducted in January 2017 in Lake Azuei, Haiti collected three sediment cores, 220 km of multichannel seismic reflection (MCS) data, and ~200 km of high-resolution sub-bottom profiling (“CHIRP”) data (Cormier and Sloan, 2017). Data from the 2017 survey were complemented with two surveys consisting of ~65 km CHIRP data (Wang et al., 2018) and 140 km of echosounder data (Moknatian et al., 2017) (Figure 2).

The echosounder data were graciously provided to us by Prof. M. Piasecki and Dr. Mahrokh Moknatian of City College (CUNY), as a single file containing the depth sounding information as “latitude, longitude, and depth” triplets. These data were separated into a set of roughly linear profiles labeled 1 through 31 (see map in appendix 2) and distance along individual profile were computed in order to display each as depth-versus-distance graphs (see appendix 3). Morphological features were identified from these graphs, their approximate distance noted, and the corresponding latitude, longitude pair were then retrieved from the data files.

Visualizing and interpreting the CHIRP data required the use of the software Opendtect (<https://www.opendtect.org>). Opendtect is a free, open source software that allows the interactive visualization and interpretation of MCS and CHIRP data, in two and three dimensions. This software displays the lake bed and the sedimentary layers beneath, called seismic horizons.

Morphological features including an ~11-m paleoshoreline, troughs, break in slopes, faults, soft sediment deformation, and fold axes were characterized throughout and beneath the lake bed with the intent of constraining fault geometry and vertical deformation. These picks are listed in Appendix 4. Lastly, the mapping software GMT (<https://www.soest.hawaii.edu/gmt/>) was used in order to graphically present the data.

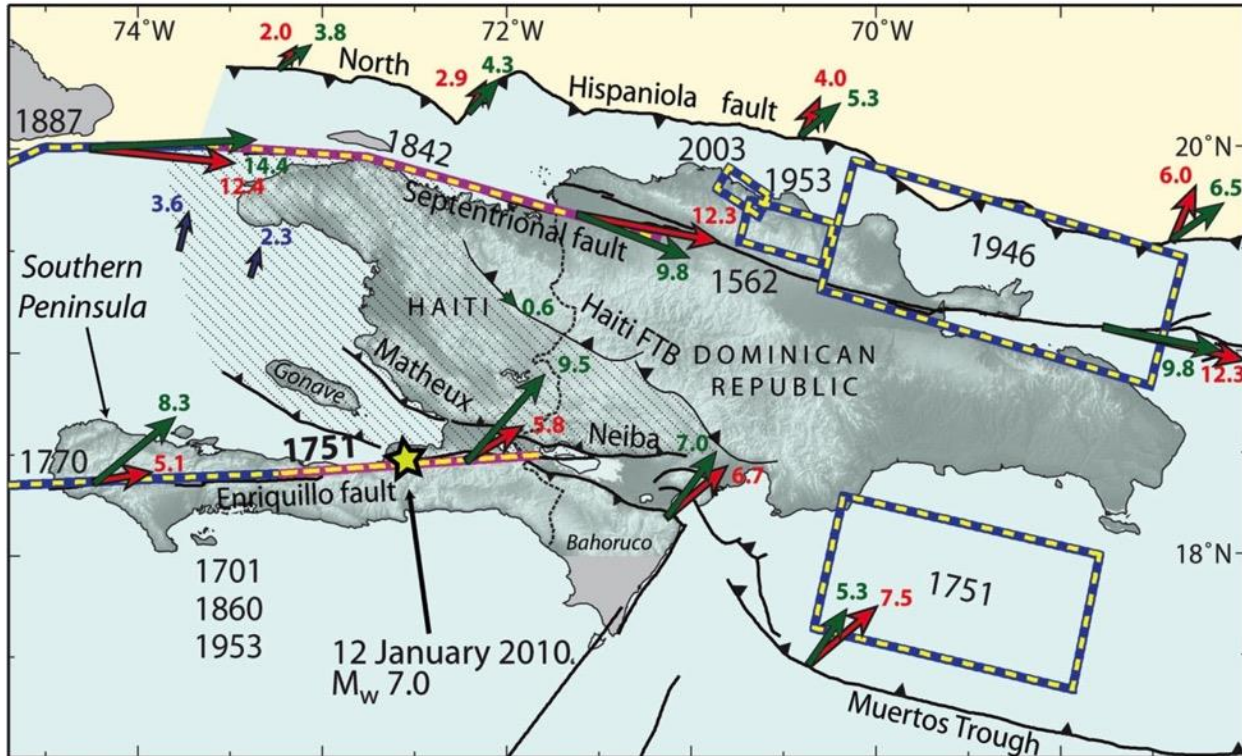


Figure 1: Tectonic context of Hispaniola, including the two major strike-slip faults that compose the broad Caribbean and South American plate boundary: The Enriquillo-Plantain Garden Fault and the Septentrional Fault. Relative plate motion velocity (mm/yr), based on GPS monitoring, is indicated by the arrows; green arrows indicate updated velocities compared to a prior model (in red). Historical earthquakes dates are denoted by black numbers, and their estimated rupture are indicated by either a colored box (dipping thrust fault) or a colored line (vertical strike-slip fault). From Benford et al., 2012.

2.2 Morphological features and classification

Seismic horizons reveal various morphological features that may be indicative of tectonic deformation. These features were analyzed and classified as follows:

Slope break: A position where the slope of the lakebed changes from steeper upslope to less steep downslope (Figure 3). Although such slope breaks are also observed at a paleoshoreline (Sloan et al., 2017; Lucier et al., 2017), we apply this criterion for what may alternatively correspond to an active fault offset below the lakebed, as follows: If the CHIRP profile shows some penetration beneath the lakebed, the imaged stratigraphy is expected to show a similar change in slope for all the layers - something which would not be expected at a paleoshoreline where wave action eroded a scarp in the pre-existing soil/rock.

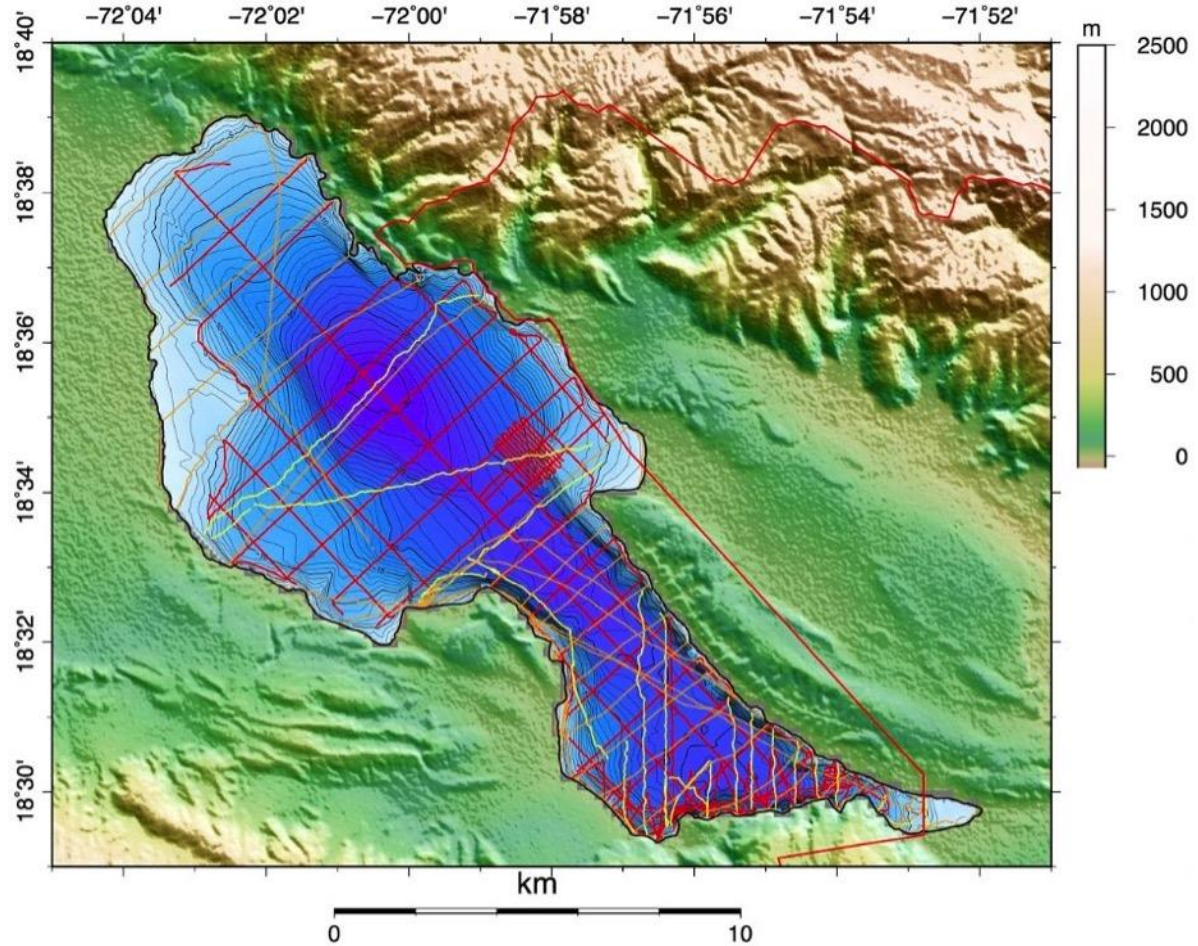


Figure 2: Shuttle Radar Topographic Mission (SRTM) topography of the Lake Azuei region, as derived from the 1 arc-second SRTM data. Artificial sun illumination is from the NE. The survey tracks for the 2017 survey are shown in red, those for the 2013 echosounder survey are shown in orange (Moknatian et al., 2017), and the tracks for the 2013 CHIRP survey are shown in yellow (Wang et al., 2018). The bathymetric data, compiled from all three datasets, are contoured at 1 m interval and labeled every 5 m. Water depths are relative to the lake level in 2017, which was ~5 m higher than the historically stable lake level prior to 2004 (Moknatian et al., 2017).

Base of slope: The position where the lake slope flattens to a nearly horizontal lake floor (Figure 4). We interpret that feature as the transition from lake slope to lake floor, where the lake floor is infilled by a succession of horizontally deposited turbidites that pinch out (“onlap”) onto the lake slope. Recent uplift of the slope or subsidence of the floor may deform the latest turbidite deposit such that it is no longer horizontal.

Fault: In some rare cases, the CHIRP profile reveals a clear stratigraphic offset that extends across all the layers imaged below the lakebed, which may be attributed to an active fault (Figure 5). Such interpretations may be confirmed by examining the corresponding MCS profile, if available.

Syncline Axis: The lowest point (trough) where a series of stacked beds are folded into a synclinal shape (Figure 6).

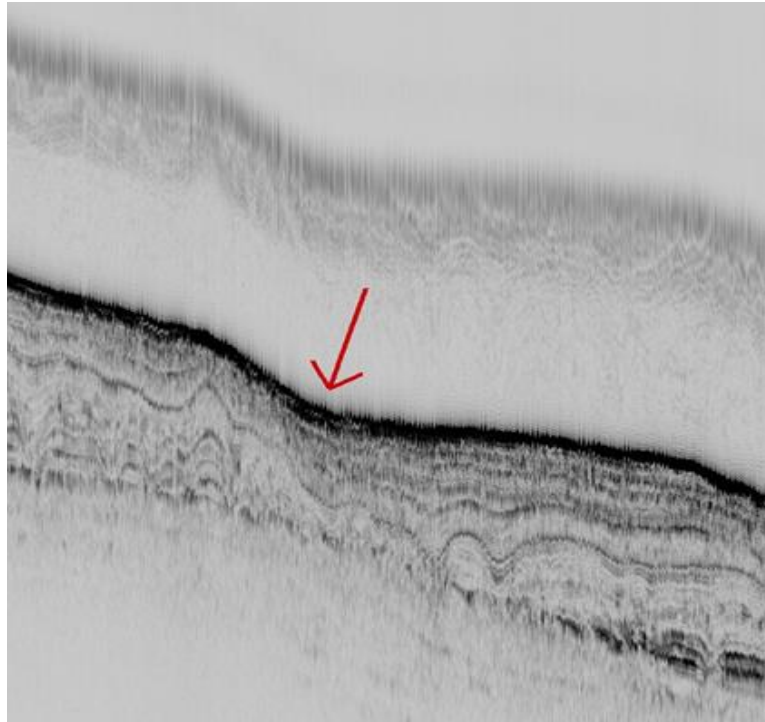


Figure 3: Slope break located at CHIRP profile 402. The vertical and horizontal edges of the image are approximately 15 m and 600 m, respectively.

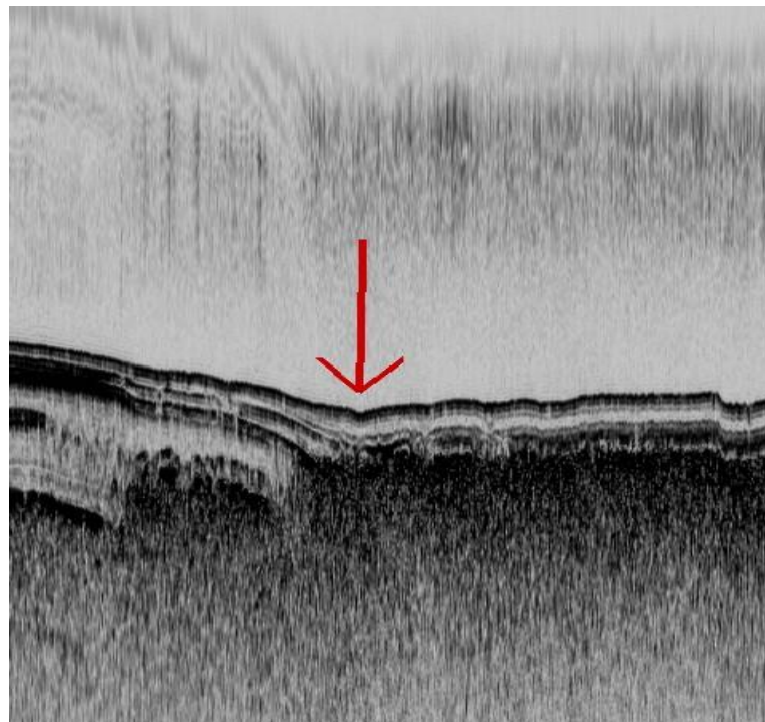


Figure 4: Base of slope located at CHIRP profile 702. The vertical and horizontal edges of the image are approximately 8 m and 380 m, respectively.

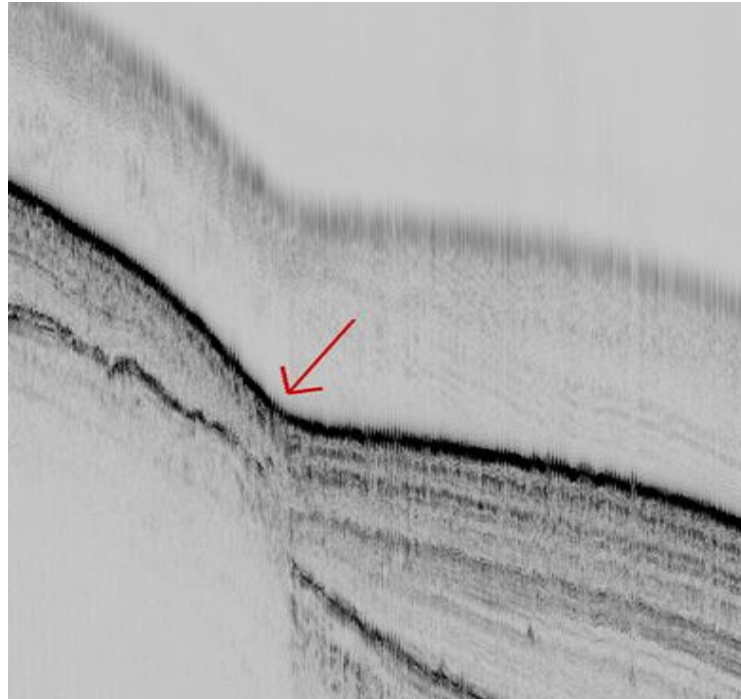


Figure 5: Fault located at CHIRP profile 402. The vertical and horizontal edges of the image are approximately 18 m and 600 m, respectively.

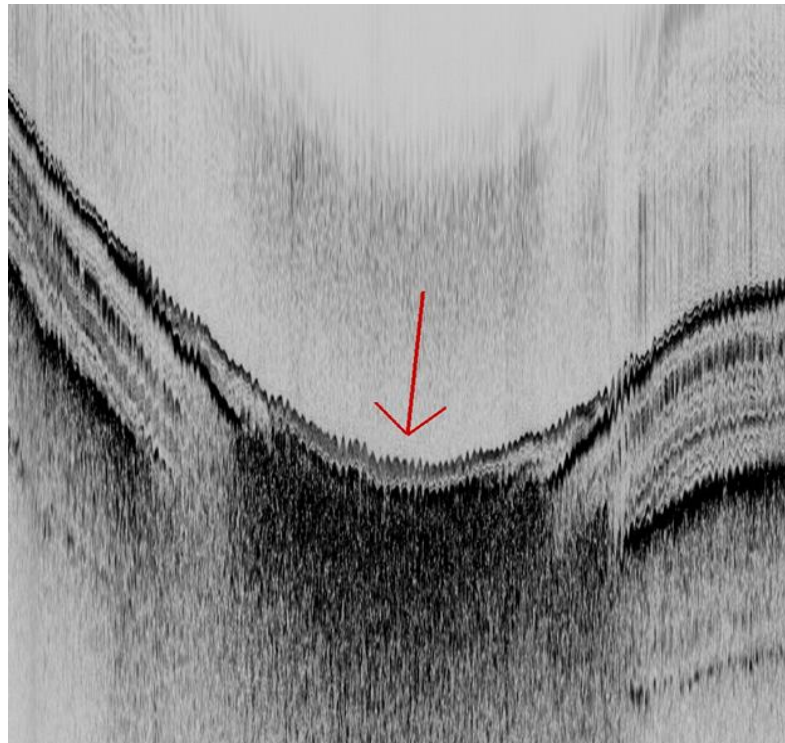


Figure 6: Syncline axis located at CHIRP profile 305. The vertical and horizontal edges of the image are approximately 10 m and 400 m, respectively.

Fold axis: The highest point (crest) where series of stacked beds are folded into an anticlinal shape (Figure 7). Note that if folding were an on-going process, deeper beds should be folded tighter than shallower beds, with the latest flat-lying turbidite pinching out on the flank of the fold.

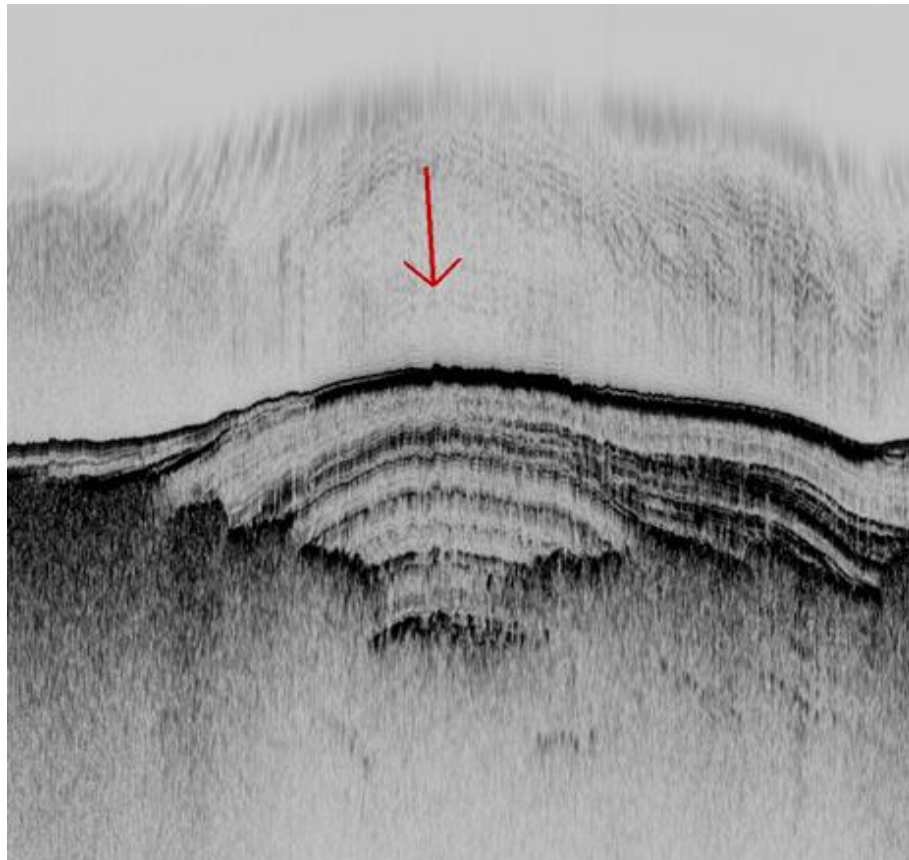


Figure 7: Fold axis located at profile 802001. The vertical and horizontal edges of the image are approximately 17 m and 650 m, respectively.

Soft sediment deformation: Areas where the stratigraphy displays pockmarks or a succession of folds of various amplitudes and shapes (Figure 8). These features may be smoothed over by undeformed sediment. If fluid and/or gas escapes slowly and continuously, localized “pockmarks” are expected. Successive folds (Figure 9) could result from slow downslope creep. Most likely, pervasive soft-sediment deformation (pockmarks and folds) may result from ground liquefaction produced by strong ground motion associated with a sizable earthquake.

3. Results

This section reports preliminary results. Although prior analysis of the CHIRP profiles had already provided some results (Cormier et al., 2017 & 2018; Sloan et al., 2017; Lucier et al., 2017; Murray et al., 2018), this report not only expands on these results but data analysis will continue through the remainder of the year and updated results will be presented at a meeting in Haiti this September 2019 (Cormier et al., 2019) and at the Fall 2019 Meeting of the American Geophysical Union in San Francisco in December 2019 (James et al. 2019).

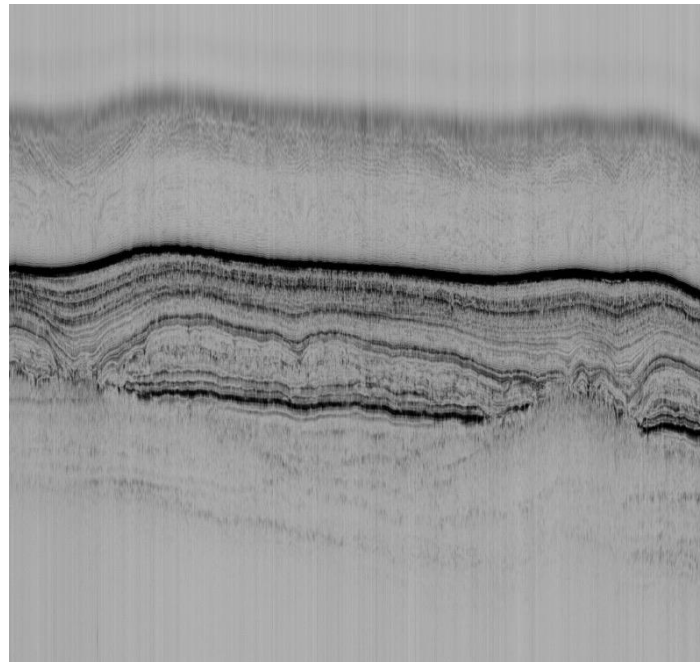


Figure 8: Soft sediment deformation located at CHIRP profile 301. The vertical and horizontal edges of the image are approximately 20 m and 1300 m, respectively.

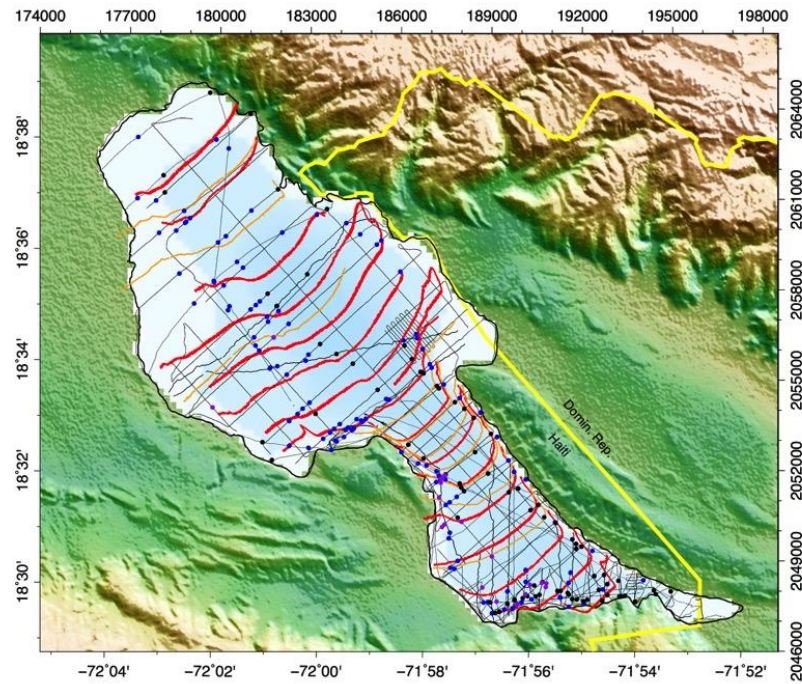


Figure 9: Preliminary picks for some of the morphological features identified from the three sonar datasets. Blue dots indicate slope breaks (presumably indicative of subsurface faults), black dots indicate base of slope (where lake slope transition to flatfish basin), and purple dots are where faults are identified directly from the CHIRP data.

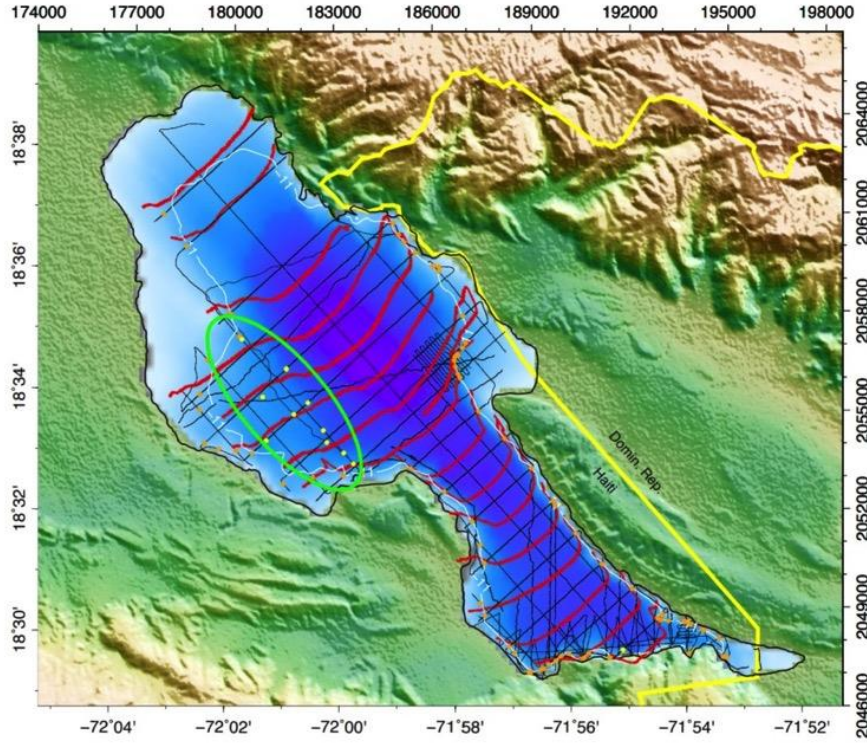


Figure 10: Preliminary map of soft-sediment deformation features imaged with the CHIRP data. Yellow dots mark the extent of soft sediment deformation features, possibly reflecting liquefaction of the lakebed. Orange dots mark the picks for the 11-m deep paleoshoreline (after Lucier, 2017; Sloan et al., 2017). The white line is the 11-m depth contour. Note how the area where the paleoshoreline is uplifted above the 11-m depth also coincides with the presumed area of liquefaction. Both are overlying the broad NW-trending monoclinal fold that occurs in the western region of the lake (Hearn et al., 2018; Charles et al., 2019).

4. Discussion

Multichannel seismic reflection (MCS) data acquired concurrently with CHIRP data in 2017 have revealed two main tectonic structures (Hearn et al., 2017; Charles et al., 2019), and the present analysis allows to better characterize their geometry, as follows:

- 1) MCS data image a NW-trending monoclinal fold on west side of lake. This monocline is interpreted as the surface expression of a SW-dipping blind thrust fault. The MCS data also indicate this monocline is cut across by several near-vertical faults, but their strike is not easily determined from the 1.2 km-spacing of the MCS profiles. Our analysis of slope breaks reveals that these fault strike generally NW, parallel to the strike of the monocline itself (Figure 12).
- 2) MCS profiles reveal a ~3-km wide EW deformation zone along the southern shore of the lake (Figure 11). Because the deformation is barely visible beneath the shallow gas front, it is unclear whether it represent folding, faulting, or a combination of both. Here, our analysis of CHIRP data reveals a set of EW en echelon folds, but because there is no evidence of any subtle fault scarps at the lakebed or in the upper few meters of sediments, we suggest that this deformation zone indicates folding rather than pure strike-slip.

Lastly, CHIRP data reveal zones of soft sediment deformation on the back of the monocline in the western part of lake. We interpret these as resulting from liquefaction. These features also

coincide with the area where the 11-m deep paleoshoreline is uplifted by 1 to 2 m. Both features are compatible with being the result of one or more large earthquake(s) occurring on the presumed SW-dipping blind thrust fault (which would uplift the monocline fold). If this interpretation were correct, it would suggest that this structure is seismically very hazardous.

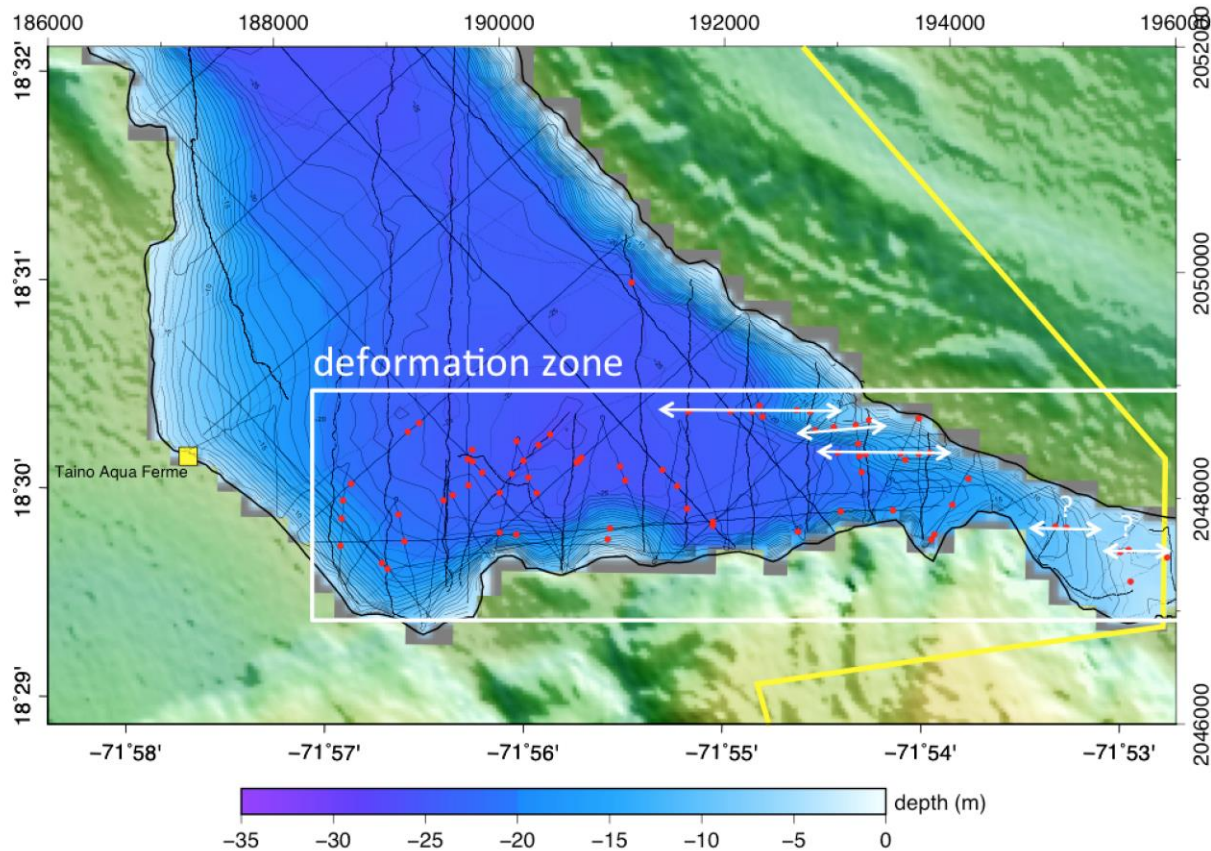


Figure 11: Map of the southern part of the lake, showing our interpretation of a broad deformation zone and several folds. The red dots mark the fold axis interpreted from echosounder profiles and CHIRP profiles. The white rectangle marks the approximate extent of a broad deformation zone, also detected in the deeper penetration MCS profiles (Charles et al., 2019). The double-headed white arrows are the interpreted fold axis. Note how these three folds are arranged in a right-stepping en echelon pattern. Question marks indicate where interpretation is not well supported.

5. Conclusions

- 1) The interpretation and precise co-location of morphological features such as faults, folds, and slope breaks detected from about 400 km of sonar profiles collected in lake Azuei are documenting the spatial relations of these various features.
- 2) It documents the presence of a deformation zone a few km wide, mostly expressed by small folds striking about parallel to the southern shore of the lake. The lack of evidence for any fault scarps at the lakebed in that same area supports a model where transpressional deformation is accommodated by oblique slip on a south-dipping fault bordering the southern lakeshore.
- 3) It also documents that soft-sediment deformation features occur in the western part of the lake in association with a previously documented uplifted paleoshoreline, both of which are

compatible with a large earthquake rupture occurring on a SW-dipping blind thrust fault presumably located beneath these features.

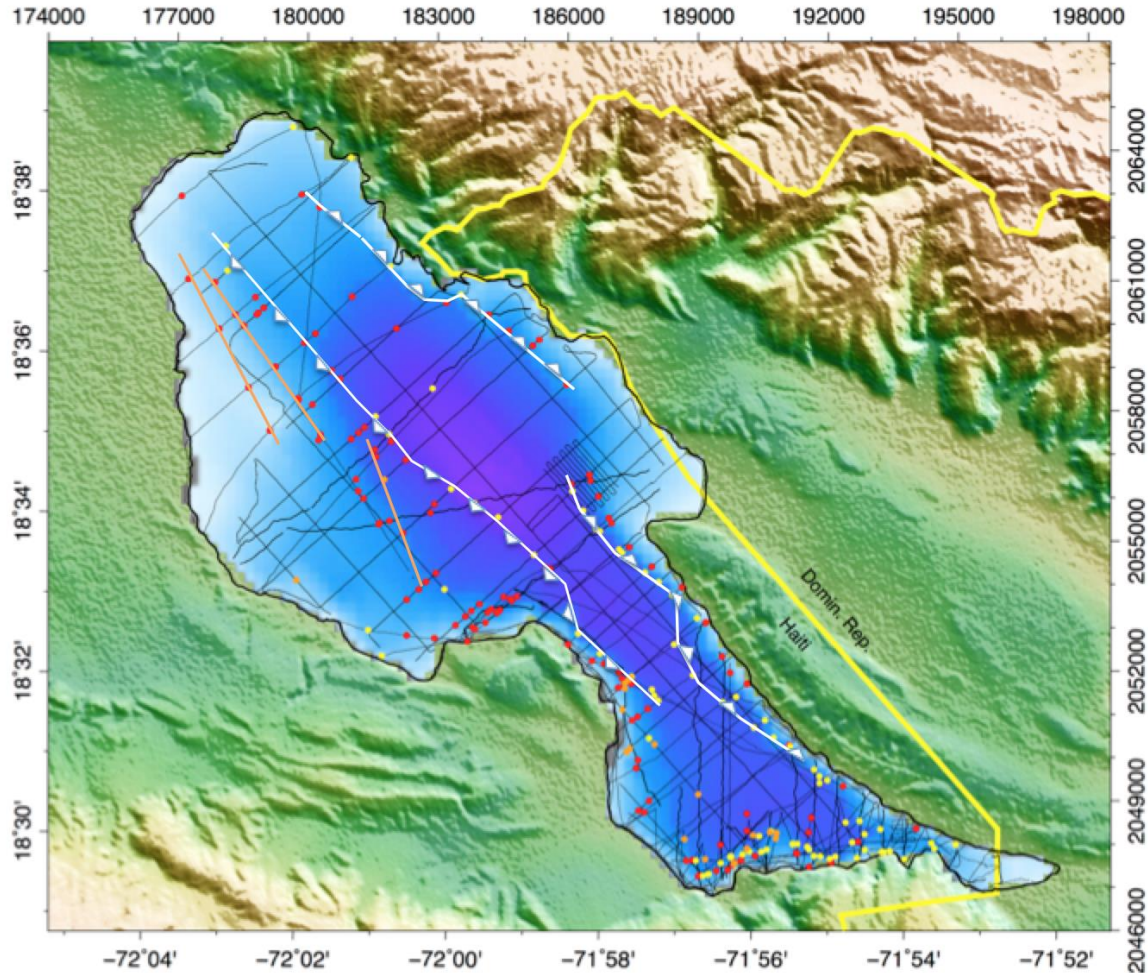


Figure 12: Map showing the picks of the various morphological features as colored dots, along an interpretation of possible fault traces. The red dots are picks for "breaks in slope", the orange dots are picks for "faults", and yellow dots are "base of slope". The white lines with triangles are possible thrust fronts (connecting breaks in slope and base of slope picks). Note the irregular thrust front; this irregularity echoes that of the mountain range on land. The orange lines are other faults, possibly strike-slip. The survey tracks for the 3 sets of sonar profiles are shown as fine black lines

Acknowledgments

This project is financed by the U.S. National Science Foundation under grants EAR-1624583 (URI, M.H. Cormier & J.W King) and EAR-162456 (Lehman College-CUNY, H. Sloan). Kamal James was supported by a Summer Undergraduate Research Fellowship in Oceanography (SURFO) (National Science Foundation REU grant # OCE-1757572). The active participation in this project from several Haitian scientists is gratefully acknowledged, including that of Dominique Boisson, Kelly Guerrier, Roberte Momplaisir, Steeve Symithe, and Sophia Ulysse. The field participation in January 2017 of Nigel Wattrus and Casey Hearn and their technical expertise with data acquisition have been critical to the success of this project.

References

- Benford, B., DeMets, C., and Calais, E., GPS estimates of microplate motions, northern Caribbean: evidence for a Hispaniola microplate and implications for earthquake hazard: *Geophysical Journal International*, 191, 481-490, 2012.
- Calais, E., Freed, A., Mattioli, G., Amelung, F., Jonsson, S., Jansma, P., Hong, S.-H., Dixon, T., Prepetit, C., and Momplaisir, R., Transpressional rupture of an unmapped fault during the 2010 Haiti earthquake: *Nature Geoscience*, 3, 794-799, 2010.
- Charles, N., M.H. Cormier, H. Sloan, N.J. Wattrus, C.C. Sorlien, D. Boisson, K. Guerrier, C.K. Hearn, J.W. King, R. Momplaisir, S.J. Symithe, and S.M.J. Ulysse, Multichannel Seismic Survey of Lake Azuei (Haiti) Documents a Complex System of Active Transpressional Structures Across the North American-Caribbean Plate Boundary, abstract # 555543, *Fall Meeting of the American Geophysical Union*, San Francisco, 9-13 December 2019.
- Cormier, M.H., H. Sloan, and the Lake Azuei Project Team, Lake Azuei Project, Haiti: Field Report, <https://www.projectlakeazuei.org>, January 9 - February 3, 2017.
- Cormier, M.H., Sloan, H., Boisson, D., Brown, B., Guerrier, K., Hearn, C.K., Heil, C.W., Kelly, R.P., King, J.W., Knotts, P., Lucier, O.F., Momplaisir, R., Stempel, R., Symithe, S.J., Ulysse, S.M.J., and Wattrus, N.J., Signature of Transpressional Tectonics in the Holocene Stratigraphy of Lake Azuei, Haiti: Preliminary Results from a High-Resolution Subbottom Profiling Survey, *Fall Meeting of the American Geophysical Union*, Session T047, abstract # 259609, New Orleans, 11-15 December 2017.
- Cormier, M.H., Sloan, H., King, J.W., Boisson, D., Guerrier, K., Hearn, C.K., Heil, C.W., Kelly, R.P., Momplaisir, R., Murray, A.N., Sorlien, C.C., Symithe, S.J., Ulysse, S.M.J., and Wattrus, N.J., Late Quaternary fault-related folding, uplifted paleoshoreline, and liquefaction structures: clues about transpressional activity along the North American-Caribbean plate boundary from a comprehensive seismic reflection survey of Lake Azuei, Haiti, Abstract #368456, *Fall Meeting of the American Geophysical Union*, Washington DC, doi: [10.1002/essoar.10500232.1](https://doi.org/10.1002/essoar.10500232.1), 2018.
- Cormier, M.H., H. Sloan, K. James, D. Boisson, K. Guerrier, C.K. Hearn, J.W. King, R. Momplaisir, T. Ramsamooj, S.J. Symithe, S. Ulysse, and N.J. Wattrus, Déformation Holocène Transpressive Révélée par les Marqueurs Géomorphologiques et Stratigraphiques du Lac Azuei, presented at the *Haiti Géoscience 2019 meeting*, Port-au-Prince, Haiti, 11-13 September 2019.

Hearn, C.K., Cormier, M.H., Sloan, H., Watrus, N., Boisson, D., Brown, B., Guerrier, K., King, J.W., Knotts, P., Momplaisir, R., Sorlien, C.C., Stempel, R., Symithe, S., and Ulysse, S.M.J., Transpressional tectonics across the N. American-Caribbean plate boundary: preliminary results of a multichannel seismic survey of Lake Azuei, Haiti, Abstract T51G-0566, *Fall Meeting of the American Geophysical Union*, New Orleans, 11-15 December 2017.

James, K., M.H. Cormier, H. Sloan, T. Ramsamooj, D. Boisson, K. Guerrier, C.K. Hearn, J.W. King, R. Momplaisir, S.J. Symithe, S.M.J. Ulysse, and N.J. Watrus, Geomorphologic and Stratigraphic Evidence of Ongoing Transpressional Deformation Across Lake Azuei (Haiti), abstract # 554040, *Fall Meeting of the American Geophysical Union*, San Francisco, 9-13 December 2019.

Lucier, O., Submerged Paleo-Shorelines as Markers of Vertical Deformation around Lake Azuei, Haiti, *SURFO Final Report*, 2017.

Mann, P., F.W. Taylor, R.L. Edwards, and T.L. Ku, Actively evolving microplate formation by oblique collision and sideways motion along strike slip faults: An example from the northwestern Caribbean plate margin, *Tectonophysics*, 246, 1–69, 1995.

Moknatian, M., M. Piasecki and J. Gonzalez, Development of geospatial and temporal characteristics for Hispaniola's Lake Azuei and Enriquillo using Landsat imagery, *Remote Sensing*, 9, 510-542, 2017.

Murray, A.N., Sedimentary Signatures of Climate Variability and Tectonic Activity in Lake Azuei, Haiti: Possible Implications for Natural Hazards, *SURFO Final Report*, 2018.

Sloan, H., M.H. Cormier, D. Boisson, B. Brown, K. Guerrier, C.K. Hearn, C.W. Heil, L. Hynes, R.P. Kelly, J.W. King, P. Knotts, O.F. Lucier, R. Momplaisir, R. Stempel, S.J. Symithe, S.M.J. Ulysse, and N.J. Watrus, Subbottom seismic profiling survey of Lake Azuei, Haiti: Seismic signature of paleoshorelines in a transpressional environment and possible tectonic implications, *Fall Meeting of the American Geophysical Union*, Session T047, abstract # 259797, New Orleans, 11-15 December 2017.

Symithe, S., and E. Calais, Present-day shortening in Southern Haiti from GPS measurements and implications for seismic hazard: *Tectonophysics*, 679, 117-124, 2016.

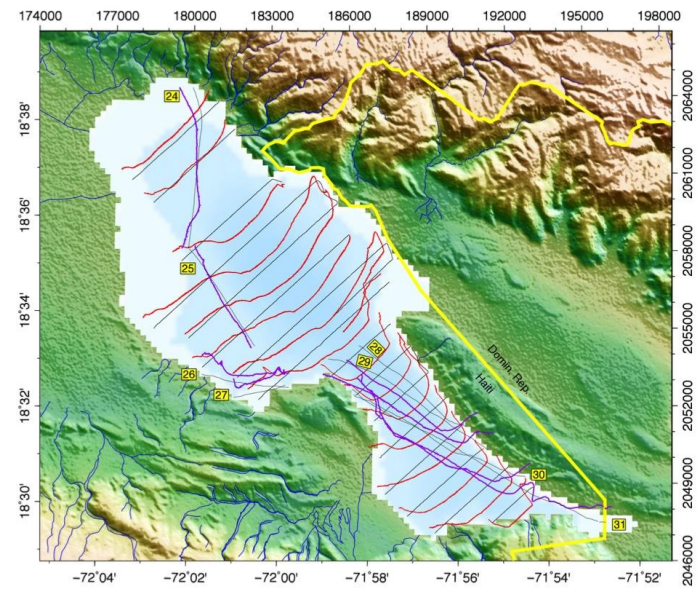
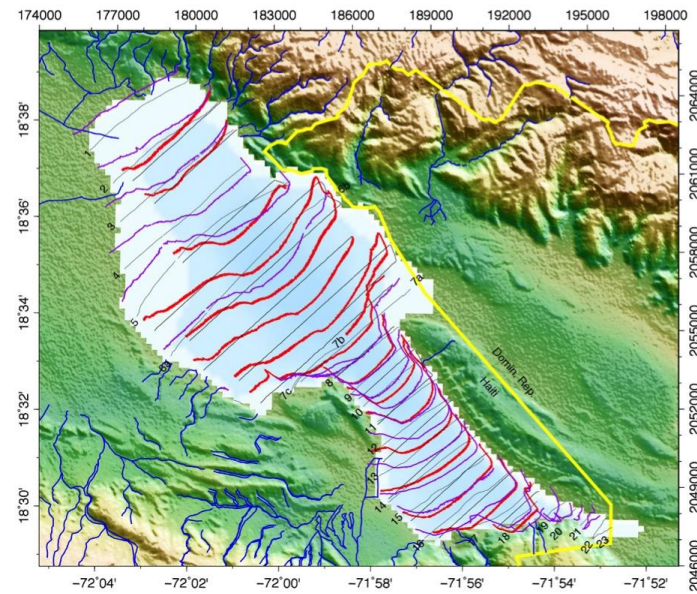
Wang, J., P. Mann, and R.R. Stewart, Late Holocene structural style and seismicity of highly transpressional faults in southern Haiti, *Tectonics* 37, 3834-3852, doi: 10.1029/2017TC004920, 2018.

World Bank, Haiti Earthquake Post Disaster Needs Assessment: Assessment of damage, losses, general and sectoral needs, http://siteresources.worldbank.org/INTLAC/Resources/PDNA_Haiti- 2010_Working_Document_EN.pdf, 2010.

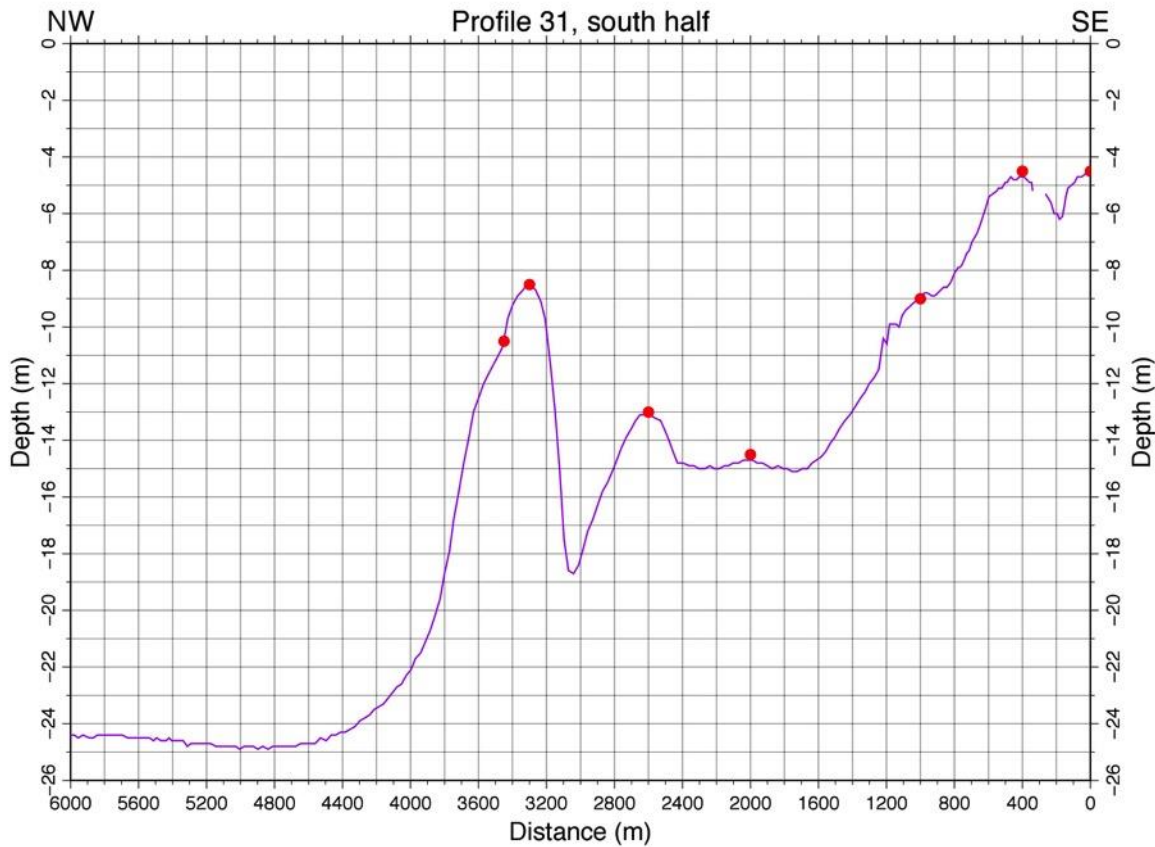
Missing appendices are available by contacting Marie-Hélène Cormier (mhcormier@uri.edu) or Kamal James (kamaljames96@gmail.com).

Appendix 1. Table listing the features picked from the echosounder profiles and displayed as red dots in appendix 3.

Appendix 2. Two maps displaying the location of the echosounder profiles acquired by Prof. Piasecki and his team in 2013 (Moknatian et al., 2017). Profiles are labeled 1 through 31 and are displayed in appendix 3.



Appendix 3. One example among the thirty-one echosounder profiles (located in Appendix 2), displayed as depth versus distance along the profile. Both horizontal and vertical axis are labeled in meters. The red dots indicate interpreted picks for “break in slope”, “base of slope”, and “fold axis” (and listed in Appendix 1).



Appendix 4. Table listing the features picked using OpendTect from the CHIRP profiles acquired in 2013 (Wang et al., 2018) and 2017 (Cormier and Sloan, 2017). X and Y coordinates are in meters, UTM zone 19.

Using stable isotopes to trace marine ecogeochemical cycling in chemosynthetic symbiotic *Solemya velum*

Sommer Meyer^{1,2}, Nina Santos¹, Roxanne Beinart¹, and Kelton McMahon¹

¹Graduate School of Oceanography, University of Rhode Island, Narragansett, Rhode Island, U.S.A.

²Department of Earth & Environmental Sciences, University of Rochester, Rochester, New York, U.S.A.

Corresponding author: Sommer Meyer (smeyer11@u.rochester.edu)

Running head: Isotopes in chemosynthesis and clams

Key Points:

- *Solemya velum* is a bivalve species that has evolved a symbiosis with chemosynthetic bacteria
- *Mercenaria mercenaria* isotopes reflect phytoplankton; *S. velum* isotopes reflect chemosynthetic symbionts
- Compound-specific stable isotope analysis could resolve the hypotheses about the bivalve's organic matter cycling

Key Index Words:

Stable isotopes, chemosynthesis, symbiosis, Solemya velum, ecogeochemical cycling

Abstract

Although symbioses between invertebrates and chemosynthetic bacteria, including the bivalve *Solemya velum* in Rhode Island salt ponds, have been discovered, little is known about the trophic transfer of organic matter in such symbiont-host systems. Nitrogen and carbon stable isotope analysis was completed to reveal how organic matter is transferred from symbiont to host and from host to ecosystem, and how it differs from photosynthetic processes, by creating and tracking an isotopic fingerprint of transferred organic matter. For comparison, samples of *Mercenaria mercenaria* underwent the same treatment, as *M. mercenaria* live in the same Rhode Island salt ponds but consume organic matter through suspension feeding. The mean $\delta^{15}\text{N}$ value of the *S. velum* was $-8.2\text{\textperthousand}$ (± 0.8), whereas the mean *M. mercenaria* value was $10.1\text{\textperthousand}$ (± 0.5). For $\delta^{13}\text{C}$, the mean *S. velum* value was $-32.8\text{\textperthousand}$ (± 0.7) and the mean *M. mercenaria* value was $-18.6\text{\textperthousand}$ (± 0.4). The *M. mercenaria* values within the expected range, given the isotope values of the phytoplankton it feeds on and its trophic position. However, the *S. velum* values were unexpected, and likely due to the isotope values of the chemosynthetic bacteria at the baseline of its food web. These results may provide valuable insight into the ecogeochemical cycling of organic matter originally from chemosynthetic processes, and how it differs from that of photosynthetic processes.

1. Introduction

Throughout the world's oceans, there have been discoveries of symbioses between marine invertebrates and chemosynthetic bacteria, including the bivalve family Solemyidae (Roeselers

& Newton, 2012). Within this family, there are 30 described species, including the *Solemya velum* (Taylor & Glover, 2010). These marine bivalve species host chemosynthetic bacteria, and derive at least part of their food source from feeding off the bacteria. Taking a closer look at *S. velum* and its biogeochemistry may provide a deeper understanding into the process of chemosynthesis, and how food webs throughout the world operate and cycle without the use of photosynthesis for organic matter creation.

The species *S. velum* (see Figure 1b & 1c) is known to reside in the salt ponds of Rhode Island; another, more well-studied species, *Mercenaria mercenaria* (common name quahog; see Figure 1a) lives in the same sediments. Because *M. mercenaria* feed solely through suspension feeding, their food web is based only on photosynthesis. Thus, comparing *S. velum* and *M. mercenaria* may be a useful tactic for differentiating between the ecogegeochemical cycling of food webs based on chemosynthesis and those based on photosynthesis. To do this, samples of *S. velum* and *M. mercenaria* tissues were run through an isotope analysis of $\delta^{15}\text{N}$ and $\delta^{13}\text{C}$ values, which may provide a window into the sources and cycling of organic matter in two bivalve species that are apart of two distinct food webs.



Figure 1. Image of **a)** the bivalve *Mercenaria mercenaria*. **b)** the bivalve *Solemya velum*. **c)** close-up of *S. velum*.

It is likely that these two species will have different nitrogen and carbon isotope ratios, as the source of organic matter in their respective food webs is produced through different processes, which likely leads to separate fractionation values. One hypothesis for differing isotope values is that the two bivalve species feed at different trophic levels. As organic matter transfers through trophic levels, fractionation of certain isotopes occur (DeNiro & Epstein, 1981; Peterson & Fry, 1987; Post, 2002). Therefore, if the two organisms are not feeding at the same trophic level, there may be some isotope fractionation in their tissues. Another hypothesis regards the isotope ratios of each specific food web, tracing down the food web to the autotrophs. Since *S. velum* and *M. mercenaria* are known to feed on autotrophs with different methods of carbon fixation, this hypothesis may be more correct. This study is conducted to test these hypotheses, and to take a closer look at the ecogeochemical cycling of chemosynthesis.

2. Materials and Methods

2.1 Field collections

Field work was completed with the Rhode Island Department of Environmental Management (RI DEM). Quonochontaug Pond and Ninigret Pond, two salt ponds in Rhode Island, were visited for three days over the course of one week in mid-June 2019. Quonochontaug Pond was visited the first two field days, and Ninigret Pond on the last. The RI DEM's collection methods included a bull rake and a large pump to remove the first layers of sediment in a one square-meter quadrant, which then deposited the sediment into a large sifting bin. As this bin was washed out, the individual shellfish could be found, including the targeted bivalve species. Throughout the three days at the salt ponds, many specimens of *M. mercenaria* were found, both from the bull rake and the pump, however there were no *S. velum* to be seen.

Because this field work did not produce any *Solemya* samples, additional field work was completed the following week, without RI DEM's participation. Several people from the University of Rhode Island Graduate School of Oceanography labs traveled to another salt pond, Point Judith (see Figure 2). Collection methods in Point Judith consisted of bull rakes as well as large garden shovels with sieves. *M. mercenaria* were primarily collected with the bull rakes, and *S. velum* were targeted by removing sediment with the large garden shovels and sieving through it. After completing two days of field work at Point Judith Pond, 23 specimens of *M. mercenaria* and 74 specimens of *S. velum* were collected. All samples were frozen from the time of collection until later dissections could take place.

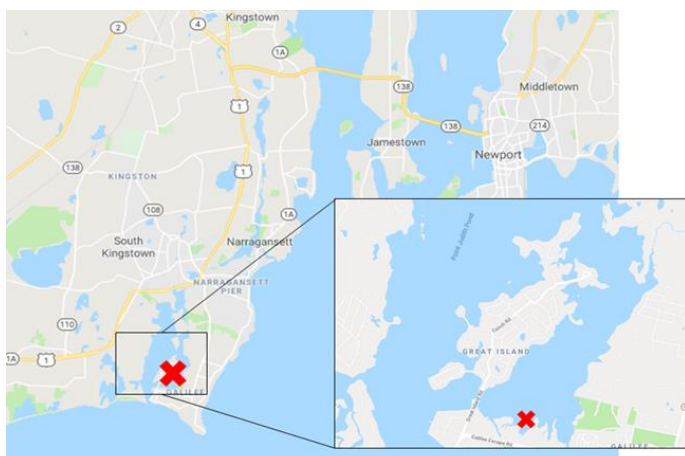


Figure 2. The location in which bivalve samples were collected in reference to Rhode Island and (in box) Point Judith Pond.

2.2 Sample processing

Once a sufficient number of *S. velum* and *M. mercenaria* samples were obtained, the tissues of interest were separated through dissection. The targeted tissues included the gills and the foot muscle in each specimen of *S. velum* and *M. mercenaria*. The shells of each bivalve were also kept, so that the periostracum, a thin layer of organic matter on the outside of the calcium carbonate shell, could also be put through isotope analysis.

As the *S. velum* are not widely studied, a new protocol for the dissections had to be created. A similar protocol was also created for the *M. mercenaria*, so that the two species would have as similar a treatment as possible. For both species, after the specimen has been sufficiently thawed, the adductor muscles were cut along the opening of the shell with forceps, and the shell was then pried open. With tweezers, the gills were identified, separated, and stored in a vial; the same was done for the foot muscles. After these two tissues were separated, the rest of the bivalve interior was pulled out and discarded, and the shell was cleaned and likewise stored. All samples of foot, gill, and shell were frozen at -20 °C until the preparation for isotope analysis.

The shells of each dissected specimen are to be analyzed at a future date. The processing for this analysis will first be to homogenize the shells. This will be done by breaking the shell and grinding them into a homogenous powder in a mortar and pestle. Next, the calcium carbonate of the shell will be removed by reacting the sample with hydrochloric acid. This will leave behind only the organic material of the periostracum, which will then be analyzed on an isotope ratio mass spectrometer, similar to how the rest of the samples were run.

2.3 Isotope analysis

To prepare the samples of dissected foot and gill tissues for isotope analysis, several steps had to be completed. First, the samples were dehydrated in a freeze-dryer for approximately 48 hours. To ensure proper freeze-drying, the samples needed to remain frozen until immediately set in the freeze dryer. Next, the samples were left to sit for a few days, so that they could acclimate to the ambient moisture in the air. This ensures that during preparation and analysis, the samples do not change in mass from absorption or evaporation of water from the tissues.

Although there were 74 specimens collected of the *S. velum*, only 19 of these samples were run through isotope analysis. This is because after all the samples were freeze-dried and acclimated to ambient humidity, preliminary weighing of all the *S. velum* tissues took place. The specimens were then separated into two categories – samples where the foot and gill tissues were over 5 mg each, and those that were not. The specimens with adequate mass, that is, samples with over 5 mg each of foot and gill, were selected for isotope analysis. For *M. mercenaria* samples, the largest 19 of the 23 specimens were selected for consistency.

The selected samples were homogenized. *M. mercenaria* were homogenized by transferring the sample to a mortar and pestle, grinding it until it was homogenous, and transferring it back into the sample vial from which it came. The *S. velum* samples, however, were much smaller, and transferring it to and from the mortar would risk losing a large portion of that sample. Instead, the *S. velum* were kept in their original vials, and a spatula was used to grind the samples into a homogenous powder in their vials.

Next, the samples were weighed out into cylindrical tin capsules that would then be placed in the mass spectrometer. Each tin capsule was tared to zero. Approximately 1 mg (± 0.1 mg) of

homogenized sample was placed into the tin capsule, and the tin capsule was folded shut. The tin capsules were placed into a labeled container, with each spot corresponding to a specific specimen and tissue sample. Once each of the 76 samples to be run (19 *S. velum* gills, 19 *S. velum* feet, 19 *M. mercenaria* gills, and 19 *M. mercenaria* feet) were placed into a tin capsule, they were ready for isotope analysis.

The labeled container with the samples was brought to the US Environmental Protection Agency's Atlantic Ecology Division Laboratory (henceforth referred to simply as the EPA), who had agreed to assist in this process by allowing these samples to be run on their Elementar IsoPrime elemental analysis isotope ratio mass spectrometer (EA/IRMS). At the EPA, standard samples of known isotopic composition were weighed out. This included 5 samples of cysteine with weights between 1.0 mg and 2.5 mg, and 8 samples of blue mussel laboratory standard (BLUM) with weights of 2 mg (± 0.2 mg).

The standards and bivalve samples were then placed in the EA/IRMS. First, a blank sample of an empty tin capsule was placed. Then, all 5 cysteine standards followed by 2 BLUM. Next, 24 samples were placed, then 2 BLUM, then another 24 samples, then 2 more BLUM. Finally, the last 28 bivalve samples were placed, followed by the last 2 BLUM. The information of each sample was entered into the EA/IRMS program, the EA/IRMS was calibrated, and the analysis began.

Once the raw data came from the isotope analysis, it had to be corrected to remove any instrument error. This was completed by finding the difference between the BLUM true value and the mean BLUM measured value and subtracting this difference from each sample. For the $\delta^{15}\text{N}$, the offset correction was $-0.66\text{\textperthousand}$, and for the $\delta^{13}\text{C}$, the offset correction was $-0.55\text{\textperthousand}$. The data were plotted and analyzed, and isotope values were compared between the two species and between the two tissues of each species using Student t-tests with a significance point set at $p < 0.05$.

3. Results

M. mercenaria and *S. velum* had greatly different $\delta^{15}\text{N}$ values (Student t-test, $p = 1.96 \times 10^{-87}$) and $\delta^{13}\text{C}$ values (Student t-test, $p = 1.08 \times 10^{-82}$). Although each sample within the distinct species were relatively similar to each other, the two species had vastly different isotopic signatures (see Figure 3a). The difference in the mean $\delta^{15}\text{N}$ values for *S. velum* and *M. mercenaria* was $18.3\text{\textperthousand}$; for $\delta^{13}\text{C}$ the difference in mean values was $14.2\text{\textperthousand}$.

Table 1. Mean isotope values for all *Mercenaria mercenaria* samples, *M. mercenaria* foot samples, and *M. mercenaria* gill samples. Reports nitrogen-15 and carbon-13 values, as well as a standard deviation (SD) for each ($n = 19$).

	$\delta^{15}\text{N} (\text{\textperthousand})$	SD $\delta^{15}\text{N}$	$\delta^{13}\text{C} (\text{\textperthousand})$	SD $\delta^{13}\text{C}$
<i>Mercenaria mercenaria</i> all	10.1	0.5	-18.6	0.4
<i>Mercenaria mercenaria</i> foot	10.0	0.5	-18.3	0.3
<i>Mercenaria mercenaria</i> gill	10.2	0.4	-18.8	0.3

M. mercenaria samples had a mean $\delta^{15}\text{N}$ value of 10.1‰ (± 0.5) and a mean $\delta^{13}\text{C}$ value of -18.6‰ (± 0.4); the *M. mercenaria* foot and gill samples were not statistically different in $\delta^{15}\text{N}$ values (Student t-test, $p = 0.25$) or $\delta^{13}\text{C}$ values (Student t-test, $p = 0.78$) (Table 1 & Figure 3b). The mean $\delta^{15}\text{N}$ value for *S. velum* was -8.2‰ (± 0.8) and the $\delta^{13}\text{C}$ was -32.8‰ (± 0.7). The gills were significantly isotopically lighter in both $\delta^{15}\text{N}$ values (Student t-test, $p = 5.82 \times 10^{-4}$) and $\delta^{13}\text{C}$ values (Student t-test, $p = 2.17 \times 10^{-6}$) (Figure 3c).

Table 2. Mean isotope values for all *Solemya velum* samples, *S. velum* foot samples, and *S. velum* gill samples. Reports nitrogen-15 and carbon-13 values, as well as a standard deviation for each ($n = 19$).

	$\delta^{15}\text{N}$ (‰)	SD $\delta^{15}\text{N}$	$\delta^{13}\text{C}$ (‰)	SD $\delta^{13}\text{C}$
<i>Solemya velum</i> all	-8.2	0.8	-32.8	0.7
<i>Solemya velum</i> foot	-7.8	0.7	-32.3	0.5
<i>Solemya velum</i> gill	-8.7	0.7	-33.3	0.6

4. Discussion

The goal of this project was to investigate any potential major differences in the isotopes of the bivalves *S. velum* and *M. mercenaria*, as they feed off different organisms and in different ways. These results may provide valuable insight into the ecogeochimical cycling within the *M. mercenaria* and the *S. velum*. The isotope values of *M. mercenaria* were within the expected range for a coastal marine suspension feeder. However, the *S. velum* isotope values were unpredicted; this could be explained with multiple different hypotheses. First, the *S. velum* could be feeding at a different trophic level; however, the major differences in isotope values between *S. velum* and other marine bivalves would be difficult to explain with only this hypothesis. Another possible hypothesis, and one that is more evident, is that the *S. velum*'s unique method of feeding on chemosynthetic bacteria symbionts could have a large impact on the baseline isotope signature of the *S. velum*'s food web.

The nitrogen isotope values for *M. mercenaria* fall within the expected range for this type of organism. Atmospheric nitrogen has a $\delta^{15}\text{N}$ value of approximately 0‰ (Peterson & Fry, 1987), and fractionation from nitrogen uptake typically leave marine phytoplankton with $\delta^{15}\text{N}$ values in the range of 2.2‰ to 6.2‰ (Needoba, Waser, Harrison, & Calvert, 2003). Many trophic isotope studies have shown that the nitrogen fractionation during a trophic transfer leaves the $\delta^{15}\text{N}$ of the consumer on average 3-4‰ heavier than that of its diet (DeNiro & Epstein, 1981; Peterson & Fry, 1987; Post, 2002). Thus, the *M. mercenaria* $\delta^{15}\text{N}$ value of 10.1‰ (± 0.5) could easily place the species at the second or third trophic position. Because *M. mercenaria* feed on phytoplankton and zooplankton through suspension feeding, this trophic position would be expected.

The *M. mercenaria* carbon isotope values can also be easily explained. Rounick & Winterbourne (1986) show that marine phytoplankton $\delta^{13}\text{C}$ typically range from -23.8‰ to -19.3‰. Carbon typically exhibits low trophic fractionation; it is estimated to be between 0‰ and 1‰ (Peterson & Fry, 1987), with a mean of 0.4‰ (Post, 2002). The $\delta^{13}\text{C}$ value for *M.*

mercenaria of -18.6‰ (± 0.4) falls directly within the range for a consumer at the second to third trophic position, again showing isotope values that are to be expected.

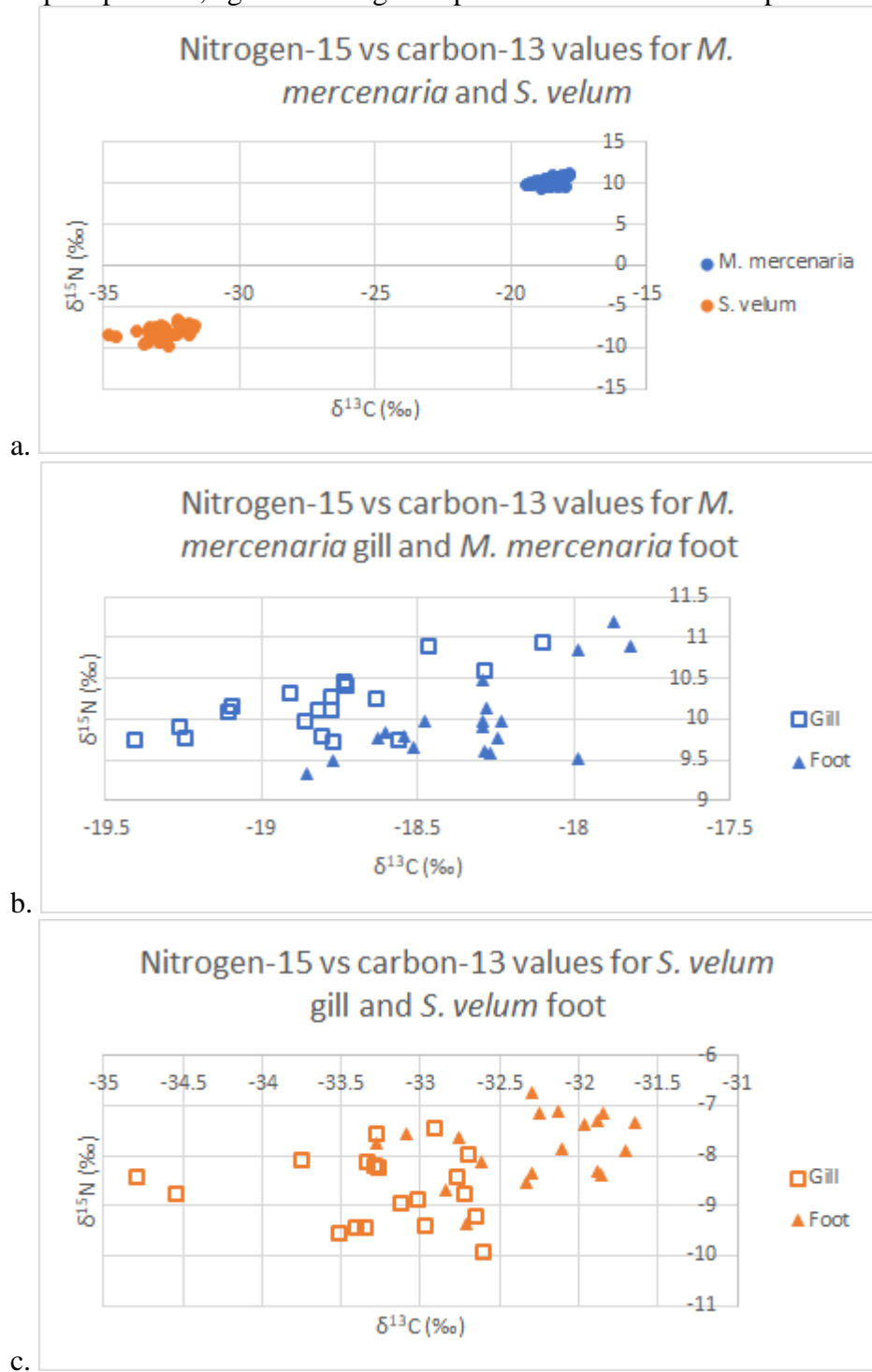


Figure 3. Dual-isotope plot of nitrogen-15 vs carbon-13 for **a**) all samples of *Mercenaria mercenaria* and *Solemya velum*; foot and gill tissues reported together. **b**) all samples of *M. mercenaria*; foot and gill reported separately. **c**) all samples of *S. velum*; foot and gill reported separately.

The $\delta^{15}\text{N}$ and $\delta^{13}\text{C}$ values of the *M. mercenaria* from Point Judith Pond were compared to those from O'Donnell et al (2003) and Kanaya et al (2013). The values from the three areas are all similar, however they do not fall within one standard deviation of each other (see Table 3). This is perhaps due to *M. mercenaria* relying strictly on suspension feeding, and thus the isotope signatures would be more susceptible to changes in baseline isotope values of phytoplankton in different regions.

The isotope values of *Solemya velum*, however, are much different from that of the *Mercenaria mercenaria*. The $\delta^{15}\text{N}$ value of $-8.2\text{\textperthousand}$ (± 0.8) is actually lighter than that of atmospheric nitrogen ($\delta^{15}\text{N} = 0\text{\textperthousand}$; Peterson & Fry, 1987), the opposite of marine photosynthetic organisms and their consumers. Additionally, the *S. velum* $\delta^{13}\text{C}$ value of $-32.8\text{\textperthousand}$ (± 0.7) is approximately $10\text{\textperthousand}$ lighter than marine phytoplankton. These values may seem enigmatic without further studies, however there are still possible explanations for the distinct isotopic signature of *S. velum*.

One hypothesis for the distinctive *S. velum* isotope values is that *S. velum* is feeding at a different trophic level than *M. mercenaria*. Because of nitrogen isotope fractionation at trophic transfers, organisms at higher trophic levels have different isotope values than organisms feeding at lower trophic levels (Cabana & Rasmussen, 1996). However, upon inspection of the data, this hypothesis does not seem likely to be the main cause of the distinct *S. velum* isotope values. Both *S. velum* and *M. mercenaria* are known to feed on autotrophs, and thus a trophic position variability higher than one trophic level would be inconsistent with the known information regarding these two species. As trophic fractionation is typically around $3-4\text{\textperthousand}$ for $\delta^{15}\text{N}$ (DeNiro & Epstein, 1981; Peterson & Fry, 1987; Post 2002) and only $0-1\text{\textperthousand}$ for $\delta^{13}\text{C}$ (Post, 2002), the differences in $\delta^{15}\text{N}$ values ($18.3\text{\textperthousand}$) and $\delta^{13}\text{C}$ values ($14.2\text{\textperthousand}$) could not be explained with only trophic position variability.

Another hypothesis for the *S. velum* results is that *S. velum* is a part of a unique food web, and that this food web possesses different isotope values at its baseline. The baseline of a food web, that is, the autotrophs at the bottom of the chain, can harbor different isotope values from autotrophs in other food webs, and this difference can be carried up through the consumers of the baseline (Vander Zanden & Rasmussen, 1999). Because *S. velum* harborsymbiotic chemosynthetic bacteria, they get at least a large portion of their diet by feeding off these bacteria (Stewart & Cavanaugh, 2006). These chemosynthetic bacteria have the ability to fix inorganic carbon by methods quite unlike that of photosynthetic organisms, and therefore have the potential for radically different isotope fractionation. If the chemosynthetic bacteria do indeed create a much different baseline from that of marine phytoplankton, *S. velum* as the consumer would have this difference reflected in its own tissues.

It is important to note with this hypothesis that *S. velum* gets at least a majority of its food from the chemosynthetic bacteria, and it has a greatly reduced gut, which in turn reduces the ability to suspension feed (Stewart & Cavanaugh, 2006). However, there is still the possibility that *S. velum* suspension feeds on phytoplankton for a small portion of its diet (Krueger, Gallager, & Cavanaugh, 1992). Therefore, there is a possibility that the isotope values of the *S. velum* tissues are actually the weighted average of two different baselines - the chemosynthetic bacteria and phytoplankton.

These results appear to be consistent with other studies documenting isotope values in *S. velum*. Conway, Capuzzo, & Fry (1989) measured isotope values of *S. velum* in two areas of

Cape Cod, Massachusetts - Little Buttermilk Bay and Hadley's Harbor. The $\delta^{15}\text{N}$ and $\delta^{13}\text{C}$ values of the *S. velum* in Little Buttermilk Bay are easily within the range of the values reported from Point Judith Pond. In Hadley's Harbor, however, the $\delta^{13}\text{C}$ value is slightly heavier, thoughnot unreasonably different, but the $\delta^{15}\text{N}$ value was a striking $-0.6\text{\textperthousand}$ (± 3.5) (Table 3). Looking at the similarities between Point Judith Pond and Little Buttermilk Bay, and the relatively high standard deviation at Hadley's Harbor, it seems as though *S. velum* may be living in different conditions or feeding on different baselines. A potential explanation for this may be related to unique biogeochemistry in the region that the *S. velum* were collected.

Table 3. Comparative values of nitrogen-15 and carbon-13 isotope ratio values in *Solemya velum* and *Mercenaria mercenaria* from several studies.

Species	Location	$\delta^{15}\text{N} (\text{\textperthousand})$	$\delta^{13}\text{C} (\text{\textperthousand})$	Reference
<i>Solemya velum</i>	Point Judith Pond, RI	-8.2 (± 0.8)	-32.8 (± 0.7)	This study
<i>Solemya velum</i>	Little Buttermilk Bay, Cape Cod, MA	-8.7 (± 0.8)	-32.7 (± 1.0)	Conway et al, 1989
<i>Solemya velum</i>	Hadley's Harbor, Cape Cod, MA	-0.6 (± 3.5)	-31.8 (± 0.9)	Conway et al, 1989
<i>Mercenaria mercenaria</i>	Point Judith Pond, RI	10.1 (± 0.5)	-18.6 (± 0.4)	This study
<i>Mercenaria mercenaria</i>	Assateague Channel, VA	11.2 (± 0.3)	-17.3 (± 0.1)	O'Donnell et al, 2003
<i>Mercenaria mercenaria</i>	Oi Tidal Flat, Inner Tokyo Bay	7.4 (± 0.8)	-19.2 (± 0.2)	Kanaya et al, 2013

One last important feature to note is the relation of the isotope values in the bivalve foot and gill tissues. The close values suggest that the isotope fractionation between the bivalve and its diet has been cycled throughout the entire bivalve tissue. In *M. mercenaria*, the foot and gill isotope values were not statistically different; running a Student t-test gives a $p = 0.25$ for nitrogen values and a $p = 0.78$ for carbon values, indicating that the isotope values are consistent throughout its tissue. However, there are statistical differences in the tissue isotopes of *S. velum*; the gill appear to be lighter than the foot in both $\delta^{15}\text{N}$ and $\delta^{13}\text{C}$ values. Running a Student t-test confirms this; the nitrogen value had a $p = 5.82 \times 10^{-4}$ and the carbon value had a $p = 2.17 \times 10^{-6}$. As the chemosynthetic bacteria are hosted inside the *S. velum*'s gill (Stewart & Cavanaugh, 2006), it is interesting to note that the gill isotope values are statistically different from the foot values in *S. velum* but not *M. mercenaria*. This could point towards the mechanisms of organic matter cycling in these bivalves, however further studies would be required to fully analyze this feature.

5. Conclusion

These results lend themselves well to application of future studies; for example, compound-specific isotope analysis may provide an even more in-depth analysis by targeting the isotope values of specific amino acids to separate baseline variability from trophic fractionation. Additionally, isotope analysis on more chemosynthetic organisms or their consumers may give a better understanding of the cycling throughout ecosystems.

Acknowledgements

Sommer Meyer was supported by a Summer Undergraduate Research Fellowship in Oceanography (SURFO) (National Science Foundation REU grant # OCE- 1757572). We would like to thank Katherine Rodrigue and the Rhode Island Department of Environmental Management for assistance with field work, along with Rick McKinney and the US Environmental Protection Agency's Atlantic Ecology Division Laboratory for assistance with running the isotope analysis samples. We would also like to thank Angela Stahl, Catherine Nowakowski, Chris Mayer, and Michelle Hauer for their unparalleled support and guidance throughout this project. Lastly, we would like to thank Dr. Lucie Maranda and Dr. David Smith, without whom our participation in the SURFO program would not have been possible.

References

- Cabana, G. & Rasmussen, J. B. (1996). Comparison of aquatic food chains using nitrogen isotopes. *Proceedings of the National Academy of Sciences of the United States of America*, 93(20), 10844-10847. doi:10.1073/pnas.93.20.10844
- Conway, N., Capuzzo, J. M., & Fry, B. (1989). The role of endosymbiotic bacteria in the nutrition of *Solemya velum*: Evidence from a stable isotope analysis of endosymbionts and host. *Limnology and Oceanography*, 34(1), 249-255. doi:10.4319/lo.1989.34.1.0249
- DeNiro, M. J. & Epstein, S. (1981). Influence of diet of the distribution of nitrogen isotopes in animals. *Geochimica et Cosmochimica Acta*, 45(3), 341-351. doi:10.1016/0016-7037(81)90244-1
- Kanaya, G. et al. (2013). Temporal changes in carbon and nitrogen stable isotope ratios of macrozoobenthos on an artificial tidal flat facing a hypertrophic canal, inner Tokyo Bay. *Marine Pollution Bulletin*, 71(1-2), 179-189. doi:10.1016/j.marpolbul.2013.03.018
- Krueger, D. M., Gallager, S. M., & Cavanaugh, C. M. (1992). Suspension feeding on phytoplankton by *Solemya velum*, a symbiont-containing clam. *Marine Ecology Progress Series*, 86, 145-151. doi:10.3354/meps086145
- Needoba, J. A., Waser, N. A., Harrison, J. P., & Calvert, S. E. (2003). Nitrogen isotope fractionation in 12 species of marine phytoplankton during growth on nitrate. *Marine Ecology Progress Series*, 255, 81-91. doi:10.3354/meps255081
- O'Donnell, T. H., Macko, S. A., Chou, J., Davis-Hartten, K. L., Wehmiller, J. F. (2003). Analysis of $\delta^{13}\text{C}$, $\delta^{15}\text{N}$, and $\delta^{34}\text{S}$ in organic matter from the biominerals of modern and fossil *Mercenaria* spp. *Organic Geochemistry*, 34(2), 165-183. doi:10.1016/S0146-6380(02)00160-2
- Peterson, B. J. & Fry, B. (1987). Stable isotopes in ecosystem studies. *Annual Review of Ecology and Systematics*, 18, 293-320. doi:10.1146/annurev.es.18.110187.001453

- Post, D. M. (2002). Using stable isotopes to estimate trophic position: models, methods, and assumptions. *Ecology*, 83(3), 703-718. doi:10.1890/0012-9658(2002)083[0703:USITET]2.0.CO;2
- Roeselers, G. & Newton, I. L. G. (2012). On the evolutionary ecology of symbioses between chemosynthetic bacteria and bivalves. *Applied Microbiology and Biotechnology*, 94(1), 1-10. doi:10.1007/s00253-011-3819-9
- Rounick, J. S. & Winterbourne, M. J. (1986). Stable carbon isotopes and carbon flow in ecosystems. *BioScience*, 36(3), 171-177. doi:10.2307/1310304
- Stewart, F. J. & Cavanaugh, C. M. (2006). Bacterial endosymbioses in *Solemya* (Mollusca: Bivalvia) - Model systems for studies of symbiont-host adaptation. *Antonie van Leeuwenhoek*, 90(4), 343-360. doi:10.1007/s10482-006-9086-6
- Taylor, J. D. & Glover, E. A. Chemosynthetic bivalves. *Topics in Geobiology*, 33, 107-135. doi:10.1007/978-90-481-9572-5_5
- Vander Zanden, M. J. & Rasmussen, J. B. (1999). Primary consumer $\delta^{13}\text{C}$ and $\delta^{15}\text{N}$ and the trophic position of aquatic consumers. *Ecology*, 80(4), 1395-1404. doi:10.1890/0012-9658(1999)080[1395:PCCANA]2.0.CO;2

Examining How Primary Productivity Shifts Over A Summer Season in Narragansett Bay

Lydia Nunez^{1,2}, Diana Fontaine¹, Samantha Setta¹, and Tatiana Rynearson¹

¹University of Rhode Island Graduate School of Oceanography, Narragansett RI

²University Ana G. Mendez, Puerto Rico

Abstract

Phytoplankton are microscopic organisms capable of photosynthesis in oceans, seas, and freshwater, and are an essential component of aquatic ecosystems. Primary productivity (PP) is the rate at which phytoplankton control carbon dioxide and oxygen levels in the Earth's atmosphere, through photosynthesis. Changes in light, carbon dioxide, nutrients, and temperature influence the variety of phytoplankton, their growth rates, and biomass accumulation. In areas where there are less nutrients, nitrogen gas (N_2) fixation plays an important role in supporting oceanic primary production. Phytoplankton size can be affected by the amount of nutrients, therefore if there are less nutrients, it is expected that phytoplankton are smaller. The main goal of this research was to examine how PP varies with changing summer conditions in Narragansett Bay (NB). Weekly surface, mid-depth and bottom samples were collected and this sampling effort was paired with the long-term plankton time series in Narragansett Bay. PP was measured with ^{13}C incubations at in situ light levels. The stable isotope, carbon-13 was used to determine the photosynthetic rate. To obtain size-fractionated PP rates, in-line filtering was done using 5- and 20- μm filters for biomass collection on GF/F filters and these PP rates were paired with size-fractionated chlorophyll-a. Cell counts were measured using flow cytometry. As a result, NB demonstrated to be at its highest temperatures, but this alone is not an indicator of changes in this estuary. Therefore, the photosynthetic rate was also taken into consideration, where it showed that the smallest phytoplankton (0.7-5 μm) were acquiring more carbon uptake over time. Besides, the community composition was observed using the Guava Flow Cytometry where there might be a small pattern occurring, because the small-size population was dominant but with time, the medium population of phytoplankton became more dominant. These data demonstrated how summer primary production changes with shifts in environmental conditions in a temperate estuary.

(THE REST OF THIS SECTION IS INTENTIONALLY LEFT BLANK)

Testing Nanographene as a Passive Sampler for Emerging Contaminants of Environmental Concern in Narragansett Bay

Jamillez Olmo Classen^{1,2}, Jitka Becanova¹, Simon Votja¹, and Rainer Lohmann¹

¹Graduate School of Oceanography, University of Rhode Island, Narragansett, RI

²Department of Physics and Chemistry, University of Puerto Rico at Arecibo, Recinto de Arecibo, PR

Abstract

The lack of awareness and abuse of certain chemicals in our daily life, in the past years, has put our health at risk. Among these chemicals are flame retardants (FRs); these are chemicals which are added to flammable materials (for example, fabrics) to avoid or delay a fire. A specific group of FRs, organophosphate esters (OPEs), has been found in different and disturbing concentrations in different places of our ecosystem. This study focused on studying the marine waters of Narragansett Bay, primarily targeting twelve OPEs. Two passive samplers, polyethylene sheets (PEs) and graphene based passive samplers, were compared and characterized using a series of laboratory experiments. PEs were subsequently deployed at different depths and locations of the bay and then analyzed for concentrations of OPEs. After extraction, sample analysis was performed by Gas Chromatography coupled with Mass Spectrometry (GC/MS). The data show that these two passive samplers can gradually absorb OPEs. In laboratory experiments, we found graphene based samplers able to concentrate seven of the twelve compounds of study, whereas PEs concentrated nine of the compounds. For the bay deployments, PEs were less compatible for the OPEs than expected. More analysis should be performed in order to deeply compare these two passive samplers in the laboratory as well as in the field

(The rest of this section is intentionally left blank)

Understanding Sediment Biogeochemical Exchanges of Nutrients Impact on Ecosystem Health in Narragansett Bay

Forrest G. Pilone^{1,2} and Rebecca Robinson²

¹Department of Civil and Environmental Engineering, Colorado School of Mines, Golden, CO

²Graduate School of Oceanography, University of Rhode Island, Narragansett, RI

Running head: Springtime benthic nutrient fluxes in Narragansett Bay

Key Points:

- Nutrient and oxygen exchanges across the benthic layer are spatially variable within Narragansett Bay.
- The magnitudes of nutrient and oxygen fluxes tend to vary with anthropogenic impact.

Key Index Words: Nutrient, Exchange, Narragansett, Ecosystem, Health

Abstract

Nutrient exchanges driven through sediment and microbial processes and groundwater at the benthic layer represent important sources/sinks for nutrients involved in regulating key ecological phenomena in Narragansett Bay, such as seasonal hypoxic conditions. Utilizing the C-AIM benthic chamber lander, we isolated a known volume of the sediment-water interface for ~24 hours in 4 locations across Narragansett Bay, the Providence River (PR), Mount Hope Bay (MHB), Greenwich Bay (GB), and Mid Narragansett Bay (MidNB). Within the chamber, sensors measured pH, oxygen, and nitrous oxide *in situ*, in addition to a time-series collection of water samples for the analysis of ammonium (NH_4^+), nitrate (NO_3^-), and phosphate (PO_4^{3-}). MHB had the highest respiration rate, indicated by its oxygen drawdown, followed by PR, GB, and then MidNB. The greatest nitrogen flux was at MHB followed by PR, GB, and MidNB. PO_4^{3-} cycled in accordance with nitrogen in similar N:P ratios at all sites except MHB. Nutrient cycling at MidNB was small relative to other sites. This reflects the relative anthropogenic impact of nutrient loading on the PR, MHB, and GB sites when compared to less impacted MidNB site. These data will extend our understanding of the spatial and seasonal variability of benthic nutrient exchanges, improve constraints on nutrient budgets and ultimately, contribute to biogeochemical and ecological models of Narragansett Bay.

(The rest of this section is left blank)

THE EFFECT OF RISING AND FALLING TIDES AND CURRENT ON MATUNUCK OYSTER FARM

Sandra Rech^{1,2} and Chris Roman¹

¹Department of Electrical Engineering and Computer Science, University of Kansas, Lawrence, KS

²Graduate School of Oceanography, University of Rhode Island, Narragansett, RI

Abstract

Matunuck Oyster Farm, located in South Kingstown's Potter Pond, is an active aquaculture site where oysters are grown and harvested for Matunuck Oyster Bar. Many environmental factors such as tidal flux, current speed and bearing, water depth, and temperature affect the productivity of the oyster farm. By collecting and analyzing data on these environmental factors, the conditions of different areas within the farm can be observed and examined to possibly enhance productivity and wellness. The instruments used to collect data were the Lowell Tilt Current Meters (TCMs), Onset Water Level Loggers, and Onset HOBO Pendants. The TCMs recorded current direction and temperature, the water level logger recorded water depth, as a pressure measurement, and temperature, and the HOBO Pendants recorded temperature and light intensity. The data collected from these instruments at Potter Pond occurred between October 2018 and July 2019. The spatial variability across the farm was assessed by placing TCMs and Pendants around it. By attaching a small surface buoy to a long TCM, correlation between wind and current was investigated by observing how wind affected the current bearing and speed measured by a nearby short TCM. The analysis of this data exhibited that tide falls faster and that falling tide current moves to the east. The data also suggested that wind was only one of many natural phenomena that drive current due to their lack of correlation. Data will continue to be collected and analyzed to evaluate the spatial variability and enhance wellness across Matunuck Oyster Farm.

(The rest of this section is intentionally left blank)

Understanding the Key Contributors to Smooth Dogfish Trends in Abundance in New Jersey and Delaware Waters

Brianna Villalon^{1,2} and Camilla McCandless³

¹Graduate School of Oceanography, University of Rhode Island, Narragansett, RI

²Department of Biology, Texas A&M University, Corpus Christi, TX

³NOAA Fisheries, New England/Mid-Atlantic, Narragansett Laboratory, Narragansett RI

Abstract

The smooth dogfish, *Mustelus canis*, is a small coastal shark landed in a number of U.S. commercial fisheries. This study focused on the cause for the decrease in smooth dogfish catches during the NOAA shark survey in Delaware Bay. Another species, the sandbar shark, *Carcharhinus plumbeus*, showed an increasing trend during the same timeframe. To investigate these trends, we used NOAA survey data, along with trawl survey data from Delaware and New Jersey Divisions of Fish and Wildlife. Analyses indicated smooth dogfish catches are negatively correlated with temperature and larger sandbar catches within the bay. The sandbar is a more robust shark and may be outcompeting the smooth dogfish for the baited hooks. There is some habitat partitioning between the two species since small sandbar sharks use the shallow waters of the bay, whereas smooth dogfish tend to use the deeper cooler waters. The larger juvenile sandbars are widespread throughout the bay and would more likely interact with smooth dogfish. Regression analysis shows a significant positive trend in bottom water temperature across years during June. Smooth dogfish are a cooler water species that migrate into and out of the bay earlier than sandbar sharks. In response to increases in sandbars and water temperatures, smooth dogfish may be migrating out of the bay sooner. Adult smooth dogfish use the bay for mating and pupping in the spring. Juvenile smooth dogfish also return in the spring, but without the need to mate or pup they may migrate out sooner as temperatures rise.

(The rest of this section is intentionally left blank)

Using Multi-GNSS Interferometric Reflectometry to Monitor Sea Level in Newport, Rhode Island

Benjamin A. Watzak^{1,2} and Meng Wei¹

¹University of Rhode Island, Graduate School of Oceanography

²Texas A&M University – College Station

Corresponding author: Benjamin Watzak (bawatzak@tamu.edu)

Key Words: Reflectometry, GNSS, Signal-to-Noise Ratio, Tidal Gauge

Abstract

Monitoring sea level accurately at low cost is critical to managing the challenges of sea level rise and climate change. Here, multi- Global Navigation Satellite System (multi-GNSS) interferometric reflectometry is used to monitor sea level in Narragansett Bay, Newport, Rhode Island. This technique uses the time delay between direct and reflected signals to measure reflector height (H_R), which is the distance between the receiver and the water surface. Compared to traditional tidal gauges, the reflectometry method has a lower associated cost and can be implemented along any coastline, without having to account for vertical land motion. Beginning with an analysis of GPS (United States GNSS) data, using existing software tools and estimated satellite ephemerides, we calculated crude daily mean H_R over a period of 8 months between 2018 and 2019. These daily mean water levels were compared to co-located data from the NOAA tidal gauge in Newport, RI. The method and software tools underwent a refinement to reduce the error and offset of the resulting water levels. Most notably, this included processing the RINEX data with precise satellite ephemerides, as well as adding a function to calculate a weighted average H_R based on a bimodal Gaussian Mixed Model of the Signal-to-Noise Ratio peak values. GLONASS (Russian GNSS) data were then incorporated, allowing for more observations per epoch because of a larger available dataset. This further reduced the error in the daily water levels; by about 19% for May and June 2019. These new H_R measurements resulted in a highly correlated representation of the long-term water level trends observed in the tidal gauge data. Annotated code has been published to apply this work at other multi-GNSS receiver sites. Coupling this improved method with already-existing tidal gauges will enable more accurate and more abundant measurements of sea level, in space and time, around the world.

1. Introduction

Interferometric Reflectometry (IR) has been developing as a new and important method of measuring sea level (Larson et. al., 2010). It has also been shown to be useful in monitoring soil moisture (Larson et. al., 2010). The resulting water levels usually compare favorably with tidal gauge data from a nearby station.

The method of GNSS-IR for measuring water levels makes use of the multiple pathways a GNSS signal can take (multipath) (Figure 1). More specifically, we focus on an analysis of the Signal-to-Noise Ratio (SNR) of the reflected signal. We use a single geodetic-quality GNSS receiver to obtain these measurements. This is the method that has been developed and tested by Larson et. al. (2013b), among others.

This project is designed to test the method of GPS IR at the Coasters Harbor Island, Newport, Rhode Island (NPRI) site. We also look into the gains made, if any, by using multiple GNSS (GPS + GLONASS) to obtain water levels.

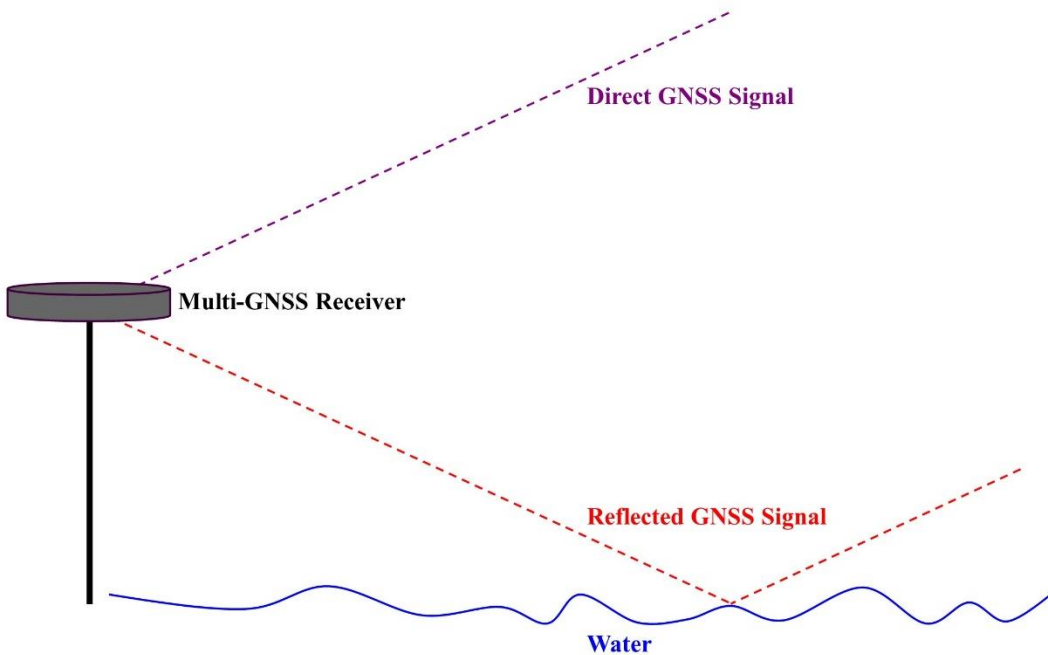


Figure 1: Visual schematic of GNSS-IR method. A GNSS signal can travel directly from satellite to receiver. It can also be reflected off of water and then travel to the receiver. This phenomenon is known as multipath.

To find the tools used in this study, you can visit https://github.com/bawatzak/gnss_NPRI. It should be noted that the files contained in this folder are only those that were created for this study and/or modified from the code made available by Roesler & Larson (2018).

2. Data



Figure 2: Trimble NetR9 multi-GNSS receiver at NPRI site with view of Narragansett Bay (41.5041, -71.3256).

NOAA owns and operates the GNSS tracker in NPRI. It uses a Trimble NetR9 geodetic-quality single multi-GNSS receiver and produces daily files that are in binary format. In order to use these data, each daily file was translated using the TEQC conversion tool from UNAVCO into satellite observation files (Table 1).

Table 1: GNSS data collected at the NPRI site and gathered into observation files.

GNSS Constellation	Signal	Options	Pseudorange	Signal Strength	Dates Used
GPS	L1 - C/A		C1, P1	S1	11/10/18 – 04/11/19, 05/14/19 – 07/05/19
GPS	L2E	C and E	C2, P2	S2	11/10/18 – 04/11/19, 05/14/19 – 07/05/19
GPS	L2C	CM + CL	C2, P2	S2	11/10/18 – 04/11/19, 05/14/19 – 07/05/19
GPS	L5	I + Q	C5	S5	11/10/18 – 04/11/19, 05/14/19 – 07/05/19
GLONASS	L1 - C/A		C1, P1	S1	04/06/19 – 04/11/19, 05/14/19 – 07/05/19
GLONASS	L1P		C1, P1	S1	04/06/19 – 04/11/19, 05/14/19 – 07/05/19
GLONASS	L2 - C/A	(M) only	C2, P2	S2	04/06/19 – 04/11/19, 05/14/19 – 07/05/19
GLONASS	L7	Data + Pilot	C7	S7	04/06/19 – 04/11/19, 05/14/19 – 07/05/19

Daily observation files from November 10, 2018 up to July 5, 2019 were analyzed. It must be noted that from April 11, 2019 to May 14, 2019 the receiver had wiring and electrical issues, so data is missing for these dates. The SNR data that were used for an analysis of water levels comes from the S1, S2, and S5 observations throughout the day. S7 data were not analyzed in this study because the Fortran tools currently do not allow for this.

Data from the co-located tidal gauge were obtained from the NPRI station home page (accessible through NOAA Tides and Currents). We chose to use the verified hourly observations, in meters, with Mean Sea Level (MSL) as the reference point. Thus, we used 24 tidal gauge observations per day, for every day since installation of the GNSS receiver. We later made use of sp3 files, which contain precise, documented satellite ephemerides for a whole day. Such files were downloaded from NASA gnss products in GFZ format so as to include GPS and GLONASS.

3. Methodology

3.1 Applying data constraints

Because the location has several obstructions to open water, signal data must be restricted to only those that are reflected from the water surface. Therefore, quality control criteria are applied to the observation data. An elevation and azimuthal angle mask are applied to the data so as to only collect SNR from reflected signals (those between 3.5° and 16° elevation, and 15° to 145.1° azimuths). These constraints have come from an analysis of several Fresnel zone overlays, such as the one in Figure 3, which were created using the software developed by Roesler & Larson (2018).

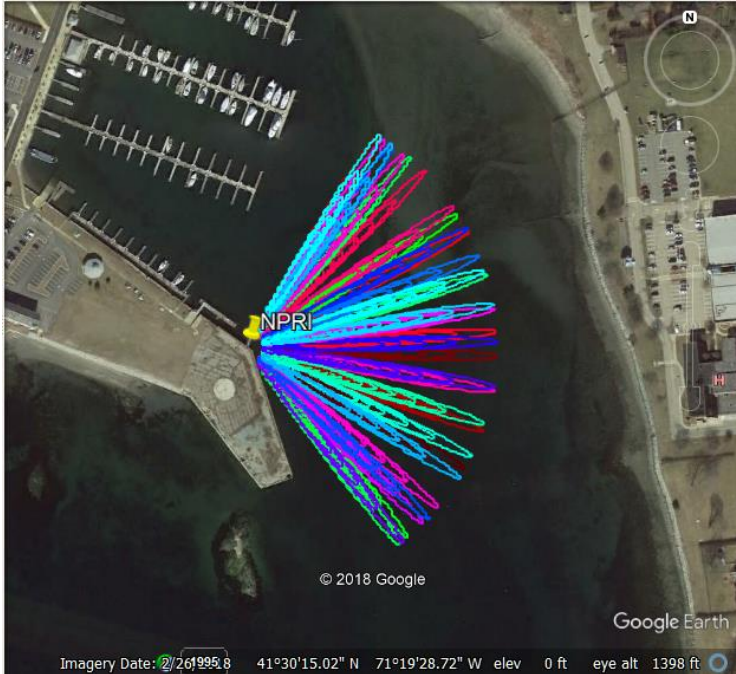


Figure 3: Aerial view of NPRI site via Google Earth, with a Fresnel zone overlay. All possible azimuths between 15° to 145.1° are considered, while elevation angles are considered every 0.5°, ranging from 3.5° to 16°.

3.2 Forming an average

We began by using calculated satellite ephemerides from a RINEX navigation file. SNR data from reflected GNSS signals were analyzed in MATLAB using tools developed and made available by Roesler & Larson (2018). We began with observing the SNR tracks and the daily Lomb-Scargle Periodograms (LSPs) that the MATLAB tool produces for the NPRI site. The original tool outputs the daily median Reflector Height (H_R), which is a measure of the distance between the receiver and the water surface. The median was used because it is a value unaffected by outliers and extraneous data. Once we were sure of the viability of this site, based on relative homogeneity of the LSP tracks for each signal type (L1, L2, and L5), we began to look for a way to calculate a daily average.

Before we could calculate a daily average, we needed a way to evaluate our anticipated results. An acoustic Aquatrak tidal gauge owned and operated by NOAA is situated within a few yards of the GNSS receiver. Therefore, it is the perfect standard by which to assess the IR method at NPRI. In theory, the two methods should yield the same water level trends. Because the water levels from each method are taken with respect to different reference points, we adjust the tidal gauge measurements (TG). This adjustment puts both water levels into the same reference frame. Due to the counter-intuitive direction of H_R values, where larger values mean lower water levels, we have changed the sign of the tidal gauge measurements. Then, we add the distance of the GNSS phase center above MSL (5.0952 m). The following equation gives our final tidal gauge data set, Tidal Gauge Adjusted (TGA).

$$TGA = -1 * TG + 5.0952$$

It should be noted that we could have, instead, adjusted the H_R measurements so as to be relative to MSL.

Because GPS signals have been recorded for the entire timespan of our dataset, we began our quest for a daily mean by only analyzing GPS SNR values. For each of the three signal types, MATLAB compiles all SNR tracks that meet the quality control criteria listed in section 3.1. We began with a comparison of the crude (unweighted) average of the H_R values at LSP peaks taken over the course of a day for each frequency, against the crude mean of 24 hourly TGA measurements. Once this was done, it was evident that a new method of finding daily means was needed.

So, a new method was developed; one which clusters the H_R values of the LSP peaks into two groups, according to a double-peaked Gaussian Mixed Model (GMM) (Figure 4). Such a model searches for two normally-distributed subpopulations of the data. Using the fitgmdist function in MATLAB, we can obtain some sample statistics from these subpopulations: means ($\hat{\mu}_1$ and $\hat{\mu}_2$), variances ($\hat{\sigma}_1^2$ and $\hat{\sigma}_2^2$), and relative proportions of the population (\hat{p}_1 and \hat{p}_2). The daily average for each frequency, f , is taken as a weighted average of the two mean H_R values from the GMM. The variance of each frequency's average is also taken, which represents a weighted variance of the two GMM peaks' variances. They are calculated as follows:

$$\bar{H}_{R,f} = \hat{p}_{1,f} * \hat{\mu}_{1,f} + \hat{p}_{2,f} * \hat{\mu}_{2,f}$$

$$\hat{\sigma}_f^2 = \hat{p}_{1,f}^2 * \hat{\sigma}_{1,f}^2 + \hat{p}_{2,f}^2 * \hat{\sigma}_{2,f}^2$$

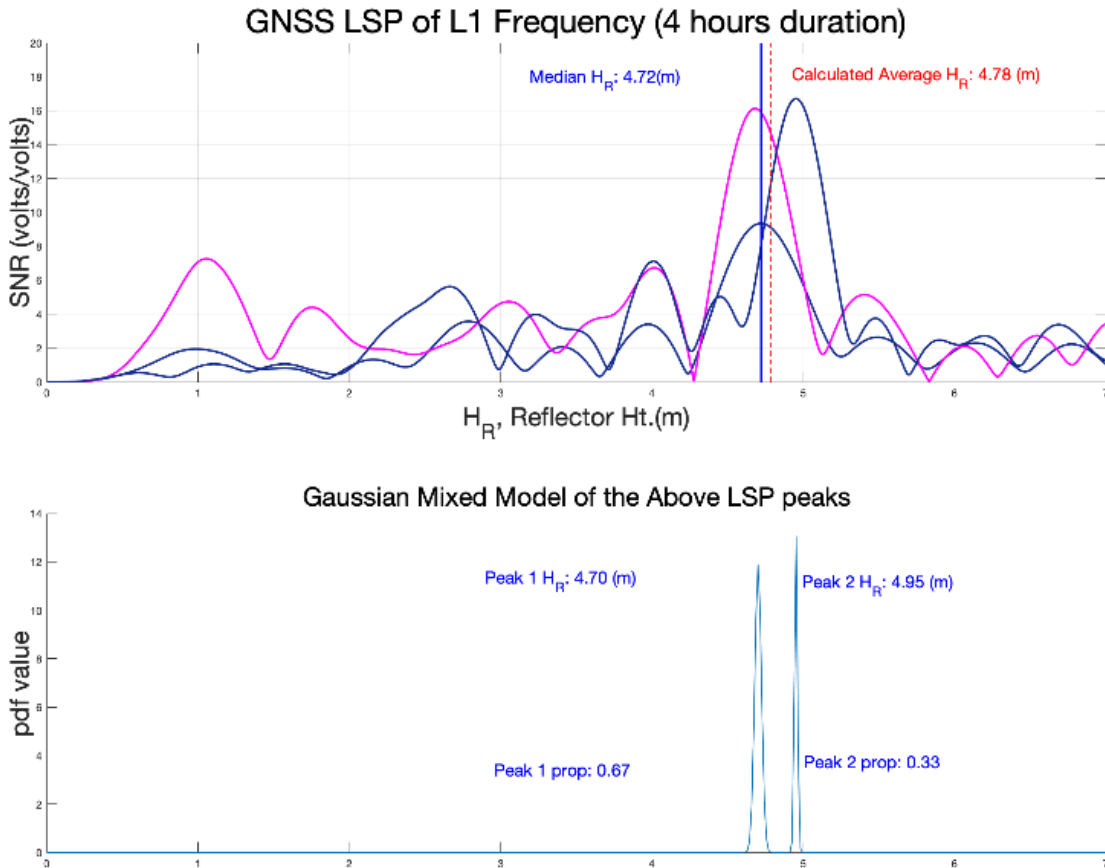


Figure 4: (top) LSP for L1 SNR tracks observed over a 4-hour period. The pink track is from GPS, whereas the blue tracks are from GLONASS. (bottom) GMM relative pdf plot of the H_R values observed at the peak values of the corresponding LSP.

This GMM approach was originally adopted as a means to identify and remedy the issue of L2 double-peaks due to the cross-correlation. However, it was later implemented in all frequencies because it allows the method to capture high and low tide subpopulations over each day. Subsequently, to get a daily average H_R , we take a weighted average of the three daily averages given by each frequency. Each of the three daily averages is given a weight w_f that is inversely related to its standard error. For example, the frequency with the average that has the smallest

standard error is given the largest weight. The combined daily average $\bar{H}_{R,Combined}$ is taken as follows, with a subsequent sample variance $\hat{\sigma}_{Combined}^2$:

$$w_f = 1 - \frac{\hat{\sigma}_f}{\sum \hat{\sigma}_i}$$

$$\bar{H}_{R,Combined} = \frac{\sum \{w_f * \bar{H}_{R,f}\}}{\sum w_f}$$

$$\hat{\sigma}_{Combined}^2 = \frac{\sum \{w_f^2 * \hat{\sigma}_f^2\}}{\{\sum w_f\}^2}$$

Once this method was developed, the resulting daily averages were again compared to those of a tidal gauge. We then proceeded to implementing multiple GNSS constellations. In order to do so, we switched to a new translation tool, also developed by Roesler & Larson (2018), that is able to convert observation files into SNR data for all GNSS constellations. This new tool also requires the use of precise satellite ephemerides. Because precise ephemerides from sp3 files replaced those of a RINEX nav file, we used this new tool to create new SNR files for the whole dataset at NPRI (including those that were not multi-GNSS). Using the same improved method of obtaining $\bar{H}_{R,Combined}$, we then incorporated all GPS and GLONASS satellite tracks available for the whole timespan of the dataset.

3.3 Evaluating the model

There are three measures by which we assess the validity of the model. The first is the correlation coefficient between the TGA and the H_R values. The second is Root Mean Squared Difference (RMSD), which is a measure of how well the H_R values match the TGA values, i.e. RMSD quantifies the offset between the two methods. The third is the Root Mean Squared Error (RMSE), a measure of the uncertainty (variance) in the mean H_R values. RMSD and RMSE are calculated as follows, with number of observations N_{obs} , which in this case is the number of daily $\bar{H}_{R,Combined}$ measurements.

$$\text{RMSD} = \sqrt{\sum \{(TGA - H_R)^2\} / N_{obs}}$$

$$\text{RMSE} = \sqrt{\sum \hat{\sigma}_{Combined}^2 / N_{obs}}$$

4. Results

Beginning with a sub-daily scale (Figure 5), we can already begin to notice a strong correlation between the water levels obtained by IR and those of TGA measurements. It is evident that data from the IR method captures high and low tides well. The high correlation between the methods increases as we average over larger periods of time.

A complete comparison of TGA daily means and combined H_R daily means is compiled for the period of November 10, 2018 to July 5, 2019 (Figure 6). The two daily water level measurements have a correlation coefficient of 0.9153, indicating that the two methods produce highly positively correlated water levels. This entire dataset of daily values also has a RMSD of 0.1312 m. When looking at only the daily averages from the dates before GLONASS was incorporated, we find a RMSD of only 0.1190 m.

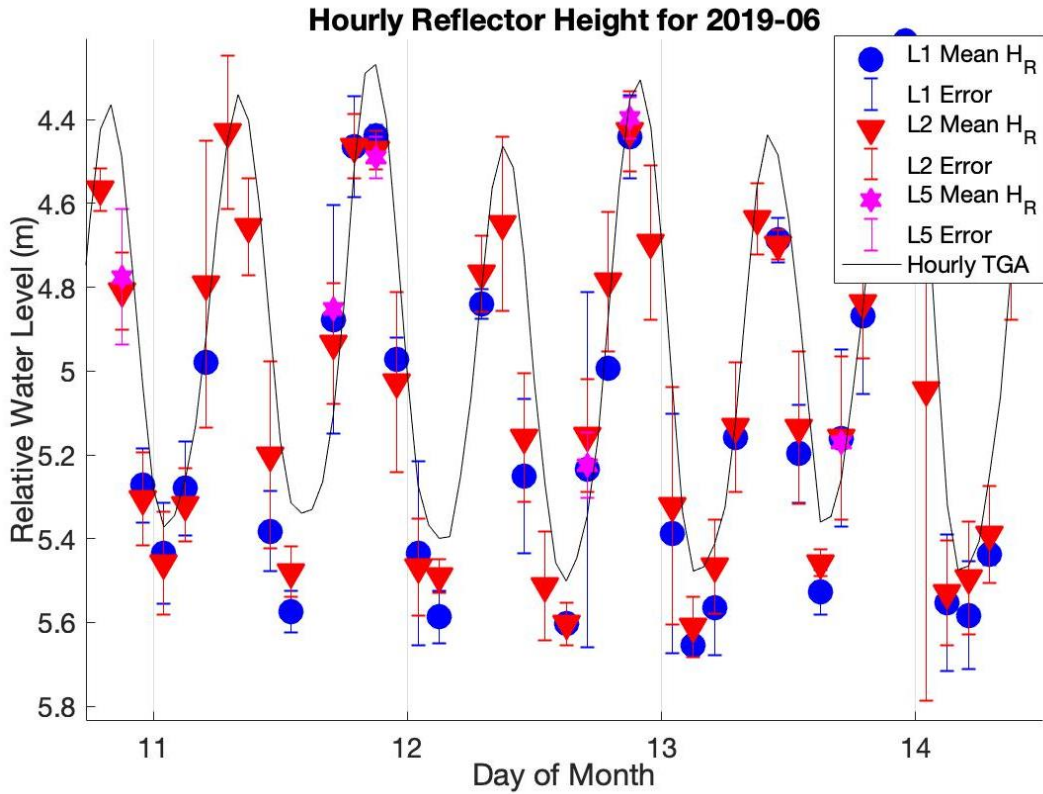


Figure 5: Water level measurements on a sub-daily scale. TGA measurements are taken each hour. H_R measurements represent a crude (unweighted) mean of the H_R values (taken from LSP peaks for each GNSS frequency) over a two-hour period. The error bars extend to ± 1 standard deviation of the respective mean.

We then determine the effects of adding GLONASS to our dataset by looking at RMSD and RMSE of daily measurements in May and June. The statistics suggest that adding GLONASS to the dataset negatively affects the resulting H_R measurements (Table 3). This is because the RMSD of both months is higher when using GPS+GLONASS data than when using GPS-only data. This leads to the implication that the resulting water levels of the multi-GNSS method are farther from TGA levels than the GPS-only water levels. Similar trends are observed in sub-daily measurements as well. On the other hand, it is worth noting that RMSE of the mean H_R is reduced by the addition of GLONASS. This leads to the implication that the GPS+GLONASS dataset reduces the uncertainty of the mean H_R .

Then we look at a larger scale: months. We average the daily water level averages over the course of each month (using only the dates where GNSS data is available). We find that the resulting monthly average water levels, of H_R and TGA, have a correlation coefficient of 0.9657, with a RMSD of 0.1197 m.

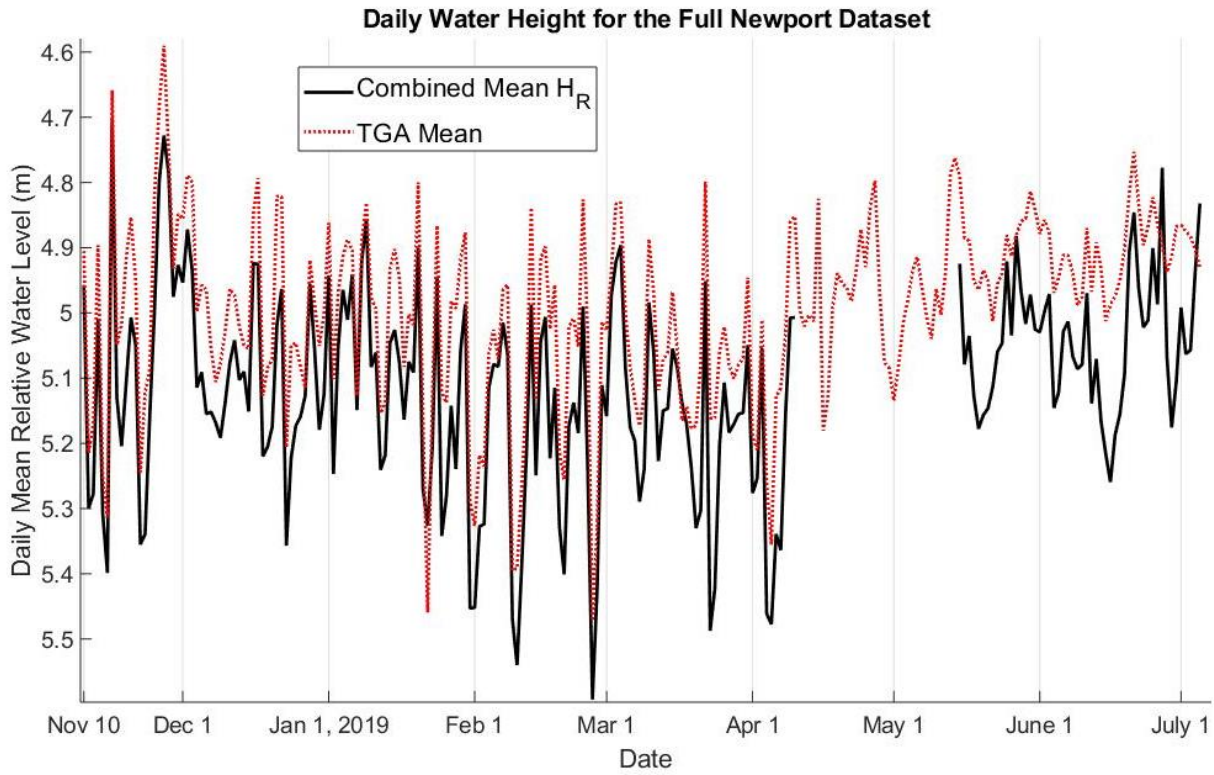


Figure 6: Plot of daily mean values for both IR and TGA, beginning Nov. 10, 2018 and ending July 5, 2019. The high correlation between the methods is visually evident.

Table 2: Validity checking of the IR method for May and June 2019, using daily averages for comparison.

Month	Time Frame of Measurements	Type	Correlation Coefficient	RMSD	RMSE
May	daily	GPS+GLONASS	0.7343	0.1510	0.0910
May	daily	GPS-only	0.8066	0.1100	0.1130
June	daily	GPS+GLONASS	0.7849	0.1619	0.1030
June	daily	GPS-only	0.7632	0.1249	0.1266

5. Discussion

5.1 The efficacy of GNSS-IR as a tidal gauge

The method of GNSS-IR produces H_R values that are highly correlated with TGA values at the NPRI site. In short, it means the method works for measuring water levels, especially over periods of time longer than a day. Our RMSD results, surprisingly, do not compare favorably to those of Larson et. al. (2017) for daily means, nor do they compare favorably on a monthly scale. Some of the offset may be attributed to error in the acoustic Aquatrak method (Larson et. al, 2017), which is where the TGA measurements come from. This is in part the reason that NOAA has installed a

MW WL sensor at the NPRI site and is ultimately looking to use that as the primary source of tidal gauge measurements (Heitsenrether-Park, 2014).

However, it should be noted that the multi-GNSS receiver itself does have some setbacks. The gap in the IR dataset for April and May was due to an electrical wiring error. It was also expected that we would have data for all of July by the end of the project. However, there was an issue again that occurred on July 5, not allowing for any subsequent data. This went unnoticed until August, when we went to collect our July data. Therefore, this method of taking water levels requires a little more monitoring and maintenance than previously thought necessary.

5.2 The efficacy of adding GLONASS

As noted previously, using the combined dataset reduces the uncertainty of the daily averages, but actually increases the RMSD. This is likely due to GLONASS having a much larger measurement noise than that of GPS (Cai et. al., 2016). This phenomenon requires further investigation because the differences in RMSD were relatively small, and we only have 1.5 months of multi-GNSS data. Additionally, because the RMSD values do not compare favorably with previous studies, even using GPS-only, it is certain that the addition of GLONASS is not the only issue at the NPRI site.

5.3 Future work

While the method that is currently used to take a daily average works relatively well, it is not the best. There is much room for improvement. Perhaps when taking an average over the course of a day, a GMM with three subpopulations should be considered: one for high tides, one for low, and one for in-between. More likely is that a GMM is not the best way to take a daily average H_R for each frequency. It is worth looking into taking a daily mean H_R as an average of 4 to 6 sub-daily H_R measurements so as to be more consistent with the method of obtaining a daily average TGA value, while also allowing for a sufficient number of observations per time slot.

Given that the resulting H_R measurements are pretty consistently lower than the TGA values, this is an issue that will need to be explored further. It is possible that a measurement of distance between reference points at the NPRI site was taken incorrectly, or has changed since the original measurement. This would also explain our large RMSD values. Due to the location of the GNSS receiver at the Naval War College, it was not possible to visit the site and verify measurements.

The results suggest that adding more GNSS constellations reduces uncertainty of the averages. It is possible that adding other GNSS with smaller measurement noises may also reduce RMSD of the method. The Fortran tools will also need some modification to allow for analysis of other frequencies such as GLONASS L7.

Additionally, in the future it would be advantageous to move the GNSS receiver to a nearby, yet different spot. It was placed on the same structure as the MW WL sensor that is to be implemented soon, so as to allow for truly co-located data. However, as is visible in Figure 3, the range of water for signal reflection is limited. This severely limits the amount of reflected SNR data we are able to take. Lastly, more data would have provided more telling results. With less than a year of GPS data, and fewer than 60 days of multi-GNSS data, the conclusions we can make about the NPRI site are limited.

6. Conclusions

Multi-GNSS IR was proven to be an effective method of sea level tracking at the NPRI site, given that its results were highly correlated with those of the co-located tidal gauge. The employed method of taking an average reduces the uncertainty of the measurements, especially over longer time scales. The uncertainty is further reduced by the incorporation of GLONASS data, though this comes with an increase in the offset of the measurements, which requires further investigation. This method can be implemented, at low cost, anywhere along the coast where there is a wide range of unobstructed water, allowing for a spatially and temporally denser dataset of sea level tracking.

Acknowledgements

The authors would like to acknowledge the support of the following persons, who provided content expertise and advice: Kristine Larson (University of Colorado Boulder), Eric Breuer and Robert Heitsenrether (NOAA), and Simon Williams (UK National Oceanography Centre). We would also like to thank the URI SURFO program, funded by the NSF, for providing the opportunity and funds for this project.

References

- Atilaw, T. Y., P. Cilliers, and P. Martinez (2017), Azimuth-dependent elevation threshold (ADET) masks to reduce multipath errors in ionospheric studies using GNSS, *Advances in Space Research*, 59(11), 2726–2739, doi:10.1016/j.asr.2016.10.021.
- Bilich, Andria, Axelrad, Penina, Larson, Kristine M., "Scientific Utility of the Signal-to-Noise Ratio (SNR) Reported by Geodetic GPS Receivers," Proceedings of the 20th International Technical Meeting of the Satellite Division of The Institute of Navigation (ION GNSS 2007), Fort Worth, TX, September 2007, pp. 1999-2010.
- Cai, C., C. He, R. Santerre, L. Pan, X. Cui, and J. Zhu (2016), A comparative analysis of measurement noise and multipath for four constellations: GPS, BeiDou, GLONASS and Galileo, *Survey Review*, 48(349), 287–295, doi:10.1179/1752270615y.0000000032.
- Heitsenrether, R., and J. Park (2014), *NOAA's Recent Test, Evaluation, and Operational Use of Microwave Radar Water Level Sensors*.
- Larson, K. M., R. D. Ray, F. G. Nievinski, and J. T. Freymueller (2013a), The Accidental Tide Gauge: A GPS Reflection Case Study From Kachemak Bay, Alaska, *IEEE Geoscience and Remote Sensing Letters*, 10(5), 1200–1204, doi:10.1109/lgrs.2012.2236075.
- Larson, K. M., J. J. Braun, E. E. Small, V. U. Zavorotny, E. D. Gutmann, and A. L. Bilich (2010), GPS Multipath and Its Relation to Near-Surface Soil Moisture Content, *IEEE Journal of Selected Topics in Applied Earth Observations and Remote Sensing*, 3(1), 91–99, doi:10.1109/jstars.2009.2033612.
- Larson, K. M., J. S. Löfgren, and R. Haas (2013b), Coastal sea level measurements using a single geodetic GPS receiver, *Advances in Space Research*, 51(8), 1301–1310, doi:10.1016/j.asr.2012.04.017.
- Larson, K. M., R. D. Ray, and S. D. P. Williams (2017), A 10-Year Comparison of Water Levels Measured with a Geodetic GPS Receiver versus a Conventional Tide Gauge, *Journal of Atmospheric and Oceanic Technology*, 34(2), 295–307, doi:10.1175/jtech-d-16-0101.1.
- Roesler, C., and K. M. Larson (2018), Software tools for GNSS interferometric reflectometry (GNSS-IR), *GPS Solutions*, 22(3), doi:10.1007/s10291-018-0744-8.
- Vanderplas, J. T. (2018), Understanding the Lomb–Scargle Periodogram, *The Astrophysical Journal Supplement Series*, 236(1), 16, doi:10.3847/1538-4365/aab766.